Numerical Techniques for the Simulation of PDEs on Surfaces for Biomathematical Problems

---

Dissertation
zur Erlangung des akademischen Grades eines
Doktors der Naturwissenschaften (Dr. rer. nat.)

Der Fakultät für Mathematik der
Technischen Universität Dortmund
vorgelegt von

Ramzan Ali

im März 2016

Gedruckt bzw. veröffentlicht mit Unterstützung des Deutschen Akademischen Austauschdienstes

Dissertation

Numerical Techniques for the Simulation of PDEs on Surfaces for Biomathematical Problems

Fakultät für Mathematik

Technische Universität Dortmund

Erstgutachter: Prof. Dr. Stefan Turek

Zweitgutachter: Prof. Dr. Dmitri Kuzmin

Tag der mündlichen Prüfung: 20.06.2016

Numerical Techniques for the Simulation of PDEs on Surfaces for Biomathematical Problems

Abstract. The aim of this thesis is to design new algorithmic tools with which the biomathematical models on stationary and evolving-in-time surfaces can be studied and to perform related numerical analysis.

Surface PDEs models can describe several engineering applications, e.g., in fluid mechanics, modeling of membranes and image processing. The equations which describe biological phenomena are strongly coupled nonlinear systems of PDEs. The modeling of more realistic biological applications can generate complex systems of equations defined on surfaces. The domain in which the PDEs are defined can often be a challenging morphology and analytical solution for such complicated dynamical systems are not available. Nevertheless numerical solutions for such biomathemtical problems are possible and require fast, highly accurate and efficient solvers.

The present work analyzes the numerical treatment of PDEs on surfaces and provides a flexible numerical framework to solve PDEs on a stationary quadrilateral mesh.

The developed numerical approach combines the level set methodology for the implicit description of stationary and evolving surfaces with the Eulerian finite element formulation. The theory of level set methods utilizes the Eulerian formulation for partial differential equations, instead of looking at boundary motion from a natural geometric Lagrangian perspective. In order to formulate the mathematical equations, we present the necessary foundation in the context of evolving surfaces. The most significant advantages of the proposed scheme are the curvature-free calculation, i.e., the mean curvature is no more explicitly calculated. Moreover, it allows the coupling of PDEs defined on surfaces with those defined in a bulk region.

An adequate numerical scheme has to be free of numerical instabilities. The problem in hand is convection dominated which occurs due to the chemotaxis model, the transport of the cell density and surface evolution. The solution can produce non-physical spurious oscillations and can diverge from the realistic solution profiles. It is known that the pure Galerkin formulation is not sufficient to solve PDEs on surfaces with biomathematical applications. The positivity preserving scheme is obtained by using flux-corrected transport schemes of TVD and FCT-types, so that the constructed scheme is stable and positivity preserving.

The developed numerical scheme is validated by solving several problems of biomathematical models on surfaces. The discussed test cases are taken from mathematical biology of pattern formation, e.g., the numerical solution of the Schnakenberg model on a non-trivial stationary surface in three dimensional Euclidean space and the transport of cell density on a sphere. Furthermore, we demonstrated the coupling of the Koch-Meinhardt reaction-diffusion model of the Turing-type with the evolution of level sets, where the normal velocity of a surface resp., level set is proportional to the numerical solution of the

model.

The numerical results support the reliability of the proposed computational framework in terms of numerical convergence and capturing of expected solution profiles. The computational and analytical complexity significantly increase for realistic applications. Thus, the developed approach can readily be employed for biological applications that involve PDEs on evolving surfaces. This numerical scheme is also applicable to three dimensional models which is mandatory when considering real-life applications.

Keywords: Evolving Surfaces; Level Set; Finite Element Method; FCT/TVD; Chemotaxis; Patterns Formation.

Dortmund, March 10, 2016

Ramzan Ali

To
My Parents
&
Zahida Bano

Acknowledgments

First of all, I am grateful to my supervisor Prof. Dr. Stefan Turek for his constant support, encouragement and constructive criticism on this work. His progressive attitude towards research enabled me to develop an understanding of the topic with further advancement. He offered indispensable support and guidance throughout my PhD research.

Secondly, I am sincerely thankful to my research mentor Dr. Andriy Sokolov for his thoughtful motivation throughout this project. He introduced me to a wide research area of surface PDEs with potential application in mathematical biology. Thanks for always being there for discussion on numerical state-of-the-art and algorithmic implementation. I am indebted for your passion and continuous consultation during the entire time of this research work.

I would like to thank Dr. Robert Strehl for his exchange of ideas concerning literature on mathematical biology in the early stage of the research and mutual coordination in numerical implementation. Special thanks to PD. Dr. Frank Klinker for his thoughtful conversation on differential geometry and mathematical formulation of the surface defined PDEs.

I would like to express my gratitude for members of the institute of applied mathematics and numerics TU-Dortmund for their invaluable support during these last years. Thanks to Dr. Abderrahim Ouazzi, Dr. Mudassar Razzaq, Dr. Amin Safi, Absaar Ul Jabbar, Babak Sayyid Hosseini and Muhammad Waseem for sharing scientific and non-scientific thoughts during this period.

This work is supported by University of Central Asia Faculty Development Program in collaboration with DAAD. I greatly appreciate both parties for their funding.

Finally, I thank my family, particularly my parents and my beloved wife Zahida Bano for enthusiasm and well wishes to continue my studies.

Dortmund, February 25, 2016

Ramzan Ali

Contents

1 Introduction

This chapter provides a brief account on the motivation of the research work introducing few generalizations about the partial differential equations on surfaces. In addition, their applications in biological science including pros and cons of different techniques to solve partial differential equations on evolving surfaces. A brief summary of the mathematical development of chemotaxis and pattern forming models is presented. The subsequent section is followed by a concise note on notations used as well as an outline of the research dissertation.

1.1 Motivation

Mathematics is the foundation of all science and possesses the quality to make links with other fields of science, like biology, physics, technology and each interaction with new research area introduces and develops new mathematical challenges to work. For instance, mathematical biology is one such example. It is an emerging subject, Murray [79, 80] recently published on this topic. The involvement of mathematics in bio-science is important, as the biology depends on qualitative and quantitative studies of mathematical objects. Mathematics exhibits a strong quality to transform a complex natural phenomena into mathematical equations, then uses a wide range of techniques to analyze different variables. Therefore the complexity of biological science makes the involvement of mathematics inevitable.
Recently, computer simulations have been intensively applied in life-science such as bio-engineering, bioinformatics and biomathematics. The applications of mathematical biology are rapidly growing yet remain an underexplored area and attracting a large number of researchers [73, 74, 78, 94, 98, 101, 117, 134] to study several biological models with advances in computing. The computational value of simulation is cost-effective and faster than laboratory based practical experiments, consequently, the interdisciplinary research will produce useful outcome.

The experimental work is an important component in determination of the biological mechanisms, moreover, the theoretical investigation established for the simulation of mathematical models has a key role in developmental biology, e.g., to name few contributions, cf. [38, 73, 78, 98, 117, 130–132]. It is always useful to interpolate and simulate a realistic data set through computational science. The mathematical modeling and simulation provide an essential tool, which can

be used to investigate and test the hypothesis, to predict and propose a testable solution. In addition, focusing on certain parameters of a biological system can demonstrate how some components lead to enigmatic phenomena. It is harder to perceive such intuitions in laboratory as compared to simulations. The characterization and modeling of simple biological phenomena often lead to a formidable set of mathematical equations. The analytical solution of such systems is often highly complicated to perform. Besides the complication of mathematical equations, the lack of theoretical results compels us to use numerical simulations for investigating such models. Consequently, an advanced numerical simulation to study the biological models will be developed.

1.2 Preliminaries

Here, we will provide a general overview on most commonly used symbols and notations throughout this work. In order to keep a section self-contained, for newly used terms we will define the corresponding symbols and notations in the context of each section.

1.2.1 General notation

Let us suppose that $\Omega \subset \mathbb{R}^d$, where the dimension $(d = 1,2,3,\ldots)$ the spatial computational domain Ω with boundary $\partial\Omega$. The spatial variable $\mathbf{x} = (x^1, x^2, x^3, \ldots) \in \Omega$. Consider $\Gamma(t)$ as an evolving in time surface, further assume that the evolving surface Γ does not exceed the underlying stationary domain, i.e., $\Gamma \subset \Omega$. The temporal variable is denoted by t, where $I = [0,T] \subset \mathbb{R}$ with $T > 0$ is a suitable time interval for the solution. Hence, the entire space-time domain is described through $(\mathbf{x},t) \in \Omega \times I$.

The divergence operator defined on a vector field $\boldsymbol{\xi}$ is given by

$$\nabla \cdot \boldsymbol{\xi} = \sum_{i=1}^{d} \frac{\partial \xi^i}{\partial x^i}.$$

For a function $\rho \in C^2(\Omega)$, we can define the gradient operator:

$$\nabla \rho = \left(\frac{\partial \rho}{\partial x^1}, \ldots, \frac{\partial \rho}{\partial x^d} \right)^T.$$

The usual Laplacian operator defined through

$$\Delta := \nabla \cdot \nabla$$

for a differentiable function ρ, as:

$$\Delta \rho = \sum_{i=1}^{d} \frac{\partial^2 \rho^i}{(\partial x^i)^2}.$$

The gradient and divergence on a surface including Laplace-Beltrami operator will explicitly defined in §2.2. The most frequently used notations are provided in tabular form $(Table : 1.1)$, other symbols will be described whenever they are required.

bold letters, $\boldsymbol{a}$, $\boldsymbol{b}$, $\boldsymbol{c}$ and $\boldsymbol{d}$	vector value functions
a, b and c	scalar values
d	spatial dimension, e.g., $d = 1,2,3\dots$
$\mathbf{x}$	spatial variable, i.e., $\mathbf{x} = (x^1, x^2, \dots) \in \mathbb{R}^d$
t	temporal variable
$I = [0,T]$	temporal interval
m	time level index e.g., $\rho^{m+1} = \rho(m + \Delta t)$
bold face $\boldsymbol{A}$, $\boldsymbol{B}$, $\boldsymbol{C}$, $\dots$	block matrices
Greek letters α, β, γ, $\dots$	scalar value functions
$\Gamma(t), \Gamma_h$	continuous evolving surface and the discrete counterpart
Δ_Γ	Laplace-Beltrami operator
Ω	spatial domain
Ω_h	discretized domain
h	fixed mesh size
$\mathbf{n}$	normal vector
V, V_h	continuous space of function and its discrete counterpart
φ_i	nodal basis function, $\varphi_i \in V_h$ for $i = 1,2,\dots,N$
N	d.o.f. number of degrees of freedom
$(\boldsymbol{\rho}, \boldsymbol{\zeta}, \boldsymbol{c})$	continuous coefficients vectors
(ρ_h, ζ_h, c_h)	finite element functions

Table 1.1: General notations

1.3 Surface PDEs and related techniques

A large class of natural phenomena occur on evolving in time surfaces (e.g., in biology; biological membrane, animal skin, general growth and etc.), besides the

usual Euclidean domain Ω. Thus the modeling of partial differential equations (PDEs) on the general manifolds is significant [38, 62, 116, 139]. In addition, PDEs on surfaces have a wide range of applications, to name few in flow problem; surfactant flow by Stone [116], flows over topography, atmospherics flow on the surface of the Earth and virtual weathering [24]. In computer science, we have image processing, medical imaging [22], computer vision, computer-aided design and computer graphics, which are mostly involved in creation and optimization of engineering problems. In biology which is the main purpose of this thesis, the study of PDEs on biological surfaces is a rapidly growing interdisciplinary field of research, which generated new fields like computational biology or biomedical-engineering. A myriad number of research problems in this field are highly challenging due to mathematical and biological constraints on surfaces, but the results have quite promising implications in developmental biology. Since computational fluid dynamics (CFD) is a well developed field with several computational tools. Thus to make use of existing tools of CFD we treat the mathematical models of a bio-membrane as fluid interface. The interface is commonly used for shape recognition of DNA, in biological pattern formation [74, 78, 83, 94, 129] (will be discussed in §1.4.2), tissue regeneration in wound healing and brain imaging in MRI [19, 79, 80]. In short, partial differential equations on surfaces arise in a variety of natural applications. This thesis is dedicated mainly to study mathematically and numerically partial differential equations on stationary and evolving in time surfaces of pattern forming models. For the case of surface partial differential equations the domain will be curved, or more precisely, a surface PDE is a partial differential equation whose domain is an d-dimensional curved (surface Γ) living in $\mathbb{R}^{d+1}$. For example, the Poisson equation on a surface:

$$-\Delta_\Gamma \rho = g, \qquad \text{on} \quad \Gamma. \tag{1.1}$$

Here Δ_Γ is the Laplace-Beltrami operator, the surface equivalent to the Laplace operator. Mathematical details will be addressed in next chapter. The simplest unsteady case, we consider is the heat equation on a surface,

$$\frac{\partial \rho}{\partial t} = \Delta_\Gamma \rho + g, \qquad \text{on} \quad \Gamma \times T, \tag{1.2}$$

$$\rho(\cdot,0) = \rho_0, \qquad \text{on} \quad \Gamma. \tag{1.3}$$

Suppose that the boundary of the surface is empty. For the case of non-empty boundaries of the surface, one can assume and impose the required boundary conditions. Now consider partial differential equations on an evolving d-dimensional surface $\Gamma(t)$ for $t \in [0,T]$. For example, the transport equation on evolving in time surface:

$$\frac{\partial^* \rho}{\partial t} = \Delta_{\Gamma(t)} \rho + g, \text{ on } \Gamma(t) \times T. \tag{1.4}$$

Here, the derivative $\frac{\partial^* \rho}{\partial t}$ is due to the evolution of surface $\Gamma(t)$, which is responsible for additional terms involving convection due to surface evolution. Derivation of

the surface related equation will be discussed in the subsequent *Chapter 2*. The material derivative on the surface is defined as:

$$\frac{\partial^* \rho}{\partial t} = \partial_t^\bullet \rho + \rho \nabla_{\Gamma(t)} \cdot \boldsymbol{v}\,, \tag{1.5}$$

the evolution of $\Gamma(t)$ can be obtained by the Leibniz formula. In addition, $\partial_t^\bullet \rho = \partial_t \rho + \boldsymbol{v} \cdot \nabla \rho$ denotes the advective surface material derivative. The surface velocity $\boldsymbol{v} = \mathsf{V}\boldsymbol{n} + \boldsymbol{v}_S$ can be decomposed into velocity components in the normal direction $\mathsf{V}\boldsymbol{n}$, with $\boldsymbol{n}$ to be a surface outward normal vector, and velocity in the tangential direction is $\boldsymbol{v}_S$.

To solve these problems efficiently, one requires advanced mathematical modeling with fast, efficient and robust computational algorithms, which cover natural phenomena with physical characteristics on manifolds. Now we give an overview of the surface related numerical techniques and description of gradual developments in this direction.

Curves and surfaces belong to a class of manifolds which have an implicit or parametric representation. With a good representation in hand, we can define systems of PDEs on manifolds using differential tangential calculus and Riemannian geometry. For instance, we may assume curves or surfaces as lower dimensional manifolds which are embedded in the physical space, known as hypersurface. PDEs on a surface can be computed through different techniques, the most frequently used techniques include: level set methods [1, 91, 108, 109, 111], fast marching method [110, 111], phase field method [35, 64], closest point representation [67–69, 105, 121], parametrization and triangulation of the surface [33], bulk surface finite element method (FEM) [34], ALE surface FEM approach for surface PDEs and diffuse interface [36, 37], fully discrete FEM for evolving surface [28]. In some cases, combination of two or more approaches are used to solve surface PDEs. Each of the above mentioned methods and representation has its own advantages and disadvantages and are mostly dependent on the nature of the particular problem.

In parametrization methods a smooth coordinate system is imposed on the surface, the differential operators are expressed within these coordinates, afterwards the resulting equations are discretized. In other words, in this method manifolds are represented using a geometrical mapping from a parametric domain to physical space. Parametrization of the surface has few draw-backs as well, it may be challenging to derive for complicated geometries on manifolds. It requires surface patching, to connect several characterization neighborhood, sometime it is challenging to derive a new parametrization for each surface patch. The construction of the coordinate system can be complicated involving more non-constant coefficients and derivative terms, which may introduce artificial singularities at the poles in spherical coordinates [105]. It is revealed that surface parametrization mostly introduces distortion either in some area or through some angles [40]. Triangulation of the surface can be effective for particular classes of equations. In general, it lacks some essential geometric properties, e.g., it does not posses a well-defined

surface characteristics [47]. Surface normal and curvature are not clearly defined. Numerical properties like convergence of the scheme on triangulated surfaces are not clear as compared to Cartesian grids [47].

Ruuth and Merriman [105] discussed that the closest point method representation of surface give some advantages. Namely, it is more flexible to represent both open and closed surfaces without an orientation. They also noticed that objects having co-dimension two or higher, such as points, curves and collection of surfaces can be naturally accommodated using the closest point representation.

Phase field method is extensively used to model interfacial motion in multiphase flow [35, 98, 99]. To capture a diffuse interface it transforms Lagrangian coordinates into Eulerian formulation. It is used to solve PDEs on implicitly defined surfaces, which is mainly based on diffuse interface methods. The authors [98, 99] represented the surface by half of the level set of a phase field variable ϕ defined on the surface Γ contained in the domain $\Omega \subset \mathbb{R}^d$ for $d = 1,2,3$. They introduced the so-called diffuse interface function, which allows to rewrite parabolic and elliptic PDEs defined on surfaces into PDEs defined on simple Euclidean domain. This function is assumed to vanish outside the diffuse interface. This method is closely related to level set approaches to solve Eulerian representation of surface defined PDEs.

In the last few decades, the level set method [91, 111] has been used as a numerical technique for dynamically evolving manifolds. It is a great tool to solve problems involving changes in topology like surface deformation. In level set methods the surface Γ is represented as zero level set of a function ϕ defined in $\mathbb{R}^d$. One can rewrite PDEs in Eulerian coordinate and solve this new representation on a fixed Cartesian grid in a neighborhood of $\Gamma(t)$. The Eulerian presentation of PDEs on a surface can be derived simply by replacing surface derivatives with projections of derivatives in the embedding Euclidean space. The level set approach avoids the non convenient parametrization and triangulation of the surface, e.g., the normal $\boldsymbol{n}$ and mean curvature H can be calculated, simply by taking derivatives of the level set function ϕ. This approach also avoids the numerical evaluation of the curvature. Although the proposed method solves the resulting equations in one dimension higher, it can be solved in a fixed domain [27]. The level set method has been suggested by Dziuk and Elliott [27] for complex morphology, where the parametric approach may not be adequate to find solutions of PDEs on surfaces.

The application of PDEs on surface is interesting because they possess a variety of quite promising applications in several areas, such as fluid dynamics, solid mechanics, image processing and multi-phase flow. The level set method is successfully implemented for the numerical study of a high-order 3-D technological flow problem with optimization [128], a unified model for etching, deposition, and lithography [1], reaction-diffusion systems on deforming surface [5], image processing [70], transport equation on evolving implicit surface [27], chemotaxis model on stationary surface [113] and in 3-D brain aneurysm capturing [23].

Consequently, we will employ the level set method to describe PDEs on surface, which allows implicit prescription of the surface $\Gamma(t)$, more detailed descrip-

tion on the method will be discussed in *Chapter 2*.

Literature review reveals that PDEs on surface can give some undesirable and non-physical results [27]. In this context we use high-order flux correction approaches for advective dominated problems. The surface convection produce wiggles and kinks, which requires use of the numerical stabilization to avoid non-physical solutions. We use algebraic flux correction (AFC) of FCT/TVD-type to get a positivity preserving solution. More information on algebraic flux correction based finite element method of FCT/TVD-type can be found in [60, 61, 76] and Galerkin FEM discretization in the later chapters.

1.4 Application of surface PDEs

In case of more realistic modeling problems, most of the time, we have to solve PDEs which live on an evolving manifold. For the solution of PDEs on surfaces with aforementioned biological properties, theoretical and numerical challenges may be faced. The standard conservation laws for PDEs on evolving surface differ from that of domain defined PDEs. One has to prescribe the motion of the interface. Consequently, the modeling of physical phenomena on surfaces requires in-depth command in differential geometry. It is challenging to construct numerical schemes for the surface-driven PDEs. The construction of robust, efficient and accurate solvers for the system of PDEs on surface Γ, is needed. Since the convection of the surface evolution may create numerical kinks, we require a stabilized numerical scheme with positivity preserving property for the solution. The solvers should be able to deliver an appropriate numerical solution in a reasonable time frame. The spatio-temporal discretization and suitable coupling between equations have to be taken under consideration with construction and implementation of a high-order and positivity preserving technique for convection and chemotaxis dominated equation. It is realized that the evolution of the surface $\Gamma(t)$ at each time instant has to preserve the area. The occurrence of sharp edges in the boundary and surface discontinuity may lead to undesirable numerical solutions. The implicit implementation of the level set approach to prescribe the interface is not straightforward.

Boykov et al. [7] discussed an integral solution to the surface PDEs. The proposed method is able to compute gradient flows on hypersurface w.r.t. a general class of energy functional. This approach can handle the topological changes of the evolving interface, like level set method. The suggested method is able to use an implicit representation of the surface via geo-cut. A Galerkin formulation of the matched interface boundary method for the elliptic interface problems can be found in [138], they captured the interface via two sets of elements in two subdomains. Olshanskii et al. [90], Chernyshenko and Olshanskii [16], Olshanskii and Reusken [85, 87] derived and studied a variational formulation for a class of PDEs on evolving surface, for interested readers in well posedness and stability of solutions, error analysis we refer to their work on evolving surfaces [86, 88–90].

The purpose of the thesis is to propose a level set based finite element method with FCT/TVD stabilization for the PDEs on an evolving in time surfaces $\Gamma(t)$. We mainly discuss the modeling of surface PDEs, in addition we will suggest some improvement for the existing techniques to treat PDEs on surface. Furthermore, we will address the application of PDEs on evolving surface in computational biology, particularly we will demonstrate a number of simulation for chemotaxis and pattern formation.

The thesis encompasses two closely related phenomena of mathematical biology, chemotaxis and pattern formation. In the first part, the mathematical derivation and a priori error analysis for the surface PDEs are mapped. The second segment is devoted to illustrate underlying physical mechanisms through numerical simulation on surface. The mathematical models are studied and simulated using FCT/TVD stabilized implicit finite element level set based schemes.
We explain the theoretical background and mathematical development focusing on the numerical state of the art for two biological phenomena, namely chemotaxis and Turing patterns in this section.

1.4.1 Chemotaxis

Chemotaxis mechanism

Chemotaxis is derived from Greek suffix -taxis which means arrangements. It is a bio-chemical phenomenon, which gives a particular movement of chemicals in response to the stimuli [81]. The chemicals are either moving towards (chemo-attractant) or away (chemo-repellent) from the source, it can be food or environmental danger, respectively. To understand the terminology of chemotaxis we can rely on commonly used -taxis suffix, to name few, e.g., photo-taxis (movement w.r.t. light), geo-taxis (gravitational attraction) and etc. Chemotaxis describes and dictates the direction, according to gradient of chemical substances. It could be either positive or negative chemotaxis, depending on the direction to the chemical gradient. The movement is controlled through the chemo-sensitivity parameter. In biological science, we take a simple example of the bacterium E. COLI, which obeys chemotaxis, swims towards a favorable environment in search of food (chemo-attractant) and moves away from unfavorable environment like toxin (chemo-repellent), depending upon the chemo-sensitivity parameter χ.

Chemotaxis is a peculiar behavior, which exists in a wide variety of living organism, ranging from macro- to micro-organisms, in their motile response to chemical stimuli [117]. For example, in nature it helps many species e.g., turtles to travel over thousands of miles for its breeding. This happens through detection of some chemical stimuli. In addition, several species of sharks have the ability to sense blood in water, being miles away from the actual source. Chemotaxis is intensively used throughout biology e.g., in the immune systems the leukocyte cell; which are produced in response to bacteria is based on chemotaxis mechanism. Theoretical results show that chemotaxis processes occur during healing

of wound [48]. Chemotaxis is naturally composed of two correlated but independent processes called motility and directionality, which are regulated under cellular stimuli. Now the mathematical development in chemotaxis will be addressed.

Mathematical development

The mathematical investigation of chemotaxis started in early 1970 after the pioneering work of Keller and Segel [54, 55]. They studied the mathematical modeling of slime mold aggregation, actually they were inspired by a tiny character called Dicty amoebae. Later on, they observed that E. COLI is traveling at a constant speed when the bacteria are placed in one end of a tube containing sources. The bacteria move towards higher concentrations of chemical [56] due to chemotaxis mechanisms. Mathematically, the most general model for chemotaxis phenomena can be described by the following system of reaction-diffusion advection or chemotaxis like equations [114, 117].

$$\frac{\partial c^i}{\partial t} = D_c^i \Delta c^i - \nabla \cdot \left[\chi_c^i \mathbf{w}_c^i(\boldsymbol{c},\boldsymbol{\rho}) c^i\right] + f^i(\boldsymbol{c},\boldsymbol{\rho}) \text{ in } \Omega \times T\,, \tag{1.6}$$

$$\frac{\partial^* \rho^j}{\partial t} = D_\rho^j \Delta_{\Gamma(t)} \rho^j - \nabla_{\Gamma(t)} \cdot (\chi_\rho^j \mathbf{w}_\rho^j(\boldsymbol{c},\boldsymbol{\rho}) \rho^j) + g^j(\boldsymbol{c},\boldsymbol{\rho}) \text{ on } \Gamma(t) \times T\,. \tag{1.7}$$

Here χ is the chemo-sensitivity parameter, $\chi \geqslant 0$ shows chemo-attractant and $\chi < 0$ indicates chemo-repellent. The description of such model will be discussed in *Chapter 3*. For a certain parameter setting in the system (1.6) and (1.7), we can get a desired model of reaction-diffusion and/or chemotaxis.

Minimal model

From the general system of equations (1.6) and (1.7) e.g., for the following set of parameters

$$i, j = 1, \quad D_c^i = 1, \quad \chi_c^i = \chi, \quad \mathbf{w}_c^i = \nabla\rho \quad \text{and} \quad f^i(c,\rho) = 0\,,$$

$$D_\rho^j = D^\rho, \quad \chi_\rho^j = \chi, \quad \mathbf{w}_\rho^i = 0, \quad \text{and} \quad g^j(c,\rho) = -c + \rho\,,$$

the minimal model of chemotaxis reads

$$\begin{aligned} c_t &= \Delta c - \nabla \cdot (\chi c \nabla \rho) \qquad \text{in} \qquad \Omega \times T\,, \\ \rho_t &= D^\rho \Delta \rho - c + \rho \qquad \text{on} \qquad \Gamma \times T\,. \end{aligned}$$

The historical development of the minimal model of chemotaxis can be found in [117].

Kinetic model

We obtain the following kinetic model:

$$\begin{aligned} c_t &= \nabla\cdot(D^c\nabla c)-\nabla\cdot(c\chi\nabla\rho)+c(1-c)(c-a) \text{ in } \Omega\times T\,,\\ \rho_t &= \Delta\rho-\alpha\rho+c \text{ on } \Gamma\times T\,, \end{aligned}$$

for the following parameter setting in the general system of equations (1.6) and (1.7),

$$i=1,\quad D^i_c=D^c,\quad \chi^i_c=\chi,\quad \mathbf{w}^i_c=\nabla\rho\quad\text{and}\quad f^i(c,\rho)=c(1-c)(c-a)\,,$$
$$j=1,\quad D^j_\rho=1,\quad \chi^j_\rho=1,\quad \mathbf{w}^j_\rho=0\quad\text{and}\quad g^j(c,\rho)=-\alpha\rho+c\,.$$

Mostly complex patterns formation occur due to the kinetic models [11, 113, 117, 120].

Mimura-Tsujikawa model

We get the Mimura-Tsujikawa model [73, 113, 118, 120] on surface:

$$c_t = D^c\Delta c-\alpha c+\beta\rho \text{ in } \Omega\times T\,, \tag{1.8}$$

$$\frac{\partial^*\rho}{\partial t} = D^\rho\Delta_{\Gamma(t)}\rho-\nabla\cdot(\chi\rho\nabla_{\Gamma(t)}c)+\rho(1-\rho) \text{ on } \Gamma(t)\times T\,. \tag{1.9}$$

We arrive at this model by considering the following coefficients in the general system of equations:

$$i=1,\quad D^i_c=D^c,\quad \chi^i_c=\chi,\quad \mathbf{w}^i_c=0\quad\text{and}\quad f^i(c,\rho)=-\alpha c+\beta\rho\,,$$
$$j=1,\quad D^j_\rho=D^\rho,\quad \chi^j_\rho=\chi,\quad \mathbf{w}^j_\rho=\nabla c\quad\text{and}\quad g^j(c,\rho)=\rho(1-\rho)\,.$$

This model admits evolving patterns, which will be discussed in §5.2.4.

From the introductory text and mathematical formulation on chemotaxis, we can deduce that it is working under signaling mechanisms based on source terms. The source can be food and/or environmental threat, broadly speaking, in cell biology via this process a cell migrates along a shallow chemo-attractant gradient. For more details on signaling mechanisms for regulation of chemotaxis, we refer to Wu [137]. Furthermore, Willard and Devreotes [136] noted that the social amoebae, (cf. DICTYOSTELIUM DISCOIDEUM) rely on chemotaxis signaling to find food for survival during starvation. Thus chemotaxis models can be used in several bio-medical applications. One of the useful applications of chemotaxis signaling is chemotherapy to control the growth of the cancerous cells e.g., see Condeelis et al. [21]. The laser ablation experiments have also allowed identification of sensory neurons and inter-neurons. The molecular neurogenetics of chemotaxis in C. ELEGANS including the identification of sensory neurons are important for animals life. In addition, the molecular and cellular analysis of chemotaxis in C. ELEGANS

are assumed to be a model mechanism. Moreover, Mori and Ohshima [77] provide more significant implications for the molecular basis of sensory systems in animals.

Keller and Segel [56] published their seminal work on chemotaxis in early 1970. Since 1980's state of the art work has been published on the numerical solution of several chemotaxis models. Some interesting mathematical questions arise in the context of the chemotaxis-driven systems, e.g., the modeling of the chemotaxis and angiogenesis [112], the global existence of solution to a chemotaxis hyperbolic and parabolic models [142], the random walks, aggregation and collapse [92], blow-ups in the Keller-Segel model [39], nonlinear aspects in chemotaxis [17], existence of solution [140] and etc.

In a series of articles, Tyson et al. [131, 132] studied the chemotaxis bacterial patterns in liquid medium and also introduce the fractional step methods to a chemotaxis model. Aida et al. [2] discussed a lower estimate for a chemotaxis growth system, they also showed that the numerical computation of the model contained several pattern solutions. In a series of articles, a flexible and algebraic flux-corrected finite element solver for chemotaxis is developed by Strehl et al. [118, 119]. The 3-D chemotaxis model is studied in [120], it is also assuring the positivity preserving property. The statistical and mathematical modeling of chemotaxis on stationary surfaces for 2-D and 3-D are discussed by Strehl [117], more details on blow-up and its remedy such as flux correction techniques on several chemotaxis models including Keller-Segel model can be found in their joint work [113, 118–120] as well.

For general understanding of mathematical development in chemotaxis mechanisms we refer to the seminal work of Keller and Segel [54, 55]. The mathematical modeling and numerical investigation of chemotaxis model on stationary surface can be found in [117–119].

A large part of the aforementioned work has been studied on Euclidean domains. The modeling and implementation gets complicated to study an evolving surface. Mostly natural phenomena evolve in time. For example, biological surfaces like animal coat and membranes also evolve in time. To model such problems in a realistic way; we will rely on basic concepts and mechanisms of differential geometry and application [14, 15, 96]. The complexity of the physical model increases due to that of evolving surface, the mathematical modeling of the phenomena on surface adds extra terms in the equation [116], which are challenging to solve numerically. The convection due to surface evolution and Laplace-Beltrami operators increases the difficulty level to find the solution of the problem. Elliott et al. [38] described a mathematical modeling and finite element solution of the cell motility and chemotaxis on evolving surface. They also discussed the interaction of several factors that act normal to the surface including internal and external forces which may be produced due to pressure or internal chemical reactions and polarization of the cell membrane. We will suggest and develop a stabilized finite element level set method for stationary and evolving in time surface with possible application for advection or chemotaxis like PDEs.

1.4.2 Turing-type instability

Biology of patterns emerged as an enthralled branch of research after the ground breaking work of A. Turing (1952) on morphogenesis [129]. Morphogenesis is a part of embryology dealing with forms and pattern formation [4]. The concept of Turing patterns has been applied to a wide variety of systems, the diverse areas include astrophysics formation of galaxies [84], ecology [107], hydrodynamics [135], material science [58], signaling network [98] and physics of semi-conductors [4].

Apart from the above discussed applications, the pattern formation in biology is a wide research field with several open questions, such as the understanding of pattern formation in zygote, animal coat [78], spots on butterfly [83], and many more underexplored areas to work. A large area of experimental and theoretical research is devoted to understand the science of pattern. Alan Turing in his seminal work [129] proposed that under certain conditions, chemicals can react and diffuse in such a way that they can produce steady state patterns, known as Turing instability. Although conventionally diffusion is treated as a stabilizing factor but in diffusion-driven instability it plays an important new role. A diffusion based instability occurs if the homogeneous steady state is stable to small perturbations in the absence of diffusion, but unstable to a small spatial perturbation in the presence of diffusion, as presented by Painter [94].

The classical work of Turing (1952) showed that many different patterns in nature can be modeled by a simple system of reaction-diffusion equations. In general, the biological membrane are not stationary. They are evolving in time, in consequence, we model such phenomena to investigate the biological models on evolving in time surfaces. The numerical experiments suggest that similar reaction-diffusion systems posed on evolving biological surfaces can exhibit a diffusion-driven instability of spatially uniform structures and thus lead to spatial patterns and forms, an example of such a model comes from the growth of solid tumors and patterns of animal skin.

The mathematical model of the diffusion-driven Turing type instability on a surface $\Gamma(t)$ can be found through exploring the following system of equations:

$$\frac{\partial^* \rho}{\partial t} = D^{\rho}\Delta_{\Gamma(t)}\rho + f(\rho,\zeta) \text{ on } \Gamma(t)\times T\,, \tag{1.10}$$

$$\frac{\partial^* \zeta}{\partial t} = D^{\zeta}\Delta_{\Gamma(t)}\zeta + g(\rho,\zeta) \text{ on } \Gamma(t)\times T\,, \tag{1.11}$$

where $\partial^*\rho/\partial t$ and $\partial^*\zeta/\partial t$ are time derivatives, which take into account the evolution of $\Gamma(t)$, and the Laplace-Beltrami operator $\Delta_{\Gamma(t)}$ on $\Gamma(t)$ will be discussed in details in next chapters. The corresponding initial and boundary conditions need to be provided, which vary with respect to physical models. The unknown functions $\rho(\mathbf{x},t)$ and $\zeta(\mathbf{x},t)$ are however defined on the surface-time domain $\Gamma(t)\times T$ and are solutions of the system (1.10) and (1.11), respectively. The parameters D^{ρ} and D^{ζ} are the positive diffusion coefficients, $f(\rho,\zeta)$ and $g(\rho,\zeta)$ are the reaction-kinetic

terms which are responsible for the interactions between the two surface concentrations. The reactive-kinetic itself is responsible for a large number of models, for example, the Schnakenberg model and activator and inhibitor model or Koch-Meinhard reaction-diffusion model, will be discussed in the subsequent chapters. In case of the Schnakenberg model [65], the reactive terms reads:

$$f(\rho,\zeta) = \gamma(a-\rho+\rho^2\zeta) \quad \text{and} \quad g(\rho,\zeta) = \gamma(b-\rho^2\zeta)\,,$$

where γ, a and b are positive constants. A thorough numerical investigation of this model will be discussed in §5.2.2. Furthermore, Koch and Meinhardt [57] introduced the following reactive kinetic model:

$$f(\rho,\zeta) = \alpha_1\rho\left(1-r_1\zeta^2\right) - \zeta\left(1-r_2\rho\right),$$

$$g(\rho,\zeta) = \beta_1\zeta\left(1+\frac{\alpha_1 r_1}{\beta_1}\rho\zeta\right) + \rho\left(\gamma_1 - r_2\zeta\right),$$

here α_1 and β_1 are constants. A rigorous numerical study of the Koch-Meinhardt reaction-diffusion model will be addressed in §5.2.3.

Numerical investigation of similar models has been studied by Bergdorf et al. [5] using Lagrangian particle methods based on the level set technique and by Barreira et al. [3] using surface finite element method. A closely related model for brain growth was studied numerically by Lefevre and Mangin [63]. The reaction-diffusion equations have been widely used for pattern-formatting process in biology, the patterns based on diffusion-driven Turing instability are obtained from a spatially uniform state developed via approximating a 2-D system, as discussed by Ouyang and Swinney [93]. The dynamics of Turing-type mechanism for yeast cell polarity are studied by Goryachev and Pokhilko [45]. As the study of Turing patterns is influential and important for the understanding of the biological forms, here on detail biomathematical study of the phenomena, we refer interested readers to the extensive work of Murray [78, 79]. In addition, the experimental basis for Turing patterns was initially observed by Castets et al. [13] through reaction of CHLORIDE IONIC MALONIC ACID. Gierer and Meinhardt [42] extended the idea of diffusion-driven instability through a paradigm-shift, and introduced principals for activation/inhibition models. Neilson et al. [81] and Elliott et al. [38] further extended the same idea in cell motility using a fourth order geometric reaction-diffusion system known as the Meinhardt model [42].

The analytical and numerical investigation of Turing patterns shows that they are highly dependent on several factors including the geometry of the domain and initial condition [79, 80, 94, 133]. The patterns are developed only under particular points of parametric space, or so-called Turing space used by Painter [94]. This shows that an adjustment of parameter setting is essential to catch well developed forms of Turing patterns. In developmental biology, the complexity of animal coats attracted many interdisciplinary researchers, to name few, French and Brakefield [41] and Nijhout [83]. They explored the mechanism behind eye-spot patterns

on the butterfly wings. The characterization of several diffusion-driven Turing instability on evolving domains are investigated by Venkataraman [133] and Hetzer et al. [50].

In the current work, we develop numerical simulation techniques for mathematical models of PDEs on the stationary and evolving in time surfaces. We demonstrate extensive numerical experiments based on underlying biological mechanism and principles which exhibit patterning. The pattern formation can be helpful in understanding the complex biological problems.

1.5 Outline

The main focus of this thesis is the mathematical modeling and construction of a level set based FCT/TVD finite element method for the solution of PDEs on evolving manifolds. Stabilized FEM solution of the advection-diffusion-reaction equation with application to realistic biological problems is addressed. We will introduce the Galerkin FEM methods, and provide a short note on trial and test spaces, $L^2(\Omega)$ and $H^1(\Omega)$-errors and order of convergence analysis. Moreover, we will address derivation of PDEs on surfaces including theoretical results, based on proofs of theorems and lemmas. These results will be used throughout the thesis to treat PDEs on surfaces. Finally we will be able to construct and deliver a robust and accurate FEM based numerical scheme for surface PDEs. The remaining chapters are outlined as follows:

In *Chapter 2*, we present the basic mathematical definitions, proofs of several lemmas and theorems which will be used throughout the thesis. We introduce the derivation of the PDEs on surfaces, including the geometrical quantities like curvature, normal, tangent, mean curvature H and etc. In addition, the gradient, divergence and Laplace-Beltrami operators for PDEs on surfaces are defined. We derive the transport equation on the surface, because most equations in the subsequent chapters are based on this fundamental equation. In addition, proofs of related formulae, to name few, mean curvature formula, coarea formula, integration by parts on surface for scalar and vector functions are discussed.

The *Chapter 3* demonstrates the discretization techniques. We will discuss basics of the finite element method for spatial discretization of PDEs, for temporal discretization we will discuss some commonly used schemes, the implementation of such schemes can be found in FEATFLOW [1]. The Laplace-Beltrami operator for surface PDEs is introduced and the basic algorithms of required stabilization techniques for convective dominated surface PDEs are shown. We prove results related to a priori error estimates for this formulation and finally the surface triangulation will be addressed as well.

[1] `http://www.featflow.de`

In *Chapter 4*, we present the numerical simulation of the partial differential equations on surfaces. We discuss both PDEs on stationary and evolving in time surfaces. We design a physically motivated positivity preserving finite element method to provide an accurate and robust numerical scheme for surface PDEs. To avoid non-physical oscillations due to surface convection or chemotaxis like PDEs, we further extend the methods with FCT/TVD stabilization schemes. We study the Galerkin approach with and without stabilization and analyze the results. The numerical accuracy of the solution profiles are demonstrated. The content of *Chapter 2* and *Chapter 3* including some numerical results from *Chapter 4* were published as joint article with A. Sokolov and S. Turek in a research article in journal of computational and applied mathematics [114].

In *Chapter 5*, we focus on the application of the finite element method for surface PDEs to the mechanisms of the Turing patterns. We design efficient and robust level set based FEM for different models which exhibit Turing patterns on the surface. Moreover, we investigate the accuracy of the method for the solution of the discretized systems arising from biological applications. The contents and numerical results from this chapter are archived in an internal report at department of applied mathematics, TU-Dortmund co-author with A. Sokolov, R. Strehl and S. Turek [115].

In *Chapter 6*, we summarize surface finite element methods focusing on biological applications studied in this work and present future works as an outlook of the current research. The conclusion and future outlook are summarized for further possibility on extension of the work for more realistic biological problems on surfaces.

Part I

Derivation of PDEs on surface and discretization scheme

Nature is a book written in the language of mathematics.

G. Galilei, Il Saggiatore, 1632

2

Modeling of the surface defined PDEs

In this chapter, we introduce the basic differential geometry concepts including definitions and derivations of surface related equations. Moreover, these concepts are used to derive and discuss few peculiar characteristics of PDEs on surfaces. Since we used different meshes to reflect the smooth geometry of two/three dimensional surfaces embedded in $\mathbb{R}^d$ for $d = 2,3$. We know that mesh are not smooth enough to notice the instinct characteristics in $\mathbb{R}^d$, particularly for $d \geq 3$. In consequences, to implement PDEs on evolving manifolds we are using the differential calculus on manifolds. Roughly speaking, the manifolds locally look like d-dimensional Euclidean domain in $\mathbb{R}^d$. We provide a short and brief note on the basic language of differential geometry. Thus starting with definition of the surface and explain the theory of surface related literature. There are a large number of advance techniques to encounter PDEs on surfaces, most commonly used methods include the level set approaches [108, 111], the parametrized boundary methods [29] and the phase field methods [99]. In the present work we use the level set methods to capture the interface of PDEs on an evolving manifold. Moreover, results concerning to level set methods will be derived. In addition, we provide proof of theorems and lemmas to treat surface PDEs with the level set methods.

2.1 Mathematical modeling

Definition 1. *(Surface)*
A smooth surface is a subset $\Gamma \subset \mathbb{R}^3$ such that each point has a neighborhood $U \subset \Gamma$ and a mapping define from an open set $V \subset \mathbb{R}^2$ as $\mathbf{x} : V \to \mathbb{R}^3$,

- *The function $\mathbf{x}$ is a bijection that continuously maps V into U and the inverse function exists and continuous. In other way, the mapping $\mathbf{x} : V \to U$ is a homeomorphism.*
- *The function $\mathbf{x}(u^1, u^2)$ has derivatives of all orders.*
- *The first derivative, s.t., $\mathbf{x}_1 = \frac{d\mathbf{x}}{du^1}$ and $\mathbf{x}_2 = \frac{d\mathbf{x}}{du^2}$ are linearly independent at all points.*

The map $\mathbf{x}$ is known as local parametrization or local chart on the surface. The above properties identify that the surface Γ is continuous, invertible and smoothly

embedded to the ambient space. The differential $d\mathbf{x}$ is represented by the Jacobian of $\mathbf{x}(u^1,u^2)$, which maps the directions in the parametric domain to elements in the tangent space $T_p\Gamma$ at any arbitrary point p.

Hypersurface is the generalization of the ordinary surface in 3-dimensional space and the dimension of a hypersurface is one less than that of its ambient space.

Definition 2. *Hypersurface and space of tangent vector:*
Let $\alpha \in \mathbb{R}$ and $\Gamma \in \mathbb{R}^3$ be a level set of function ϕ i.e., $\Gamma = \Gamma_r := \{\mathbf{x} \in \mathbb{R}^3, \phi(\mathbf{x}) = r\}$, where ϕ is a C^α-function. Then Γ is called a C^α-hypersurface, if $\nabla\phi \neq 0$ at all points on Γ.

The tangent space $T_p\Gamma$ to a smooth surface Γ at a point p is spanned by the two vectors $\mathbf{x}_1$ and $\mathbf{x}_2$ which are orthogonal to $(\nabla\phi)_p$.
The tangent space contains all directional derivatives of curves on the manifold passing through the point p. Given that $\mathbf{x}(\tau) : (-\varepsilon,\varepsilon) \subset \mathbb{R} \to \Gamma$ with $\mathbf{x}(0) = p$ then $\frac{\partial \mathbf{x}}{\partial \tau} \in T_p\Gamma$ as illustrated in figure 2.1.

Now, we have motivation to define two main properties of the surface, known as the first and second fundamental forms. These properties are quite interesting and helpful to calculate characteristics of mathematical entities on the surface.

2.1.1 The first fundamental form

In differential geometry the first fundamental form of a surface in $\mathbb{R}^d$ induce canonically by taking the inner product of a general velocity vector with itself. Once constructed a parametrization of a curve it will allow us to calculate surface properties such as arc length, area and curvature of the curve.

Let s be the parametric arc length of curve $\mathscr{C}$, the parametrization of $\mathscr{C}$ is define by:

$$\mathscr{C} = \{\mathbf{x}(u^1(\tau),u^2(\tau)), \quad \text{where} \quad \tau \in [a,b] \subset \mathbb{R}\}.$$

We have the following relation on the surface

$$ds^2 = \left\langle \dot{\mathbf{x}}\left(u^1(\tau),u^2(\tau)\right), \dot{\mathbf{x}}\left(u^1(\tau),u^2(\tau)\right)\right\rangle d\tau^2,$$

here, $\dot{\mathbf{x}}$ is derivative with respect to variable τ. We define the following transformation

$$\mathbf{x} = \mathbf{x}(u^1(\tau),u^2(\tau)) : I \to \mathbb{R}^d.$$

Simply using chain rule, and denoting $\mathbf{x}_1 = \frac{d\mathbf{x}}{du^1}$ and $\mathbf{x}_2 = \frac{d\mathbf{x}}{du^2}$ we have

$$ds^2 = \left\langle \mathbf{x}_1\left(\frac{du^1}{d\tau}\right) + \mathbf{x}_2\left(\frac{du^2}{d\tau}\right), \mathbf{x}_1\left(\frac{du^1}{d\tau}\right) + \mathbf{x}_2\left(\frac{du^2}{d\tau}\right)\right\rangle d\tau^2.$$

The tangent space generates the surface through $T_p\Gamma = span\{\mathbf{x}_1, \mathbf{x}_2\}$ at point p implies that $\mathbf{x}_1, \mathbf{x}_2 \in T\Gamma$.

$$ds^2 = \langle \mathbf{x}_1, \mathbf{x}_1 \rangle \left(\frac{du^1 du^1}{d\tau^2} \right) d\tau^2 + 2 \langle \mathbf{x}_1, \mathbf{x}_2 \rangle \left(\frac{du^1}{d\tau} \right) \left(\frac{du^2}{dt} \right) d\tau^2 + \langle \mathbf{x}_1, \mathbf{x}_2 \rangle \left(\frac{du^2 du^2}{d\tau^2} \right) d\tau^2.$$

In the simplified form, we have

$$ds^2 = \langle \mathbf{x}_1, \mathbf{x}_1 \rangle (du^1)^2 + 2 \langle \mathbf{x}_1, \mathbf{x}_2 \rangle (du^1)(du^2) + \langle \mathbf{x}_2, \mathbf{x}_2 \rangle (du^2)^2. \tag{2.1}$$

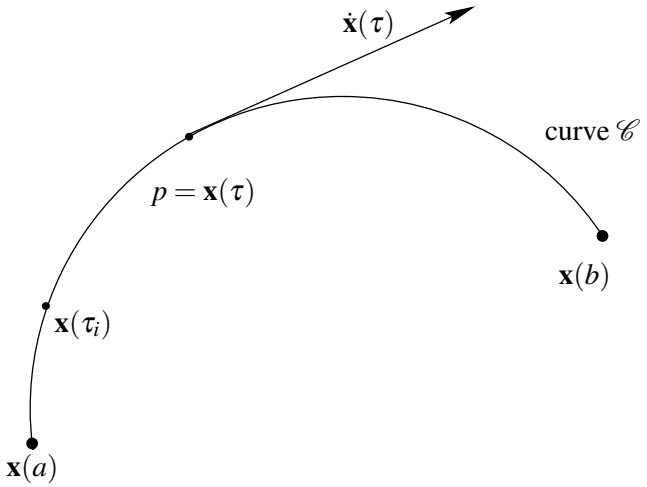

Figure 2.1: Parametrization of curve $\mathscr{C}$.

$$ds^2 = E(du^1)^2 + 2F du^1 du^2 + G(du^2)^2, \tag{2.2}$$

with $E = g_{11} = \langle \mathbf{x}_1, \mathbf{x}_1 \rangle$, $F = g_{12} = \langle \mathbf{x}_1, \mathbf{x}_2 \rangle$ and $G = g_{22} = \langle \mathbf{x}_2, \mathbf{x}_2 \rangle$ are coefficients of the first fundamental form. The matrices are much systematic to compute and evaluate thus the matrix form of the first fundamental form is given by:

$$ds^2 = \begin{pmatrix} du^1 & du^2 \end{pmatrix} \begin{pmatrix} g_{11} & g_{12} \\ g_{21} & g_{22} \end{pmatrix} \begin{pmatrix} du^1 \\ du^2 \end{pmatrix}. \tag{2.3}$$

The equations (2.2) and (2.3) are useful representation of the first fundamental form.These are mostly used to measure the arc length of the curve. From equation (2.2) we can clearly observe that the first fundamental form is a quadratic and bi-linear form. In addition, the first fundamental form is used to encodes angle between curves on the surface. It is closely tied with the isometries of the surface. The coefficients of the first fundamental form are represented through the following matrix:

$$\mathscr{G} = \{g_{ij}\} = \begin{pmatrix} g_{11} & g_{12} \\ g_{21} & g_{22} \end{pmatrix}. \tag{2.4}$$

Where $\mathscr{G}$ is known as Riemannian metric, will be used to determine geometric values of the hypersurfaces/manifolds.

2.1.2 The second fundamental form

Suppose we have a surface in $\mathbb{R}^d$, assume that we push or pull the surface along in the normal direction. Then we will get a family of surfaces. On the one hand, the first fundamental form will calculate the arc length and on the other hand, the second fundamental form will encodes how the arc length changes, as the surface moves along the normal direction.

Let $\mathbf{x}(u^1,u^2)$ parametrization of a curve for $d=2$ and assume that the initial value $\mathbf{x}(0,0)=0$. Since $\mathbf{x}_1=\frac{d\mathbf{x}}{du^1}$ and $\mathbf{x}_2=\frac{d\mathbf{x}}{du^2}$ for simplicity we are assuming

$$\mathbf{x}_{11}=\frac{d\mathbf{x}(u^1,u^2)}{du^1du^1},\quad \mathbf{x}_{12}=\frac{d\mathbf{x}(u^1,u^2)}{du^1du^2}\quad \text{and}\quad \mathbf{x}_{22}=\frac{d\mathbf{x}(u^1,u^2)}{du^2du^2}.$$

The Taylor series expansion at $(0,0)$ gives

$$\begin{aligned}\mathbf{x}(u^1,u^2) &= \mathbf{x}(0,0)+\mathbf{x}_1(0,0)du^1+\mathbf{x}_2(0,0)du^2+\frac{1}{2}\mathbf{x}_{11}(0,0)(du^1)^2\\ &+ \mathbf{x}_{12}(0,0)du^1du^2+\frac{1}{2}\mathbf{x}_{22}(0,0)(du^2)^2+\mathscr{O}\left((du^1)^2,(du^2)^2\right)\end{aligned}\tag{2.5}$$

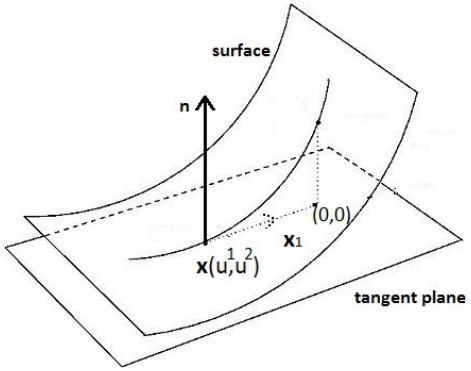

Figure 2.2: $\mathbf{x}_1$ and $\mathbf{x}_2$ generating the tangent plane

Let $\boldsymbol{n}$ be the normal vector to $T_p\Gamma$ at point p. Since the tangent space of Γ is $T_p\Gamma=span\{\mathbf{x}_1,\mathbf{x}_2\}$ then we have

$$\langle\mathbf{x}_1,\boldsymbol{n}\rangle=\langle\mathbf{x}_2,\boldsymbol{n}\rangle=0.$$

Now taking the dot product of equation (2.5) with the normal vector $\boldsymbol{n}$, we have

$$\begin{aligned}\left\langle\mathbf{x}(u^1,u^2),\boldsymbol{n}\right\rangle &= \langle\mathbf{x}(0,0),\boldsymbol{n}\rangle+\langle\mathbf{x}_1(0,0),\boldsymbol{n}\rangle du^1+\langle\mathbf{x}_2(0,0),\boldsymbol{n}\rangle du^2+\frac{1}{2}\langle\mathbf{x}_{11}(0,0),\boldsymbol{n}\rangle(du^1)^2\\ &+\langle\mathbf{x}_{12}(0,0),\boldsymbol{n}\rangle du^1du^2+\frac{1}{2}\langle\mathbf{x}_{22}(0,0),\boldsymbol{n}\rangle(du^2)^2+\mathscr{O}\left((du^1)^2,(du^2)^2\right).\end{aligned}$$

Using the initial value and the fact that $\mathbf{x}_1$ and $\mathbf{x}_2$ are in the tangent plane, we get the following relation for the second fundamental form.

$$II = 2\left\langle \mathbf{x}(u^1,u^2), \boldsymbol{n}\right\rangle = \langle \mathbf{x}_{11}, \boldsymbol{n}\rangle (du^1)^2 + 2\langle \mathbf{x}_{12}, \boldsymbol{n}\rangle du^1 du^2 + \langle \mathbf{x}_{22}, \boldsymbol{n}\rangle (du^2)^2,$$

here denoting the coefficients $b_{11} = \langle \mathbf{x}_{11}, \boldsymbol{n}\rangle$, $b_{12} = \langle \mathbf{x}_{12}, \boldsymbol{n}\rangle$ and $b_{22} = \langle \mathbf{x}_{22}, \boldsymbol{n}\rangle$. The matrix representation is given by

$$II = \begin{pmatrix} du^1 & du^2 \end{pmatrix} \begin{pmatrix} b_{11} & b_{12} \\ b_{21} & b_{22} \end{pmatrix} \begin{pmatrix} du^1 \\ du^2 \end{pmatrix}.$$

Where the coefficients of the second fundamental form are represented through the following matrix

$$\mathscr{B} = \{b_{ij}\} = \begin{pmatrix} b_{11} & b_{12} \\ b_{21} & b_{22} \end{pmatrix}. \tag{2.6}$$

The second fundamental form is a quadratic form, defined on the tangent space. Moreover, a surface can be uniquely determined through the coefficients of first and second fundamental form. A general description and interpretation including advance applications of the fundamental forms can be found in an extensive work of Chase[14] and Pressley[96].

Definition 3. *If the fundamental forms are vanishing at a point, then the surface is planar at that point.*
If coefficients of the second fundamental form are zero, then

$$\mathbf{x}_1 \cdot \boldsymbol{n}_1 = \mathbf{x}_1 \cdot \boldsymbol{n}_2 = \mathbf{x}_2 \cdot \boldsymbol{n}_1 = \mathbf{x}_2 \cdot \boldsymbol{n}_2 = 0,$$

here, $\boldsymbol{n}_1 = \boldsymbol{n}_{u^1}$ and $\boldsymbol{n}_2 = \boldsymbol{n}_{u^2}$. As we know that $\mathbf{x}_1$ and $\mathbf{x}_2$ are linearly independent (e.g., see definition §1) and span the tangent plane this implies that we must have $\boldsymbol{n}_1$ and $\boldsymbol{n}_2$ orthogonal to the tangent plane [14]. Since $\boldsymbol{n}_1$ and $\boldsymbol{n}_2$ lie in the tangent plane. Therefore, $\boldsymbol{n}_1 = \boldsymbol{n}_2 = 0$, which implies that the normal vector $\boldsymbol{n}$ is constant. Then $(\mathbf{x}\cdot\boldsymbol{n})_{u^1} = \mathbf{x}_1 \cdot \boldsymbol{n} + \mathbf{x}\cdot 0 = 0 + 0 = 0$, similarly $(\mathbf{x}\cdot\boldsymbol{n})_{u^2} = 0$. It follows that at p the surface is tangent to the plane up to third order.

2.2 Differential operators on surface

We are interested to give more insight into the formulation of differential operators on surface Γ in the local coordinates. Now having on hands the surface properties based on fundamental forms, we will define and derive few useful differential operators on surface. Using vector calculus we can calculate gradient and divergence on surfaces for a differentiable function that will enable us to define Laplace-Beltrami operator Δ_Γ on surfaces.

2.2.1 Integration over the surface

To integrate over the surface Γ, we define a differentiable function f using atlas on a surface. Let $f : \Gamma \to \mathbb{R}$, using the fundamental forms we can measure the length of a curve on the surface by integrating the length of derivatives over an interval $I \in \mathbb{R}$. The norm of the vector in the parametric space w.r.t. metric induced by $\mathscr{G}$. The integral of a function is weighted by the infinitesimal area elements $du^1 du^2$. Where to integrate a function over Γ, we have to deform the area accordingly. The area spanned by $\mathbf{x}_1$ and $\mathbf{x}_2$ in parametric space is mapped to the area $\left|\mathbf{x}_1 \times \mathbf{x}_2\right|$ on the tangent space of the surface.

$$\langle \mathbf{x}_1, \mathbf{x}_2 \rangle = |\mathbf{x}_1||\mathbf{x}_2| \cos\Theta. \tag{2.7}$$

$$\left|\mathbf{x}_1 \times \mathbf{x}_2\right| = |\mathbf{x}_1||\mathbf{x}_2| \sin\Theta. \tag{2.8}$$

Where Θ is angle between $\mathbf{x}_1$and $\mathbf{x}_2$, simply squaring and adding equations (2.7) and (2.8), we obtain

$$\frac{\langle \mathbf{x}_1, \mathbf{x}_2 \rangle^2 + \left|\mathbf{x}_1 \times \mathbf{x}_2\right|^2}{|\mathbf{x}_1|^2 |\mathbf{x}_2|^2} = 1,$$

plugging the coefficients of the first fundamental form (2.4), we get

$$\left|\mathbf{x}_1 \times \mathbf{x}_2\right| = \sqrt{|\mathbf{x}_1|^2 |\mathbf{x}_2|^2 - \langle \mathbf{x}_1, \mathbf{x}_2 \rangle^2} = \sqrt{det\mathscr{G}}.$$

This calculation shows that the mapped area on the tangent space is related by coefficients of the fundamental forms. Thus the integration over a coordinate chart produce area defined by

$$\mathscr{A} = \int_{u^1} \int_{u^2} f(u^1, u^2) \sqrt{det\mathscr{G}(u^1, u^2)} du^1 du^2. \tag{2.9}$$

This integration is independent of parametrization and can be extended to the whole space [12, 49]. In addition, it is possible to define an inner product on the space of square integrable function on the surface.

$$\langle f, h \rangle = \int_{u^1} \int_{u^2} f(u^1, u^2) h(u^1, u^2) \sqrt{det\mathscr{G}(u^1, u^2)} du^1 du^2. \tag{2.10}$$

Now we will use the integration over surface induced by metric $\mathscr{G}$ to derive and calculate gradient, divergence and Laplace-Beltrami operators on the surfaces [12, 15, 49, 103].

2.2.2 The gradient on surface

The gradient maps a function $\rho : \mathbb{R}^d \to \mathbb{R}$ representing the direction of greatest increase in the function ρ and its magnitude corresponds to the slope of the function. Thus the gradient in the Euclidean space $\mathbb{R}^d$ is defined as:

$$\nabla \rho = \left(\frac{\partial \rho}{\partial x^1}, ..., \frac{\partial \rho}{\partial x^d} \right)^T. \tag{2.11}$$

The gradient of a function is also used to determine the directional derivatives $d\rho_p$ at a point p in the direction of the vector $\boldsymbol{\xi} \in \mathbb{R}^d$:

$$\langle \nabla \rho(p), \boldsymbol{\xi} \rangle = d\rho_p(\boldsymbol{\xi}), \quad \forall\, \boldsymbol{\xi} \in \mathbb{R}^d. \tag{2.12}$$

A simple way to calculate the directional derivative $d\rho_p(\boldsymbol{\xi})$ is by directly observing its behavior over variable τ

$$d\rho_p(\boldsymbol{\xi}) = \frac{d}{d\tau}\Big|_{\tau=\tau_o} \rho(p+\tau\boldsymbol{\xi}). \tag{2.13}$$

In a more general way, the generalized gradient for a surface using definition 2, given that $\gamma(\tau) : (-\varepsilon, \varepsilon) \to \Gamma \subset \mathbb{R}^d$ fulfill the criteria $\gamma(0) = p$, then $\dot{\gamma}(0) = \boldsymbol{\xi} \in T_p\Gamma$.

$$d\rho_p(\boldsymbol{\xi}) = \frac{d}{d\tau}\Big|_{\tau=\tau_o} \rho(\gamma(\tau)). \tag{2.14}$$

Now this equation can be used for Riemannian manifold with metric $\mathscr{G}$. Thus the directional derivative $d\rho_p(\boldsymbol{\xi})$ exists and fulfilling the conditions of γ. We can define gradient on manifold after reconstructing equation (2.12) into manifold notations, assuming that the function $\rho \in \Gamma$, the gradient is characterized by the following relation

$$\mathscr{G}\,\langle \nabla_\Gamma \rho(p), \boldsymbol{\xi} \rangle = d\rho_p(\boldsymbol{\xi}), \quad \forall\, \boldsymbol{\xi} \in T_p\Gamma. \tag{2.15}$$

To fulfill the above relations, this equation implies that one gradient exists for all $\boldsymbol{\xi} \in T_p\Gamma$. Now to calculate the gradient on hypersurface, we define a local chart with basis ∂_i. Since the gradient is an element of the tangent space we can write in the linear combination of the basis functions

$$\nabla_\Gamma \rho = \sum_{i=1}^{d} a^i \partial_i$$

similarly it is true for the $\boldsymbol{\xi} \in T_p\Gamma$

$$\boldsymbol{\xi} = \sum_{i=1}^{d} \xi^i \partial_i$$

since the directional derivatives are linear, now using the local coordinates u^i we can define as

$$d\rho_p(\boldsymbol{\xi}) = \sum_{i=1}^{d} \xi^i d\rho_p(\partial_i) = \sum_{i=1}^{d} \xi^i \frac{\partial \tilde{\rho}}{\partial u^i}. \tag{2.16}$$

The equation (2.16) can now be used to determine the values of the coefficients a^i by starting from equation (2.15),

$$\mathscr{G}\,\langle \nabla_\Gamma \rho, \boldsymbol{\xi} \rangle = \sum_{i,j=1}^{d} g_{ij} \xi^i a^j. \tag{2.17}$$

$$d\rho_p(\boldsymbol{\xi}) = \sum_{i=1}^{d} \xi^i \frac{\partial \tilde{\rho}}{\partial u^i}, \tag{2.18}$$

therefore, using equations (2.15), (2.17) and (2.18) we have

$$\sum_{i,j=1}^{d} g_{ij} a^j = \frac{\partial \tilde{\rho}}{\partial u^i} \quad \forall\ i, j. \tag{2.19}$$

This implies that

$$\mathscr{G} \cdot \boldsymbol{a} = \begin{pmatrix} \frac{\partial \tilde{\rho}}{\partial u^1} \\ \frac{\partial \tilde{\rho}}{\partial u^2} \\ \vdots \\ \frac{\partial \tilde{\rho}}{\partial u^d} \end{pmatrix}, \tag{2.20}$$

where $\boldsymbol{a} = (a^1, ..., a^d)^T$. After inverting the matrix $\mathscr{G}$, the elements of the inverse of g_{ij} are g^{ij} we obtain an expression for the elements of $\boldsymbol{a}$

$$\boldsymbol{a} = g^{ij} \cdot \begin{pmatrix} \frac{\partial \tilde{\rho}}{\partial u^1} \\ \frac{\partial \tilde{\rho}}{\partial u^2} \\ \vdots \\ \frac{\partial \tilde{\rho}}{\partial u^d} \end{pmatrix}, \tag{2.21}$$

thus we get the coefficients a^i as:

$$a^i = \sum_{i,j=1}^{d} g^{ij} \frac{\partial \tilde{\rho}}{\partial u^i}. \tag{2.22}$$

Finally, combining these terms, the gradient on the surface $\nabla_\Gamma \rho$ is define through the following relation:

$$\nabla_\Gamma \rho = \sum_{i,j=1}^{d} a^i \partial_i \quad \text{with} \quad a^i = \sum_{i,j=1}^{d} g^{ij} \frac{\partial \tilde{\rho}}{\partial u^i}. \tag{2.23}$$

2.2.3 The divergence on surface

The divergence is physically assumed as flow of material. It is an operator defined on a vector field $\boldsymbol{\xi} : \mathbb{R}^d \to \mathbb{R}$, it converts a vector field into a scalar field. The formula in a usual $\mathbb{R}^d$ is given by

$$\nabla \cdot \boldsymbol{\xi} = \sum_{i=1}^{d} \frac{\partial \xi^i}{\partial u^i}. \tag{2.24}$$

In general, the divergence at a point measure the suction and injection. Actually, it interprets the flow field, where the direction and the control volume of the flow

in a certain point is defined through the corresponding vector. Then the divergence operator will compute the current change in volume under the influence of vector field $\boldsymbol{\xi}$.

Let ρ is a smooth function with compact support over a vector field $\boldsymbol{\xi}$, the divergence is defined as the negative adjoint operator to the gradient [12, 49, 103],

$$\langle \boldsymbol{\xi}, \nabla_\Gamma \rho \rangle \quad = \quad -\langle div\boldsymbol{\xi}, \rho \rangle \,. \tag{2.25}$$

For integration over surface in $\mathbb{R}^d$, we have

$$\int_{\mathbb{R}^d} \rho \cdot div\boldsymbol{\xi} d\mathbf{x} \quad = \quad -\int_{\mathbb{R}^d} \langle \nabla_\Gamma \rho, \boldsymbol{\xi} \rangle \, d\mathbf{x}. \tag{2.26}$$

The equation (2.26) now can be changed into manifold by introducing $\mathscr{G}(\nabla_\Gamma \rho, \boldsymbol{\xi})$ instead of $\langle \nabla_\Gamma \rho, \boldsymbol{\xi} \rangle$ and replacing $d\mathbf{x} = \sqrt{det\mathscr{G}} d\Gamma$.

$$\int_\Gamma \tilde{\rho} \cdot div\boldsymbol{\xi} \sqrt{det\mathscr{G}} d\Gamma \quad = \quad -\int_\Gamma \mathscr{G}(\nabla_\Gamma \rho, \boldsymbol{\xi}) \sqrt{det\mathscr{G}} d\Gamma. \tag{2.27}$$

$$\int_\Gamma \tilde{\rho} \cdot div\boldsymbol{\xi} \sqrt{det\mathscr{G}} d\Gamma \quad = \quad -\int_\Gamma \sum_{i=1}^{d} \frac{\partial \tilde{\rho}}{\partial u^i} \xi^i \cdot \sqrt{det\mathscr{G}} d\Gamma. \tag{2.28}$$

Using integration by parts

$$\int_\Gamma \tilde{\rho} \cdot div\boldsymbol{\xi} \sqrt{det\mathscr{G}} d\Gamma \quad = \quad \int_\Gamma \tilde{\rho} \sum_{i=1}^{d} \frac{\partial}{\partial u^i} \left(\xi^i \cdot \sqrt{det\mathscr{G}} \right) d\Gamma. \tag{2.29}$$

If the support of all ρ contain in the local coordinates, the formula for the divergence of a vector field on the manifold is given by

$$div\boldsymbol{\xi} \quad = \quad \frac{1}{\sqrt{det\mathscr{G}}} \sum_{i=1}^{d} \frac{\partial}{\partial u^i} \left(\xi^i \cdot \sqrt{det\mathscr{G}} \right). \tag{2.30}$$

This expression is independent of parametrization.

2.2.4 The Laplace-Beltrami operator

The Laplace-Beltrami operator [12, 15, 49, 103] on surface is defined for a continuous function $\rho \in C^d$ is define through the following relation

$$\Delta_\Gamma(\bullet) \quad = \quad div_\Gamma \nabla_\Gamma(\bullet) \,,$$

using equations of the gradient (2.23) and the divergence (2.30) on surface, the Laplacian in the local coordinate is define as follows:

$$\Delta_\Gamma \rho \quad = \quad \frac{1}{\sqrt{det\mathscr{G}}} \sum_{i,j=1}^{d} \frac{\partial}{\partial u^i} \left(\sqrt{det\mathscr{G}} \cdot g^{ij} \cdot \frac{\partial \rho}{\partial u^i} \right). \tag{2.31}$$

This is the parametric representation of the Laplace-Beltrami operator. Roughly speaking, the Laplace operator can be seen as a generalization of the second order derivative ρ''. Using finite difference this derivative defined as

$$\rho'' = \lim_{h\to\infty} \frac{\rho(x+h)-2\rho(x)+\rho(x-h)}{2h^2}. \tag{2.32}$$

In numerical community, mesh is used as a discrete counterpart of the continuous surface, the Laplacian operator is applied to each vertex on mesh. For example for a function ρ defined in (2.32), the vector value represents the difference between the vertex and its neighboring vertices. Using the vectors representation, we can construct mesh of the surface. In addition, by constructing the location and set of vertices we can obtain a smooth deformation of the mesh.

Lemma 2.2.1. *The gradient on surface $\nabla_\Gamma\rho(x)$ in equation (2.23) depends only on the values of the function ρ on the boundary $\Gamma\cap U_\varepsilon$, where $U_\varepsilon\subset\mathbb{R}^{d+1}$ is a neighborhood of x.*

Proof. The proof of the lemma follows from [29], here it is sufficient to show that ρ is identically equal to zero on $\Gamma\cap U_\varepsilon$, $\Rightarrow \nabla_\Gamma\rho(x)=0$.
Define $\gamma:(-\varepsilon,\varepsilon)\to\mathbb{R}^{d+1}$ such that $\gamma(0)=x, \gamma(-\varepsilon,\varepsilon)\subset\Gamma\cap U_\varepsilon$ and $\gamma'(0)=\nabla_\Gamma\rho(x)$. Since $\bar\rho(\gamma(\tau))=\rho(\gamma(\tau))=0, \forall|\tau|<\varepsilon$.
This leads to:
$0=\nabla\bar\rho(x)\cdot\gamma'(0)=(\nabla_\Gamma\rho(x)+\nabla\bar\rho(x)\cdot\boldsymbol{n}(x)\boldsymbol{n}(x))\cdot\nabla_\Gamma\rho(x)=|\nabla_\Gamma\rho(x)|^2$,
this concludes proof of the result. □

Now we will derive and discuss formula for curvature established from the geometrical properties such as the fundamental forms §2.1.1–2.1.2.

Lemma 2.2.2. *(Curvature in terms of fundamental forms)*
Let the natural parametrization of a curve by $\mathbf{x}(u^1(s),u^2(s))$, $\boldsymbol{n}$ is normal vector and $\mathbf{x}_{u^1}$ and $\mathbf{x}_{u^2}$ are derivatives w.r.t. u^1 and u^2, for simplicity we will assume $\mathbf{x}_1$ and $\mathbf{x}_2$ respectively. Calculating derivatives w.r.t. arc length s, we have

$$\mathbf{x}' = \mathbf{x}_1\frac{du^1(s)}{ds}+\mathbf{x}_2\frac{du^2(s)}{ds},$$

$$\mathbf{x}'' = \mathbf{x}_{11}\left(\frac{du^1(s)}{ds}\right)^2+2\mathbf{x}_{12}\frac{du^1(s)}{ds}\frac{du^2(s)}{ds}+\mathbf{x}_{22}\left(\frac{du^2(s)}{ds}\right)^2+\mathbf{x}_1\frac{d^2u^1(s)}{ds^2}+\mathbf{x}_2\frac{d^2u^2(s)}{ds^2}.$$

Let's assume $\mathbf{x}'\left(u^1(s),u^2(s)\right)=\frac{d\mathbf{x}}{ds}$ and $\mathbf{x}''\left(u^1(s),u^2(s)\right)=\frac{d^2\mathbf{x}}{ds^2}$, since $\mathbf{x}_1$ and $\mathbf{x}_2$ are in the tangent plane i.e., $\mathbf{x}_1,\mathbf{x}_2\perp\boldsymbol{n}$. Now taking inner product with the normal vector $\boldsymbol{n}$, we have

$$\langle\mathbf{x}'',\boldsymbol{n}\rangle = \langle\mathbf{x}_{11},\boldsymbol{n}\rangle\left(\frac{du(s)}{ds}\right)^2+2\langle\mathbf{x}_{12},\boldsymbol{n}\rangle\frac{du^2(s)}{ds}\frac{du^1(s)}{ds}$$
$$+\langle\mathbf{x}_{22},\boldsymbol{n}\rangle\left(\frac{du^2(s)}{ds}\right)^2+\langle\mathbf{x}_1,\boldsymbol{n}\rangle\frac{d^2u^2(s)}{ds^2}+\langle\mathbf{x}_2,\boldsymbol{n}\rangle\frac{d^2u^2(s)}{ds^2}.$$

Since $\mathbf{x}_1$ *and* $\mathbf{x}_2$ *are in the tangent plane. In consequences, the last two terms will vanish and* $\mathbf{x}_{12} = \mathbf{x}_{21}$*, thus we get*

$$\left\langle \mathbf{x}'', \boldsymbol{n} \right\rangle = \left\langle \mathbf{x}_{11}, \boldsymbol{n} \right\rangle \left(\frac{du^1(s)}{ds} \right)^2 + 2 \left\langle \mathbf{x}_{12}, \boldsymbol{n} \right\rangle \frac{du^1(s)}{ds} \frac{du^1(s)}{ds} + \left\langle \mathbf{x}_{22}, \boldsymbol{n} \right\rangle \left(\frac{du^2(s)}{ds} \right)^2.$$

Using coefficients of the second fundamental form §2.1.2,

$$\left\langle \mathbf{x}'', \boldsymbol{n} \right\rangle = b_{11} \left(\frac{du^1(s)}{ds} \right)^2 + 2b_{12} \frac{du^1(s)}{ds} \frac{du^2(s)}{ds} + b_{22} \left(\frac{du^2(s)}{ds} \right)^2,$$

$$\left\langle \mathbf{x}'', \boldsymbol{n} \right\rangle = \frac{\begin{pmatrix} du^1 & du^2 \end{pmatrix} \begin{pmatrix} b_{11} & b_{12} \\ b_{21} & b_{22} \end{pmatrix} \begin{pmatrix} du^1 \\ du^2 \end{pmatrix}}{ds^2}. \tag{2.33}$$

Since $\mathbf{x}''$ *has two components, the coefficients with* $\mathbf{x}_i$ *for* $i = 1,2$ *are in the tangent plane and* $\mathbf{x}_{ij}$ *for* $i, j = 1,2$ *are in the normal plane. The tangential component brings the geodesic curvature and the normal component provide the normal curvature. The dot product of equation (2.33) results a useful relation of Frenet-Serret formula [44],* $\mathbf{x}'' = \kappa \boldsymbol{n}$*, where* $\boldsymbol{n}$ *is the normal vector to the curve.*

$$\left\langle \kappa \boldsymbol{n}, \boldsymbol{n} \right\rangle = \frac{a^T \mathscr{B} a}{ds^2}.$$

As we know for the curvature

$$\kappa \left\langle \boldsymbol{n}, \boldsymbol{n} \right\rangle = \kappa \|\boldsymbol{n}\| \|\boldsymbol{n}\| cos(\theta) = \kappa_n,$$

we have the following relation,

$$\kappa_n = \frac{a^T \mathscr{B} a}{ds^2}. \tag{2.34}$$

Through the natural parametrization of a vector curve,

$$ds = \|d\mathbf{x}(s)\| = \sqrt{\langle d\mathbf{x}, d\mathbf{x} \rangle},$$

$$ds = \sqrt{\langle \mathbf{x}_1 du^1 + \mathbf{x}_2 du^2, \mathbf{x}_1 du^1 + \mathbf{x}_2 du^2 \rangle}.$$

In the simplified form

$$ds = \sqrt{\left\langle \mathbf{x}_1, \mathbf{x}_1 \right\rangle (du^1)^2 + 2 \left\langle \mathbf{x}_1, \mathbf{x}_2 \right\rangle du^1 du^2 + \left\langle \mathbf{x}_2, \mathbf{x}_2 \right\rangle (du^2)^2}.$$

$$ds^2 = a^T \mathscr{G} a, \tag{2.35}$$

combining (2.34) and (2.35), we have the relation for the mean curvature

$$\kappa_n = \frac{a^T \mathscr{B} a}{a^T \mathscr{G} a}. \tag{2.36}$$

Where "a" is the matrix of the parametrized vectors and "a^T" is the respective transpose matrix. Goldman [44] articulated the following form of the mean curvature:

$$H = trace\left((\mathscr{B})\left(\mathscr{G}^{-1}\right)\right).$$

Where $\mathscr{G}$ and $\mathscr{B}$ are coefficients matrices of first and second fundamental forms §2.1.1–2.1.2, respectively.

Lemma 2.2.3. *(Weingarten equation)*
Let Γ is a surface with a parametric representation $\mathbf{x}(u^1,u^2)$ and the first and second fundamental forms coefficients are given by g_{ik} and b_{ik} for $i,k = 1,2$. Then the partial derivative of the surface normal vector $\boldsymbol{n}_k$ satisfies the following relation,

$$\boldsymbol{n}_k = -b_k^i \mathbf{x}_i \quad for \quad i,k = 1,2. \tag{2.37}$$

Proof. Since $\boldsymbol{n}$ is unit normal

$$\boldsymbol{n} = \frac{\mathbf{x}_1 \times \mathbf{x}_2}{\|\mathbf{x}_1 \times \mathbf{x}_2\|}.$$

We have for the normal vectors,

$$\boldsymbol{n} \cdot \boldsymbol{n} = 1,$$

after taking derivatives it can be perceived that $\boldsymbol{n}_j$ is in the tangent plane. Thus we can express them in the linear combination of vectors $\mathbf{x}_1$ and $\mathbf{x}_2$.

$$\boldsymbol{n}_k = -C_k^i \mathbf{x}_i \quad \text{for} \quad i,k = 1,2. \tag{2.38}$$

It follows from (2.37) and definition of the second fundamental form coefficients §2.1.2

$$C_k^i = \delta_n^i C_k^n = g^{ij} g_{jn} C_k^n = g^{ij} \mathbf{x}_j \cdot \mathbf{x}_n C_k^n \quad \text{for} \quad k = 1,2,$$

where n is a dummy index. Thus

$$C_k^i = g^{ij} \mathbf{x}_j \cdot \mathbf{x}_n C_k^n = g^{ij} \mathbf{x}_j \cdot \boldsymbol{n}_k = -g^{ij} b_{jk} = -b_k^i \quad \text{for} \quad k = 1,2. \tag{2.39}$$

Using (2.39) in (2.38) concludes that the partial derivative of surface normal vector satisfy Weingarten equation. □

2.3 Transport equation on surface

Definition 4. *(Surface velocity function)*
Let us introduce a time parameter t, to define the evolution of surface. Consider $\Gamma(t)$ as the surface at any time t with coordinate $\mathbf{x}$, and assume for $d = 3$,

$$\boldsymbol{v} : \Gamma(t) \times [0,\infty) \to \mathbb{R}^d$$

is a vector field on $\Gamma(t)$. The surface evolution equation can be obtained as:

$$\frac{\partial \mathbf{x}}{\partial t} = \boldsymbol{v}, \quad t > 0. \tag{2.40}$$

Where $\boldsymbol{v}(\mathbf{x}(u^1,u^2,t))$ specifies the velocity of the each point of surface known as velocity function. In general, $\boldsymbol{v}$ may depends on space variable and the mean curvature. For simplicity, the surface evolution is transformed along the normal direction assuming that all forces are acting in the normal direction.

The transport of the physical particle in the system model through a generic transport (advection/convection-diffusion) equation. The derivation is established from the assumptions of Stone [116], Xu and Zhao [139] and Huang et al. [51]. The transport equation on a simple domain Ω is relatively easy to drive as compare to those on the surface Γ. In case of surface few extra terms appear due to evolution of the surface. The scalar conservation law for surface partial differential equation discussed here is also based on assumptions of Dziuk et al. [31].

Consider an interfacial element $\Gamma(t)$ which lies on $\mathbb{R}^d$. The surface is continuously deforming and embedded in $\mathbb{R}^{d+1}$. For $d = 2$ assuming that the interface is deforming with the motion of surface active agent which remains on the interfacial element. Let ρ the mass per unit area, from conservation laws we have

$$\frac{d}{dt}\left(\int_{\Gamma(t)} \rho dA\right) = 0, \tag{2.41}$$

where dA is the surface area. Let $\mathbf{x}_0$ is a fixed point of the initial configuration and define two new independent parameters (u^1,u^2). The parametric form of the interfacial element at any time t is given by $\Gamma(t) := \{\mathbf{x}(u^1,u^2,t)|(x^1,x^2) \in A_0\}$. For a fixed domain like A_0 the interfacial element is $\Gamma(0) := \{\mathbf{x}_0(u^1,u^2)|(u^1,u^2) \in A_0\}$. This derivation of transport equation is based on the Lagrangian approach with the evolution in time interface. Assume that the deforming interface is sufficiently smooth and differentiable so that the unit tangent vectors and corresponding normal vectors $\boldsymbol{n}$ can independently be expressed as:

$$\tau_1 = \frac{\frac{\partial \mathbf{x}}{\partial u^1}}{\left|\frac{\partial \mathbf{x}}{\partial u^1}\right|}, \; \tau_2 = \frac{\frac{\partial \mathbf{x}}{\partial u^2}}{\left|\frac{\partial \mathbf{x}}{\partial u^2}\right|} \quad \text{and} \quad \boldsymbol{n} = \frac{\tau_1 \times \tau_2}{|\tau_1 \times \tau_2|} = \frac{\frac{\partial \mathbf{x}}{\partial u^1} \times \frac{\partial \mathbf{x}}{\partial u^2}}{\left|\frac{\partial \mathbf{x}}{\partial u^1} \times \frac{\partial \mathbf{x}}{\partial u^2}\right|}. \tag{2.42}$$

Since the interface immersed in a three dimensional space and moves with velocity $\boldsymbol{v}$, from definition (4) $\boldsymbol{v}$ is defined by

$$\frac{\partial \mathbf{x}(u^1,u^2,t)}{\partial t} = \boldsymbol{v}(\mathbf{x}(u^1,u^2,t)). \tag{2.43}$$

An initial fixed point of reference is $\mathbf{x}(u^1,u^2,0) = \mathbf{x}_0(u^1,u^2)$.

Lemma 2.3.1. *The material time derivative of the surface element is defined as*

$$\frac{d}{dt}\left|\frac{\partial \mathbf{x}}{\partial u^1}\times\frac{\partial \mathbf{x}}{\partial u^2}\right| = (\nabla_\Gamma\cdot\boldsymbol{v})\left|\frac{\partial \mathbf{x}}{\partial u^1}\times\frac{\partial \mathbf{x}}{\partial u^2}\right|. \tag{2.44}$$

Where the surface divergent is defined in [116] by the following relation

$$\nabla_\Gamma\cdot\boldsymbol{v} = \left(\frac{\partial \boldsymbol{v}}{\partial \tau_1}\cdot b_2 + \frac{\partial \boldsymbol{v}}{\partial \tau_2}\cdot b_1\right)\frac{\left|\frac{\partial \mathbf{x}}{\partial u^1}\right|\left|\frac{\partial \mathbf{x}}{\partial u^2}\right|}{\left|\frac{\partial \mathbf{x}}{\partial u^1}\times\frac{\partial \mathbf{x}}{\partial u^2}\right|}. \tag{2.45}$$

Where b_1 and b_2 are the tangential unit vectors normal to τ_1 and τ_2, given by

$$b_1 = \boldsymbol{n}\times\tau_1 \quad \textit{and} \quad b_2 = \tau_2\times\boldsymbol{n}. \tag{2.46}$$

Proof. Let $\boldsymbol{a}$, $\boldsymbol{b}$, $\boldsymbol{c}$ and $\boldsymbol{d}$ denote the time dependent vectors in $\mathbb{R}^d$, for $d=3$ we can use the following identity

$$(\boldsymbol{a}\times\boldsymbol{b})\cdot(\boldsymbol{c}\times\boldsymbol{d}) = (\boldsymbol{a}\cdot\boldsymbol{c})(\boldsymbol{b}\cdot\boldsymbol{d}) - (\boldsymbol{a}\cdot\boldsymbol{d})(\boldsymbol{b}\cdot\boldsymbol{c}). \tag{2.47}$$

Since $\boldsymbol{n}\cdot\boldsymbol{n} = 1$, we have

$$\frac{d\boldsymbol{n}}{dt}\cdot\boldsymbol{n} = 0. \tag{2.48}$$

As we know that the cross product of two vectors is a new vector perpendicular to the plane

$$\frac{\partial \mathbf{x}}{\partial u^1}\times\frac{\partial \mathbf{x}}{\partial u^2} = \left|\frac{\partial \mathbf{x}}{\partial u^1}\times\frac{\partial \mathbf{x}}{\partial u^2}\right|\boldsymbol{n}. \tag{2.49}$$

Using Eqs. (2.48)– (2.49) and definition 4 with chain rule in the LHS of Eq. (2.44), we get

$$\begin{aligned}
\frac{d}{dt}\left|\frac{\partial \mathbf{x}}{\partial u^1}\times\frac{\partial \mathbf{x}}{\partial u^2}\right| &= \boldsymbol{n}\cdot\frac{d}{dt}\left(\frac{\partial \mathbf{x}}{\partial u^1}\times\frac{\partial \mathbf{x}}{\partial u^2}\right)\\
&= \boldsymbol{n}\cdot\left(\frac{\partial^2 \mathbf{x}}{\partial\, t\partial u^1}\times\frac{\partial \mathbf{x}}{\partial u^2}\right) + \boldsymbol{n}\cdot\left(\frac{\partial \mathbf{x}}{\partial u^1}\times\frac{\partial^2 \mathbf{x}}{\partial\, t\partial u^2}\right)\\
&= \boldsymbol{n}\cdot\left(\frac{\partial \boldsymbol{v}}{\partial u^1}\times\frac{\partial \mathbf{x}}{\partial u^2}\right) + \boldsymbol{n}\cdot\left(\frac{\partial \mathbf{x}}{\partial u^1}\times\frac{\partial \boldsymbol{v}}{\partial u^2}\right).
\end{aligned}$$

In the above expression, using definition of the normal vector (2.42) and applying the identity (2.47), we get the following equation

$$\frac{d}{dt}\left|\frac{\partial \mathbf{x}}{\partial u^1}\times\frac{\partial \mathbf{x}}{\partial u^2}\right| = \frac{B}{\left|\frac{\partial \mathbf{x}}{\partial u^1}\times\frac{\partial \mathbf{x}}{\partial u^2}\right|}, \tag{2.50}$$

where

$$B = \left[\frac{\partial \mathbf{x}}{\partial u^1}\cdot\frac{\partial \boldsymbol{v}}{\partial u^2}\left(\frac{\partial \mathbf{x}}{\partial u^2}\right)^2 + \frac{\partial \mathbf{x}}{\partial u^2}\cdot\frac{\partial \boldsymbol{v}}{\partial u^2}\left(\frac{\partial \mathbf{x}}{\partial u^1}\right)^2 - \frac{\partial \mathbf{x}}{\partial u^1}\cdot\frac{\partial \mathbf{x}}{\partial u^2}\left(\frac{\partial \mathbf{x}}{\partial u^2}\cdot\frac{\partial \boldsymbol{v}}{\partial u^2} + \frac{\partial \mathbf{x}}{\partial u^1}\cdot\frac{\partial \boldsymbol{v}}{\partial u^2}\right)\right] \tag{2.51}$$

From definition of the surface divergence (2.45), we get

$$\frac{d}{dt}\left|\frac{\partial \mathbf{x}}{\partial u^1}\times\frac{\partial \mathbf{x}}{\partial u^2}\right| = \nabla_\Gamma\cdot\boldsymbol{v}, \tag{2.52}$$

from equations (2.50) and (2.52), we have

$$\nabla_\Gamma\cdot\boldsymbol{v} = \frac{B}{\left|\frac{\partial \mathbf{x}}{\partial u^1}\times\frac{\partial \mathbf{x}}{\partial u^2}\right|^2}. \tag{2.53}$$

□

Remark 1. *In this remark we will show this definition of the surface divergence defined through equations (2.51) and (2.53) is consistent with the following equation.*

$$\nabla_\Gamma\cdot\boldsymbol{v} = (I-\boldsymbol{n}\otimes\boldsymbol{n})\,\nabla\cdot\boldsymbol{v} \tag{2.54}$$

For simplification in notations we assume $\mathbf{z}^k$ *as the parameter for surface with* $z^1 = u^1$ *and* $z^2 = u^2$ *and the third parameter* z^3 *is used for the parameter along the normal direction. As we used* $\mathbf{x}^i$ *as the Cartesian coordinates and* $\mathbf{e}_i$ *the corresponding unit vectors for* $i = 1,2$*. The position and velocity vectors are defined by*

$$\mathbf{x} = u^i\mathbf{e}_i, \quad \boldsymbol{v} = v^i\mathbf{e}_i \quad \textit{for } i = 1,2.$$

We used the co-variants and contra-variants notation to deal with the non-Cartesian coordinates.

$$g_k = \frac{\partial u^i}{\partial z^k}\mathbf{e}_i, \quad i = 1,2 \textit{ and } k = 1,2,3. \tag{2.55}$$

$$g^k = \frac{\partial z^k}{\partial u^i}\mathbf{e}_i, \quad i = 1,2 \textit{ and } k = 1,2,3. \tag{2.56}$$

The orthogonality property is given as:

$$g^i\cdot g_j = \delta^i_j, \tag{2.57}$$

here δ_i^j is the Kronecker delta function, comparing with (2.42), we have

$$\left.\begin{aligned} \tau_1 = \frac{g_1}{|g_1|}, \quad \tau_2 = \frac{g_2}{|g_2|}, \\ b_1 = \frac{g^2}{|g^2|}, \quad b_2 = \frac{g^1}{|g^1|}, \\ \boldsymbol{n} = \frac{g_3}{|g_3|} = \frac{g^3}{|g^3|}. \end{aligned}\right\}$$

Using equations (2.55)–(2.56) and keeping in view that $\mathbf{e}_i$ are constant unit vectors, we have

$$\nabla \cdot \boldsymbol{v} = \frac{\partial (\mathbf{e}_i \cdot \boldsymbol{v})}{\partial u^i} = \frac{\partial (\mathbf{e}_i \cdot \boldsymbol{v})}{\partial z^k} \cdot \frac{\partial z^k}{\partial u^i} = \mathbf{e}_i \cdot \frac{\partial \boldsymbol{v}}{\partial z^k} \cdot \frac{\partial z^k}{\partial u^i} = g^k \cdot \frac{\partial \boldsymbol{v}}{\partial z^k}. \tag{2.58}$$

Similarly, we have

$$\nabla \boldsymbol{v} = \frac{\partial \boldsymbol{v}}{\partial u^i} \mathbf{e}_i = \frac{\partial \boldsymbol{v}}{\partial z^k} g^k, \tag{2.59}$$

using the orthogonality property (2.57) and expanding the dummy index $k = 1,2,3$, we have

$$\begin{aligned} \boldsymbol{n} \cdot \nabla \boldsymbol{v} \cdot \boldsymbol{n} = \boldsymbol{n} \cdot \frac{\partial \boldsymbol{v}}{\partial z^k} g^k \cdot \boldsymbol{n} &= \boldsymbol{n} \cdot \frac{\partial \boldsymbol{v}}{\partial z^3} \left| g^3 \right|, \\ &= g^3 \cdot \frac{\partial \boldsymbol{v}}{\partial z^3}. \end{aligned} \tag{2.60}$$

Using equations (2.55), (2.56), (2.58) and (2.60) in equation (2.54) will give

$$\begin{aligned} \nabla \cdot \boldsymbol{v} - \boldsymbol{n} \cdot \nabla \boldsymbol{v} \cdot \boldsymbol{n} &= g^1 \cdot \frac{\partial \boldsymbol{v}}{\partial z^1} + g^2 \cdot \frac{\partial \boldsymbol{v}}{\partial z^2} + g^3 \cdot \frac{\partial \boldsymbol{v}}{\partial z^3} - g^3 \cdot \frac{\partial \boldsymbol{v}}{\partial z^3} \\ &= \left| g^1 \right| |g_1| b_2 \cdot \frac{\partial \boldsymbol{v}}{\partial \tau_1} + \left| g^2 \right| |g_2| b_1 \cdot \frac{\partial \boldsymbol{v}}{\partial \tau_2}. \end{aligned} \tag{2.61}$$

From equation (2.57), we have

$$|g^1||g_1| \tau_1 \cdot b_2 = |g^1||g_1| \tau_2 \cdot b_1 = 1. \tag{2.62}$$

Using relations from (2.46), we have

$$\tau_1 \cdot b_2 = \tau_1 \cdot (\tau_2 \times \boldsymbol{n}) = \boldsymbol{n} \cdot (\tau_1 \times \tau_2) = |\tau_1 \times \tau_2|,$$

and

$$\tau_2 \cdot b_2 = \tau_2 \cdot (\tau_1 \times \boldsymbol{n}) = \boldsymbol{n} \cdot (\tau_1 \times \tau_2) = |\tau_1 \times \tau_2|.$$

Through these calculations, we have

$$|g^1||g_1| = |g^2||g_2| = \frac{1}{|\tau_1 \times \tau_2|} = \left| \frac{\partial \mathbf{x}}{\partial u^1} \right| \left| \frac{\partial \mathbf{x}}{\partial u^2} \right| \Big/ \left| \frac{\partial \mathbf{x}}{\partial u^1} \times \frac{\partial \mathbf{x}}{\partial u^2} \right|. \tag{2.63}$$

Plugging the value from equation (2.63) into equation (2.61) and keeping in view the equation (2.54), we have

$$\nabla\cdot\boldsymbol{v}-\boldsymbol{n}\cdot\nabla\boldsymbol{v}\cdot\boldsymbol{n}=\left[\left|\frac{\partial\mathbf{x}}{\partial u^1}\right|\left|\frac{\partial\mathbf{x}}{\partial u^2}\right|/\left|\frac{\partial\mathbf{x}}{\partial u^1}\times\frac{\partial\mathbf{x}}{\partial u^2}\right|\right]\left(b_2\cdot\frac{\partial\boldsymbol{v}}{\partial\tau_1}+b_1\cdot\frac{\partial\boldsymbol{v}}{\partial\tau_2}\right) \quad (2.64)$$

which concludes that these two representations are consistent.

Lemma 2.3.2. *Now to derive the transport equation for ρ on surface using the law of conservation of mass (2.41), we have*

$$\begin{aligned}0 &= \frac{d}{dt}\left(\int_{\Gamma(t)}\rho dA\right),\\ &= \frac{d}{dt}\int_{\Gamma(0)}\rho(\mathbf{x},t))\left|\frac{\partial\mathbf{x}}{\partial u^1}\times\frac{\partial\mathbf{x}}{\partial u^2}\right|du^1du^2,\\ &= \int_{\Gamma(0)}\frac{D}{Dt}\rho\left|\frac{\partial\mathbf{x}}{\partial u^1}\times\frac{\partial\mathbf{x}}{\partial u^2}\right|du^1du^2+\int_{\Gamma(0)}\rho\frac{d}{dt}\left|\frac{\partial\mathbf{x}}{\partial u^1}\times\frac{\partial\mathbf{x}}{\partial u^2}\right|du^1du^2,\end{aligned}$$

where the usual material derivative is defined as:

$$\frac{D}{Dt}\rho=\frac{\partial\rho}{\partial t}+\boldsymbol{v}\cdot\nabla\rho.$$

Using equation (2.52) and after taking common, we obtain

$$\begin{aligned}0 &= \int_{\Gamma(0)}\left(\frac{\partial\rho}{\partial t}+\boldsymbol{v}\cdot\nabla\rho+\rho(\nabla_\Gamma\cdot\boldsymbol{v})\right)\left|\frac{\partial\mathbf{x}}{\partial u^1}\times\frac{\partial\mathbf{x}}{\partial u^2}\right|du^1du^2,\\ &= \int_{\Gamma(t)}\left(\frac{\partial\rho}{\partial t}+\boldsymbol{v}\cdot\nabla\rho+\rho(\nabla_\Gamma\cdot\boldsymbol{v})\right)dA.\end{aligned}$$

Since $\Gamma(t)$ is arbitrary, we obtain the the following equation

$$\frac{\partial\rho}{\partial t}+\boldsymbol{v}\cdot\nabla\rho+\rho(\nabla_\Gamma\cdot\boldsymbol{v}) = 0.$$

Using the fact that the surface active agent transport only along the interface, so the tangential component vanishes as we know that the gradient and the normal vector are in the same direction, the above equation becomes

$$\frac{\partial\rho}{\partial t}+\boldsymbol{v}\cdot\nabla_\Gamma\rho+\rho(\nabla_\Gamma\cdot\boldsymbol{v}) = 0.$$

This lemma leads to an important result known as Leibniz formula for partial differential equation on surfaces.

Lemma 2.3.3. *(Leibniz formula)*
Let us assume that ρ is a function define on the surface Γ such that the following equation holds

$$\frac{d}{dt}\int_\Gamma\rho=\int_\Gamma(\partial_t^\bullet\rho+\rho\nabla_\Gamma\cdot\boldsymbol{v}), \quad (2.65)$$

where $\partial_t^\bullet \rho$ is given by

$$\partial_t^\bullet \rho = \frac{\partial \rho}{\partial t} + \boldsymbol{v} \cdot \nabla \rho. \tag{2.66}$$

As $\boldsymbol{v} = V\boldsymbol{n} + \boldsymbol{v}_S$ are the normal and tangential components of velocity, then we have

$$\nabla_\Gamma \cdot \boldsymbol{v} = \nabla_\Gamma \cdot (V\boldsymbol{n} + \boldsymbol{v}_S) = \nabla_\Gamma V \cdot \boldsymbol{n} + V \nabla_\Gamma \cdot \boldsymbol{n} + \nabla_\Gamma \cdot \boldsymbol{v}_S. \tag{2.67}$$

Since $\nabla_\Gamma V \in T\Gamma$ which is perpendicular to $\boldsymbol{n}$, thus the first term will vanish. As we know the mean curvature is define by $H = -\nabla_\Gamma \cdot \boldsymbol{n}$, (see remark 2.5). Thus we get the following form of equation (2.67)

$$\rho \nabla_\Gamma \cdot \boldsymbol{v} = -VH\rho + \rho \nabla_\Gamma \cdot (\boldsymbol{v}_S). \tag{2.68}$$

For the second term $\boldsymbol{v} \cdot \nabla_\Gamma \rho$, we have

$$\boldsymbol{v} \cdot \nabla_\Gamma \rho = (V\boldsymbol{n} + \boldsymbol{v}_S) \nabla_\Gamma \rho = V\boldsymbol{n} \cdot \nabla \rho + \boldsymbol{v}_S \nabla \rho = V \frac{\partial \rho}{\partial \boldsymbol{n}} + \boldsymbol{v}_S \cdot \nabla \rho \tag{2.69}$$

in case velocity is only along the normal direction, then we have $v = V\boldsymbol{n}$ (i.e., $\boldsymbol{v}_S = 0$), thus finally we get $\boldsymbol{v} \cdot \nabla_\Gamma \rho = V \frac{\partial \rho}{\partial \boldsymbol{n}}$

$$\frac{d}{dt} \int_\Gamma \rho = \int_\Gamma \left(\frac{\partial \rho}{\partial t} + V \frac{\partial \rho}{\partial \boldsymbol{n}} - \rho VH + \nabla_\Gamma \cdot (\rho \boldsymbol{v}_S) \right). \tag{2.70}$$

A similar proof of Leibniz formula on parametric surface can be found in [26].

Theorem 2.3.4. *Let us assume that $\Gamma \subset \mathbb{R}^{d+1}$ is a hypersurface (e.g., see definition 1) with smooth boundary $\partial\Gamma$, for $\rho \in C^1$ from [29], we have the following relation*

$$\int_\Gamma \nabla_\Gamma \rho dA = \int_\Gamma \rho H \boldsymbol{n} dA + \int_{\partial\Gamma} \rho \boldsymbol{n}_{\partial\Gamma} dA. \tag{2.71}$$

Where H is the mean curvature and $\boldsymbol{n}_{\partial\Gamma}$ is the co-normal vector which is normal to the boundary $\partial\Gamma$ and tangent to the surface Γ.

Proof. Let ρ is a function and U_ε is the neighborhood of Γ, then

$$\bar{\rho} = \rho(a(x)) \quad x \in U,$$

applying chain rule

$$\frac{\partial \bar{\rho}}{\partial \mathbf{x}^j} = \sum_{j,k=1}^{d+1} \mathscr{D}_k \rho(a(x)) \frac{\partial a_k}{\partial \mathbf{x}^j}(x). \tag{2.72}$$

Here $\mathscr{D}_k$ is the tangential derivative along surface, from equation (2.13) for $k = 1, \ldots, d$, we get

$$\mathscr{D}_k = d\rho_p(\boldsymbol{\xi}) = \frac{d}{d\tau}\Big|_{\tau=\tau_o} \rho(\gamma(\tau)). \tag{2.73}$$

From (2.15) the manifold representation reads as:

$$\mathscr{D}_k = \mathscr{G}\,\langle \nabla_\Gamma \rho(p), \boldsymbol{\xi} \rangle \quad \forall\, \boldsymbol{\xi} \in T\Gamma\,. \tag{2.74}$$

Using (2.72), we have

$$\frac{\partial a^k}{\partial \mathbf{x}^j} = \frac{\partial}{\partial \mathbf{x}^j}\left(\mathbf{x}^k - d(x)\boldsymbol{n}_k(x)\right) = \delta^k_j - \boldsymbol{n}_j(x)\boldsymbol{n}_k(x) - d(x)H_{jk}(x)\,.$$

Here δ^k_j is the Kronecker delta function and H is the mean curvature, which can be calculated through derivatives of the normal. The matrix $(a^{kj})_{j,k=1,\ldots,d+1}$ maps any vector along the tangent vector. We have

$$\nabla\bar{\rho}(x) = (I - d(x)H(x))\nabla_\Gamma \rho(a(x)).$$

We obtain that $\nabla\bar{\rho} = \nabla_\Gamma\rho(x) \quad \text{for} \quad x \in \Gamma$, using Gauss theorem for $\bar{\rho}$ on the ε-neighborhood of U_ε, we have

$$\int_{U_\varepsilon} \nabla\bar{\rho}\,dx = \int_{\partial U_\varepsilon} \bar{\rho}\,\boldsymbol{n}_{\partial U_\varepsilon}(x)\,dA(x)\,.$$

We have that $\partial U_\varepsilon = \Gamma(\varepsilon) \cup \Gamma(-\varepsilon) \cup \mathscr{M}(\varepsilon)$, where $\mathscr{M} = \{x + r\boldsymbol{n}_{\Gamma(x)} \Big| s \in \partial\Gamma, r \in [-\varepsilon, \varepsilon]\}$

$$\begin{aligned}\frac{1}{2\varepsilon}\int_{U_\varepsilon}(I - d(x)H(x))\nabla\rho(a(x))dx &= \frac{1}{2\varepsilon}\int_{\Gamma(\varepsilon)}\bar{\rho}(x)\boldsymbol{n}_\Gamma(x)dA(x)\\ -\frac{1}{2\varepsilon}\int_{\Gamma(-\varepsilon)}\bar{\rho}(x)\boldsymbol{n}_\Gamma(x)dA(x) &+ \frac{1}{2\varepsilon}\int_{\mathscr{M}(\varepsilon)}\bar{\rho}(x)\boldsymbol{n}_{\partial\Gamma}(x)dA(x)\,.\end{aligned} \tag{2.75}$$

Where $\boldsymbol{n}$ is the normal vector, $\boldsymbol{n}_{\partial\Gamma}$ is the co-normal to Γ and both do not depend on ε. Taking limit $\varepsilon \to 0$ on both sides of the equation, we have for the left hand side as:

$$\lim_{\varepsilon\to 0}\frac{1}{2\varepsilon}\int_{U_\varepsilon}(I - d(x)H(x))\nabla\rho(a(x))dx = \int_\Gamma \nabla_\Gamma\rho(x)dA(x)\,. \tag{2.76}$$

The limits of the right hand side is given by

$$\frac{1}{2\varepsilon}\int_{\Gamma_\varepsilon}\bar{\rho}(x)\boldsymbol{n}_\Gamma(x)dA(x) = \int_\Gamma \rho(x)H(x)\boldsymbol{n}_\Gamma(x)dA(x)\,. \tag{2.77}$$

For the last term on the right hand side of the (2.75) as the integrand does not dependent on ε, we have

$$\lim_{\varepsilon\to 0}\frac{1}{2\varepsilon}\int_{\mathscr{M}\varepsilon}\bar{\rho}(x)\boldsymbol{n}_{\partial\Gamma}(x)dA(x) = \int_{\partial\Gamma}\rho(x)\boldsymbol{n}_{\partial\Gamma}(x)dA(x)\,. \tag{2.78}$$

Here equations (2.76), (2.77) and (2.78) conclude the required result. □

Remark 2. *In case of compact hypersurface Γ does not have a boundary i.e., $\partial\Gamma = \emptyset$, the last term in the right hand side of (2.71) vanishes and we get*

$$\int_\Gamma \nabla_\Gamma \rho dA = \int_\Gamma \rho H \boldsymbol{n} dA. \tag{2.79}$$

Theorem 2.3.5. *(Green formula on surface)*

$$\int_\Gamma \nabla_\Gamma f \cdot \nabla_\Gamma g dA = -\int_\Gamma f \Delta_\Gamma g dA + \int_{\partial\Gamma} f \nabla_\Gamma g \cdot \boldsymbol{n}_{\partial\Gamma} dA\,. \tag{2.80}$$

Proof. Using theorem (2.3.4) and the summation convention that are appearing for double indices, we have

$$\begin{aligned}\int_\Gamma \nabla_\Gamma f \cdot \nabla_\Gamma g dA &= \int_\Gamma \mathscr{D}_i f \mathscr{D}_i g dA = \int_\Gamma \mathscr{D}_i (f \mathscr{D}_i g)\, dA - \int_\Gamma f \mathscr{D}_i \mathscr{D}_i g \\ &= \int_\Gamma f \mathscr{D}_i g H \boldsymbol{n}_i dA + \int_{\partial\Gamma} f \mathscr{D}_i g \boldsymbol{n}_{\partial\Gamma_i} dA - \int_\Gamma f \Delta_\Gamma g dA\,.\end{aligned}$$

Since $\mathscr{D}_i g$ is in the tangent plane, thus $\mathscr{D}_i g \cdot \boldsymbol{n} = 0$. Where $\mathscr{D}_i$ is tangential derivative given in (2.73) and (2.74). This formula is known as Green's formula on the surfaces and concludes the result. □

2.4 Level set method

We used the level set methods to describe the evolution of hypersurfaces. The theory of level set methods utilize the view point of Eulerian partial differential equation, instead of looking at boundary motion from a natural geometric Lagrangian perspective. In consequences, a powerful numerical technique for analyzing and computing interfaces emerged that can undergo through topological changes. In the current work the level set methods involve to solve a problem of interest on surface Γ. The interface is represented by the zero-contour of the level set function ϕ (see figure 2.3). The technical strength of the methods come from its ability to manipulate and change in topology of the interface. Using an implicit representation of a surface, its evolution can be written in terms of partial differential equation which will be used to define interface of the surface. The evolution of the interface of Γ can be captured through level set methods. Assume that $\phi(\mathbf{x},t)$ represents the level set function and the interface separating one region from another. We assumed that $\Gamma(t) \subset \Omega$ is a compact smooth connected and oriented hypersurface in $\mathbb{R}^d$, for $d = 3$ there exists a smooth level set function

$$\phi(\mathbf{x},t) = \begin{cases} < 0 & \text{if } \mathbf{x} \text{ is inside } \Gamma(t)\,, \\ = 0 & \text{if } \mathbf{x} \in \Gamma(t)\,, \\ > 0 & \text{if } \mathbf{x} \text{ is outside } \Gamma(t)\,. \end{cases} \tag{2.81}$$

The gradient of the implicit function ϕ is defined by

$$\nabla\phi = \left(\frac{\partial\phi}{\partial x^1}, \frac{\partial\phi}{\partial x^2}, \frac{\partial\phi}{\partial x^3}\right)^T.$$

The gradient of ϕ is perpendicular to the isocontours of ϕ and point in the direction of an increasing ϕ. The zero-level set or zero-isocontour $(\phi = 0)$ shown in figure 2.3 is the interface of the surface. For any point in the zero-level set or zero-isocontour of ϕ, the $\nabla\phi$ evaluate a vector that points in the same direction as the local unit normal vector $\boldsymbol{n}$ to the interface.

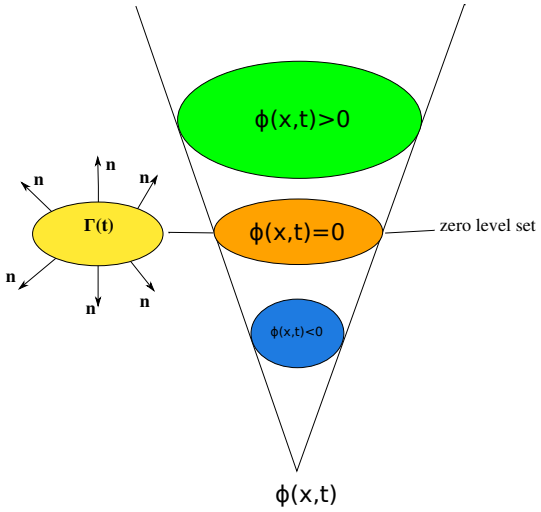

Figure 2.3: Isocontours of level set function $\phi(\mathbf{x},t)$ where $\Gamma(t)$ is represented as zero-level set function. The left picture is showing that each point on interface is moving along the normal direction.

Definition 5. *(Normal vector)*
A vector $\boldsymbol{n} \in \mathbb{R}^{d+1}$ is called a unit normal vector at the point $p \in \Gamma$ if $\boldsymbol{n} \perp T_p\Gamma$. The normal vector through the gradient of the level set function ϕ is defined by:

$$\boldsymbol{n} = \frac{\nabla\phi}{|\nabla\phi|}. \tag{2.82}$$

Since the implicit level set representation of the interface embeds the interface in a domain of one dimension higher [91]. It can be helpful to get more information through this representation. For instance, instead of defining the unit normal $\boldsymbol{n}$ (2.82) for points on interface, we can extend it from the ε-neighborhood of the interface Γ to the whole domain Ω.

2.4.1 Formulation of level set

The surface evolution in level set technique is formulated as a partial differential equation. A discretization is required to numerically simulate the continuous

problem. To achieve a numerically stable solution the stabilization methods have to be incorporated into the discretization. The level set technique is uses to address the problem of moving closed surface denoted by Γ in the normal direction with a velocity function $\boldsymbol{v}$. The function $\boldsymbol{v}$ varies its values depending on local or global measurements. Here $\boldsymbol{v}$ is the velocity of the interface which can be determined through forces acting on the surface such as chemo-attractive/chemo-repulsive forces, bending of surface due to curvature and etc. The value of $\boldsymbol{v}$ can be described analytically as well. The function ϕ is used to capture the motion of the interface in time. In this scenario, the motion of the interface is not in its tangential direction, for simplicity the tangential motions can be ignored. The surface evolution should be independent of the parametrization as well. Let us assume $\Gamma(t)$ is the family of closed surfaces, where t represents the time variable and $\mathbf{x}(x^1,x^2,x^3)$ parametrized the surface. Keeping in view the notion of moving interface for any physical quantity ρ on an evolving surface can be formulated in the following equations

$$\frac{\partial \rho}{\partial t} + \boldsymbol{v} \cdot \nabla_\Gamma \rho + \rho(\nabla_\Gamma \cdot \boldsymbol{v}) \quad = \quad 0 \quad \text{where} \quad \rho \in \Gamma(t)\,,$$

with an initial condition

$$\rho(\mathbf{x}, t=0) = \rho_0 \quad \text{where} \quad \rho_0 \in \Gamma\,, \tag{2.83}$$

here $\boldsymbol{v}$ is the velocity of a point on the surface in the normal direction $\boldsymbol{n}$ which is defined at each point on the surface Γ. Instead of choosing a parametrization of the surface Γ, the idea behind the level set formulation is to define the interface implicitly as the zero-level of ϕ :

$$\Gamma(t) = \{\mathbf{x} | \phi(\mathbf{x}, t) = 0\}\,. \tag{2.84}$$

The equation of motion derive after looking at a particle on the front with path $\mathbf{x}(t)$. The level set function $\phi(\mathbf{x},t)$ is vanishing at the position of the particle as the particle is part of the surface Γ itself:

$$\phi(\mathbf{x}(t), t) = 0. \tag{2.85}$$

Using chain rule in equation (2.85) the derivative in time of ϕ is:

$$\frac{\partial \phi}{\partial t} + \nabla \phi(\mathbf{x}(t), t) \cdot \frac{d\mathbf{x}}{dt} = 0\,, \tag{2.86}$$

where $\boldsymbol{v} = \frac{d\mathbf{x}}{dt}$ is the velocity of the interface define in equation (2.40). Thus we get the following relation for the level set:

$$\frac{\partial \phi}{\partial t} + \boldsymbol{v} \cdot \nabla \phi = 0\,. \tag{2.87}$$

The equation (2.87) does not explicitly evolve the parametrized surface but describes the change of a function in time. This is defined in full space dimension

through initial conditions (2.83). The level set equation not only evolves the interface Γ in time, which is assumed to be the zero-level set of ϕ but in general evolves all isocontours define by ϕ. Hence the function ϕ has to be extended from the embedded surface to the entire space. The numerical construction together with finite element method will be part of further discussion. The mathematical formulation construction of scheme and numerical implementation of the level set method including the historical note on origin of the technique can be found in [108–111]. The potential applications of the level set methods include, computational geometry, fluid mechanics, combustion, grid generation, computer vision, seismic analysis, material science and manufacturing of semi-conductor, an extensive literature review can be found in [1, 18, 20, 23, 91, 108, 111, 128].

Level set as sign distance function

The implicit surface is described through a function $\phi(\mathbf{x},t)$ on the surface. The function is vanishing at the interface known as zero-level set $\phi(\mathbf{x},t=0)$. The values at all other points are arbitrary because they have no influence on the position of the surface. In order to achieve the best computational stability, we take care that $\phi(\mathbf{x},t)$ is not too shallow or steep. In results, $\phi(\mathbf{x},t)$ can be chosen as the sign distance function. To allow a partition the sign is set to positive on one side of the interface and negative on the other side, the surface is assumed to be closed and orientable.

$$\phi(\mathbf{x},t) = \begin{cases} -dist(\mathbf{x},\Gamma), & \text{if } \mathbf{x} \text{ is inside } \Gamma(t)\,, \\ = 0, & \text{if } \mathbf{x} \in \Gamma(t), \\ dist(\mathbf{x},\Gamma), & \text{if } \mathbf{x} \text{ is outside } \Gamma(t)\,. \end{cases} \tag{2.88}$$

Level set method is handy during surface evolution, the topological changes occur because of the evolution are not necessary to model explicitly. It is obvious that the topological change of surface Γ does not imply the topological change of $\phi(\mathbf{x},t)$. We can describe several geometrical entities in terms of level set function, such as velocity vector V defined in remark (8), the normal vector $\boldsymbol{n}$ definition (5) and the mean curvature H §(2.5). The numerical state of the art for computing the distance function includes, the sweeping methods [104], the fast marching technique [110] and the closest point method [71].

Remark 3. *If $\phi = d(\mathbf{x},t)$ is signed distance function from $\mathbf{x}$ to Γ to be defined as*

$$d(\mathbf{x}) = \begin{cases} -\inf\limits_{\mathbf{y}\in\Gamma} |\mathbf{x}-\mathbf{y}| & \textit{if } \mathbf{x} \textit{ is inside } \Gamma\,, \\ = 0 & \textit{if } \mathbf{x} \in \Gamma\,, \\ \inf\limits_{\mathbf{y}\in\Gamma} |\mathbf{x}-\mathbf{y}| & \textit{if } \mathbf{x} \textit{ is outside } \Gamma\,, \end{cases} \tag{2.89}$$

then without loss of generality, we have

$$|\nabla\phi(\mathbf{x},t)| = 1\,. \tag{2.90}$$

Remark 4. *The result (2.90) can be satisfied in a general sense. Since it is not true for all points which are equidistant from at least two points on the interface. Although, mathematical equations that are true in a general sense can be used in numerical calculations as long as they do not destroy the numerical method entirely when they fail.*

Example: A signed distance function is an implicit function such that $|\phi(\mathbf{x})| = d(\mathbf{x})$ for all $\mathbf{x}$. Let us take an example of a signed distance function as a representation of the unit sphere is a 2-*D* surface embedded in $\mathbb{R}^3$

$$\phi(\mathbf{x}) = \|\mathbf{x}\|^2 - 1 = 0, \tag{2.91}$$

where $\|\mathbf{x}\|^2 = (x^1)^2 + (x^2)^2 + (x^3)^2$. Note that property (2.90) is true for the signed distance functions (2.91). It is well understood that the signed distance function enables us to find the closest point $a(x)$ on Γ to a point $\mathbf{x} \in \mathbb{R}^{d+1}$ by taking

$$a(x) = x - \phi(\mathbf{x},t)\boldsymbol{n}. \tag{2.92}$$

Now we define an ε-neighborhood around the interface to make the closest point mapping unique. Let U_ε be an open set in $\mathbb{R}^{d+1}$ is a volumetric neighborhood around the interface, can be defined like

$$U_\varepsilon = \{\mathbf{x} \in \mathbb{R}^{n+1} \text{ such that } |\phi(\mathbf{x})| < \varepsilon\}, \tag{2.93}$$

where ε is small enough to guarantee uniqueness of the mapping

$$a(x) : U_\varepsilon \to \Gamma.$$

This mapping allows to introduce a global coordinate system around the interface of the surface Γ as for every point $x \in U_\varepsilon$ we can assign the Fermi like coordinates $\phi(\mathbf{x})$ and $a(x)$. Here, we have to notice that $\boldsymbol{n}(\mathbf{x}) = \boldsymbol{n}(a(\mathbf{x}))$ for every point $x \in U_\varepsilon$. Also, any function h defined on Γ can be extended to U_ε as $h_e(x) = h(a(x))$.

Corollary 1. *If $\phi = d(\mathbf{x})$ then $\boldsymbol{n} = \nabla\phi$ is an orthogonal vector w.r.t. surface Γ.*

Let us assume $\mathbf{x} : U_\varepsilon \subset \mathbb{R}^d \to \Gamma$ is a coordinate patch for $d = 2$, define (u^1, u^2) as the coordinate variables of U_ε, with definition of the level set function, we have

$$\phi(\mathbf{x}(u^1,u^2)) = 0, \quad \forall (u^1,u^2) \in U_\varepsilon\,. \tag{2.94}$$

Differentiating with respect to u^1 and u^2, we have

$$\begin{aligned}\phi_{u^1} &= \langle \nabla\phi, \mathbf{x}_1 \rangle = 0\,,\\ \phi_{u^2} &= \langle \nabla\phi, \mathbf{x}_2 \rangle = 0\,.\end{aligned}$$

Since $\mathbf{x}$ is a coordinate patch $\mathbf{x}_1$ and $\mathbf{x}_2$ are two linearly independent vectors in $T\Gamma$. As $\nabla\phi$ is perpendicular to both of them, this implies that it must be in parallel to the normal. Finally normalizing and choosing a conventional sign we obtain the

inward and outward normal vectors to an evolving surface $\Gamma(t)$ expressed through the level set function:

$$\boldsymbol{n}_{\text{in}} = -\nabla\phi/|\nabla\phi|\,, \tag{2.95}$$

$$\boldsymbol{n}_{\text{out}} = \nabla\phi/|\nabla\phi|\,. \tag{2.96}$$

Such that $|\nabla\phi| \neq 0$ and a projection $\mathscr{P}_\Gamma$ on $\Gamma(t)$ using equation (2.82), we have

$$\mathscr{P}_\Gamma = I - \boldsymbol{n}\otimes\boldsymbol{n} = I - \frac{\nabla\phi}{|\nabla\phi|}\otimes\frac{\nabla\phi}{|\nabla\phi|}\,. \tag{2.97}$$

$\mathscr{P}_\Gamma$ is the projection onto the tangent space $T\Gamma$. In case if $\phi(\cdot)$ is chosen as a signed distance function (2.88) then $|\nabla\phi| = 1$.

2.5 Differential operators and level set approach

The purpose of this section is to derive the most basic results for differential operators on surface. These results can be useful in finite element discretization of the surface defined PDEs. The timely use of these remarks will reduce the mathematical complexity. In case of such a physical model using these constraints the numerical implementation of the system will be similar to those of the Euclidean domain.

The gradient and divergence for a scalar function ξ on Ω and a tangential vector field $\boldsymbol{\xi}$ on Γ, can be obtained from eqs.(2.23) and (2.30) as:

$$\nabla_\Gamma\xi = \mathscr{P}_\Gamma\nabla\xi = (I-\boldsymbol{n}\otimes\boldsymbol{n})\nabla\xi \tag{2.98}$$

$$\nabla_\Gamma\cdot\boldsymbol{\xi} = \mathscr{P}_\Gamma\nabla\xi = (I-\boldsymbol{n}\otimes\boldsymbol{n})\nabla\cdot\boldsymbol{\xi} \tag{2.99}$$

As ∇_Γ and $\nabla_\Gamma(\cdot)$ denote the intrinsic gradient and divergence operators, respectively. These operators are well-defined for any scalar and vector quantities on surface Γ.

Consider $\nabla_\Gamma\xi$ denotes a vector within $\mathbb{R}^d$ that is tangent to the surface Γ, in case it is constant along the normal. The gradient along the surface give results of usual gradient operator, stated in the following remark.

Remark 5. *Consider function $\xi \in \mathbb{R}^d$ for $d = 3$, it is constant along directions normal to the surface. Then we have at the surface,*

$$\nabla_\Gamma\xi = \nabla\xi \tag{2.100}$$

Proof. Since

$$\nabla_\Gamma\xi = \mathscr{P}_\Gamma\nabla\xi\,. \tag{2.101}$$

Where the projection operator on Γ is define as:

$$\mathscr{P}_\Gamma = (I-\boldsymbol{n}\otimes\boldsymbol{n})\,. \tag{2.102}$$

Plugging equation (2.102) in equation (2.101), we have

$$\nabla_\Gamma \xi \;=\; (I - \boldsymbol{n}\otimes\boldsymbol{n})\nabla\xi\,. \tag{2.103}$$

Using the following formula for dyadic tensor product

$$\boldsymbol{a}\otimes\boldsymbol{b}\cdot\boldsymbol{c} \;=\; \boldsymbol{a}\cdot\langle\boldsymbol{b},\boldsymbol{c}\rangle \tag{2.104}$$

we get

$$\nabla_\Gamma \xi \;=\; \nabla\xi - \boldsymbol{n}\otimes\boldsymbol{n}\cdot\nabla\xi, \tag{2.105}$$

$$\;=\; \nabla\xi - \boldsymbol{n}\cdot\langle\boldsymbol{n},\nabla\xi\rangle\,. \tag{2.106}$$

Where $\langle\boldsymbol{n},\nabla\xi\rangle = \nabla_{\boldsymbol{n}}\xi$. Since ξ is constant along the direction normal to Γ, this term will vanishes, consequently we have

$$\nabla_\Gamma \xi \;=\; \nabla\xi \tag{2.107}$$

This statement elaborate that a function that is constant in the normal direction $\boldsymbol{n}$ only varies along the surface Γ. □

In the following result we will show under certain conditions, the divergence defined on surface get characteristics of the usual divergence.

Remark 6. *For any vector field $\boldsymbol{\xi}\in\mathbb{R}^d$ that is tangent at surface Γ, and also tangent at all surfaces displaced by a fixed distance from Γ. In other words, all surfaces defined as distance functions in terms of level sets, then the divergence defined at the surface*

$$\nabla_\Gamma\cdot\boldsymbol{\xi} \;=\; \nabla\cdot\boldsymbol{\xi} \tag{2.108}$$

Proof. Since the projection operator to the surface is define by

$$\mathscr{P}_\Gamma \;=\; I - \boldsymbol{n}\otimes\boldsymbol{n}$$

$$\nabla_\Gamma\cdot\boldsymbol{\xi} \;=\; (I - \boldsymbol{n}\otimes\boldsymbol{n})\nabla\cdot\boldsymbol{\xi} \tag{2.109}$$

Using the associative property of dot product [51]

$$\nabla_\Gamma\cdot\boldsymbol{\xi} \;=\; \nabla\cdot\boldsymbol{\xi} - \boldsymbol{n}\otimes(\nabla\cdot\boldsymbol{\xi}\cdot\boldsymbol{n})\,, \tag{2.110}$$

since $\boldsymbol{\xi}\in T\Gamma$ then $\boldsymbol{\xi}\cdot\boldsymbol{n} = 0$, we have

$$\nabla_\Gamma\cdot\boldsymbol{\xi} \;=\; \nabla\cdot\boldsymbol{\xi} \tag{2.111}$$

This condition says that a flux directed along the surface Γ can only spread outward in the surface directions. □

Now we can define the Laplace-Beltrami operator (2.31) on $\Gamma(t)$. In general, it is the gradient of divergence of a function on the surface, given by

$$\Delta_\Gamma \xi = \nabla_\Gamma \cdot \nabla_\Gamma \xi = \nabla \cdot \mathscr{P}_\Gamma \nabla \xi \,. \tag{2.112}$$

Remark 7. *Assuming that the surface divergence of a vector equal to the regular divergence of its projection $\mathscr{P}_\Gamma$ to the curve, then the Laplace-Beltrami operator can be defined as:*

$$\nabla_\Gamma \cdot \nabla_\Gamma \xi = \nabla \cdot \nabla_\Gamma \xi = \nabla \cdot \mathscr{P}_\Gamma \nabla \xi \,. \tag{2.113}$$

Proof. The surface gradient operator is defined by:

$$\begin{aligned} \nabla_\Gamma (\bullet) &= (I - \boldsymbol{n} \otimes \boldsymbol{n}) \cdot \nabla (\bullet) \,, \\ &= \nabla (\bullet) - (\boldsymbol{n} \otimes \boldsymbol{n}) \cdot \nabla (\bullet) \,, \\ &= \nabla (\bullet) - (\boldsymbol{n} \cdot \nabla (\bullet)) \cdot \boldsymbol{n} \,. \end{aligned}$$

Now to show the following quantity

$$\nabla_\Gamma \cdot \nabla_\Gamma \xi = \nabla \cdot \nabla_\Gamma \xi \,,$$

we have

$$\begin{aligned} \nabla_\Gamma \cdot \zeta &= (\nabla - (\boldsymbol{n} \cdot \nabla) \cdot \boldsymbol{n}) \, \zeta \,, \\ &= \nabla \zeta - (\boldsymbol{n} \cdot \nabla) \, \boldsymbol{n} \cdot \zeta \,, \\ &= \nabla \zeta - \boldsymbol{n} \cdot \nabla (\boldsymbol{n} \cdot \zeta) \,. \end{aligned}$$

Let's assume $\zeta = \nabla_\Gamma \xi$ and substituting this value, we have

$$\nabla_\Gamma \cdot \nabla_\Gamma \xi = \nabla \cdot (\nabla_\Gamma \xi) - \boldsymbol{n} \cdot \nabla (\boldsymbol{n} \cdot \nabla_\Gamma \xi) \,,$$

here taking the second term $\boldsymbol{n} \cdot \nabla (\boldsymbol{n} \cdot \nabla_\Gamma \xi)$, we have

$$\begin{aligned} (\boldsymbol{n} \cdot \nabla_\Gamma \xi) &= \boldsymbol{n} \cdot (\nabla \xi - (\boldsymbol{n} \cdot \nabla \xi) \, \boldsymbol{n}) \,, \\ &= \boldsymbol{n} \cdot \nabla \xi - (\boldsymbol{n} \cdot \nabla \xi) \, \boldsymbol{n} \cdot \boldsymbol{n} \,, \\ &= \boldsymbol{n} \cdot \nabla \xi - (\boldsymbol{n} \cdot \nabla \xi) \,, \\ &= 0. \end{aligned}$$

Thus we get

$$\nabla_\Gamma \cdot \nabla_\Gamma \xi = \nabla \cdot \nabla_\Gamma \xi \,.$$

This concludes the remark. □

The velocity vector $V(\mathbf{x},t)$ can be calculated using the level set function $\phi(\mathbf{x}(t),t)$, in case the level set function is given, we can easily obtain the velocity vector using the following remark.

Remark 8. *To calculate the velocity $V(\mathbf{x},t)$ vector in terms of the level set function $\phi(\mathbf{x}(t),t)$ let us consider a curve c*

$$c = \phi(\mathbf{x}(t),t) \quad \forall \quad \mathbf{x}(t) \in \Gamma(t)\,. \tag{2.114}$$

Differentiating w.r.t. time variable $'t'$ and using definition (4)

$$0 = \phi_t(\mathbf{x}(t),t) + \mathbf{x}_t(t)\cdot\nabla\phi(\mathbf{x}(t),t)\,,$$

$$0 = \phi_t(\mathbf{x}(t),t) + \boldsymbol{v}\cdot\nabla\phi(\mathbf{x}(t),t)\,.$$

Since surface is moving in the normal direction, $\boldsymbol{v} = V\boldsymbol{n}$ and using definition of the outward normal (2.95), we get

$$0 = \phi_t(\mathbf{x}(t),t) + V\cdot\frac{\nabla\phi(\mathbf{x}(t),t)\cdot\nabla\phi(\mathbf{x}(t),t)}{|\nabla\phi(\mathbf{x}(t),t)|}\,.$$

The velocity in terms of the level set function $\phi(\mathbf{x},t)$ as:

$$V(\mathbf{x},t) = -\frac{\phi_t(\mathbf{x},t)}{|\nabla\phi(\mathbf{x},t)|}\,. \tag{2.115}$$

The remarks 8 and 9 use level set formulation for simplification of PDEs defined on surface. These results are useful in mathematical formulation and FEM discretization of PDEs on evolving-in-time surface.

Remark 9. *Let ϕ is the level set function $\phi \in C^2$ and $\boldsymbol{n}$ is the normal vector, then the time derivative is define as*

$$\partial_t|\nabla\phi(\mathbf{x})| = \boldsymbol{n}\cdot\nabla\phi_t\,. \tag{2.116}$$

Proof. Using definition (5) with straight forward chain rule, provide proof. □

Mean curvature

We already study curvature related formulae in §2.2.2, here we introduce once again the notion of mean curvature, which is used for FEM level set formulation of geometric PDEs. It is used in modeling and computation of the curvature dependent interface motion governed through surface defined PDEs. Several versions of curvature formula for implicit curves and surfaces are presented by Goldman [44]. Another variant of the formula discuss in remark 10 to calculate mean curvature, can be found in a book by Gilbarg & Trudinger [43, Chap. 14].

Remark 10. *Assume that we have a level set function $\phi \in C^2(\Omega)$ as $\phi : \mathbb{R}^d \to \mathbb{R}$ and define a curve $\mathbf{x} : \mathbb{R} \to \mathbb{R}^d$. The codomain of the curve for $d = 2$ is $\Gamma_r = \{(x^1, x^2) | \phi(x^1, x^2) = r\}$ where r is a constant. The curve $\mathbf{x}$ is parametrization by arc length so, we have $\|\mathbf{x}'\| = 1$. Then the curvature of the curve is define as*

$$H = -\nabla_\Gamma \cdot \boldsymbol{n} = -\nabla_\Gamma \cdot \frac{\nabla \phi}{|\nabla \phi|}. \tag{2.117}$$

Where $\phi = \phi(\mathbf{x}(s))$.

Proof. Let the curve is parametrized by its arc length

$$\|\mathbf{x}'(s)\| = 1.$$

The derivative w.r.t. arc length s gives,

$$0 = \frac{d}{ds} \left\langle \mathbf{x}'(s), \mathbf{x}'(s) \right\rangle,$$

$$0 = 2 \left\langle \mathbf{x}''(s), \mathbf{x}'(s) \right\rangle.$$

As $\mathbf{x}'(s)$ and $\mathbf{x}''(s)$ are perpendicular to each others. Assuming $\mathbf{x}''(s) \neq 0$, thus the unit normal vector locally defined to the fields $\mathbf{x}$ is $\boldsymbol{n} := \frac{\mathbf{x}''(s)}{\|\mathbf{x}''(s)\|}$. Since $\mathbf{x}$ parametrizes the level set function ϕ and $\nabla \phi$ is orthonormal to its level set function, then the normal vector reads as follows:

$$\boldsymbol{n} = \pm \frac{\mathbf{x}''(s)}{\|\mathbf{x}''(s)\|}.$$

Since the curvature is defined using Frenet-Serret formula [44]

$$H = \left\|\mathbf{x}''(s)\right\| = \left|\left\langle \mathbf{x}''(s), \boldsymbol{n} \right\rangle\right| = \left| \frac{d}{ds} \left\langle \mathbf{x}'(s), \boldsymbol{n} \right\rangle - \left\langle \mathbf{x}'(s), \frac{d}{ds} \boldsymbol{n} \right\rangle \right|,$$

as $\mathbf{x}'(s)$ is in the tangent plane, consequently,

$$H = \left\langle \mathbf{x}'(s), \frac{d}{ds} \boldsymbol{n} \right\rangle.$$

Since $\|\boldsymbol{n}(s)\| = 1$, it follows like $\mathbf{x}'(s)$ as $\left\langle \boldsymbol{n}, \frac{d}{ds} \boldsymbol{n} \right\rangle = 0$, thus $\frac{d}{ds} \boldsymbol{n}$ is in the tangent plane and multiple of $\mathbf{x}'(s)$. So,

$$\left\| \frac{d}{ds} \boldsymbol{n} \right\| = \left| \left\langle \mathbf{x}'(s), \frac{d}{ds} \boldsymbol{n} \right\rangle \right|,$$

thus

$$H = \left\| \frac{d}{ds} \boldsymbol{n}(s) \right\| = \left\| \frac{d}{ds} \frac{\nabla \phi}{|\nabla \phi|} \right\|. \tag{2.118}$$

Now to prove that $|\nabla_\Gamma \cdot \boldsymbol{n}| = \left\| \frac{d}{ds} \boldsymbol{n}(s) \right\|$.

Let us define an arbitrary vector field with differential $\mathscr{D}_i\boldsymbol{\xi}$.

$$\boldsymbol{\xi} : \mathbb{R}^d \times \mathbb{R}^d.$$

Let $(b^i)_{i=1}^d$ are orthonormal basis of $\mathbb{R}^d$, then

$$\nabla_\Gamma \cdot \boldsymbol{\xi} = \sum_{i=1}^{d} \langle \mathscr{D}_i \boldsymbol{\xi}(b_i), b_i \rangle \,. \tag{2.119}$$

Since divergence is defined as the trace of the Levi Civita connection, we have

$$\left\| \frac{d}{ds}\boldsymbol{n} \right\| = \left\langle \mathbf{x}'(s), \frac{d}{ds}\boldsymbol{n} \right\rangle = \left\langle \mathbf{x}'(s), \mathscr{D}_i \boldsymbol{n}(s) \right\rangle + \left\langle \boldsymbol{n}(s), \mathscr{D}_i \boldsymbol{n}(s) \right\rangle ,$$

here $\mathscr{D}_i\boldsymbol{n}$ is the differential of $\boldsymbol{n}$, in the above equation the first term is zero as vector and its differential are perpendicular to each others, which holds due to extension of the level set function.

$$\left\| \frac{d}{ds}\boldsymbol{n} \right\| = \nabla_\Gamma \cdot \boldsymbol{n} \tag{2.120}$$

Using (2.118) and (2.120), conclude the results. □

Remark 11. *The surface* Γ *is called minimal at a point* $\mathbf{x}_0$ *iff* $H(\mathbf{x}_0) = 0,\ \forall\, \mathbf{x}_0 \in \Omega$.

2.5.1 Surface PDEs formulae

The aim of this section to derive few useful formulae for computation of the geometric partial differential equations. These are the Coarea formula 2.5.1, the Eulerian integration by parts 2.5.2 and implicit surface Leibniz formula 2.5.3. These formulae can be found in Dziuk and Elliott [27, 29].

Theorem 2.5.1. *This theorem is known as Coarea formula.*
Let for each $t \in [0,T]$, $\phi(t,\cdot) : \bar{\Omega} \to \mathbb{R}$ *be Lipschitz continuous and assume that for each* $r \in (inf_\Omega \phi, sup_\Omega \phi)$ *the level set* $\Gamma_r = \{\mathbf{x} | \phi(\mathbf{x},\cdot) = r\}$ *is a smooth* d*-dimensional hypersurface in* $\mathbb{R}^{d+1}$. *Suppose* $\rho : \bar{\Omega} \to \mathbb{R}$ *is continuous and integrable. Then*

$$\int_{inf_\Omega}^{sup_\Omega} \left(\int_{\Gamma_r} \rho \right) dr = \int_\Omega \rho |\nabla \phi|. \tag{2.121}$$

Proof. Let $\Omega \subset \mathbb{R}^d$ for $d = 3$, ϕ is a level set function and $\phi \in C^2(\Omega)$ such that $|\nabla\phi| \neq 0$ and $\Gamma_r = \{x | \phi(\mathbf{x},\cdot) = r\}$. Since $|\nabla\phi| \neq 0$ this implies that there exists $\nabla_d \phi \neq 0$. Without loss of generality, we can assume for the case $d = 1,2,3$ and $\nabla_3 \phi := \phi_{x^3} \neq 0$.

$$\phi(x^1, x^2, x^3) = r,$$

$$\phi_{x^1} dx^1 + \phi_{x^2} dx^2 + \phi_{x^3} dx^3 = 0\,, \tag{2.122}$$

with the condition $\phi(\mathbf{x},t)=0$, from equation (2.122), we have

$$dx^3 = -\frac{\phi_{x^1}}{\phi_{x^3}}dx^1 - \frac{\phi_{x^2}}{\phi_{x^3}}dx^2 . \tag{2.123}$$

Since the metric is

$$(dx^1)^2+(dx^2)^2+(dx^3)^2 = Volume . \tag{2.124}$$

Using (2.123) in (2.124), we have

$$\left(1+\frac{\phi_{x^1}^2}{\phi_{x^3}^2}\right)(dx^1)^2 - 2\frac{\phi_{x^1}^2\phi_{x^2}^2}{\phi_{x^3}^2}(dx^1)^2(dx^2)^2 + \left(1+\frac{\phi_{x^2}^2}{\phi_{x^3}^2}\right)(dx^2)^2 = Vol . \tag{2.125}$$

Where the coefficients of the first fundamental form are $g_{11}=1+\frac{\phi_{x^1}^2}{\phi_{x^3}^2}$, $g_{12}=g_{21}=-\frac{\phi_{x^1}^2\phi_{x^2}^2}{\phi_{x^3}^2}$ and $g_{22}=1+\frac{\phi_{x^2}^2}{\phi_{x^3}^2}$. Since the determinant of the first fundamental form is defined by, $det(\mathscr{G}) := g = g_{11}g_{22}-g_{12}^2$, thus

$$g = \left(1+\frac{\phi_{x^1}^2}{\phi_{x^3}^2}\right)\left(1+\frac{\phi_{x^2}^2}{\phi_{x^3}^2}\right) - \left(\frac{\phi_{x^1}^2\phi_{x^2}^2}{\phi_{x^3}^2}\right)^2 . \tag{2.126}$$

$$g = 1+\frac{\phi_{x^1}^2}{\phi_{x^3}^2}+\frac{\phi_{x^2}^2}{\phi_{x^3}^2} = \frac{|\nabla\phi|}{|\phi_{x^3}|} = |\Gamma_r| . \tag{2.127}$$

Since $|\nabla\phi\cdot\mathbf{e}_3| = |\phi_{x^3}|dx^3$

$$\int_{\inf_\Omega}^{\sup_\Omega}\left(\int_{\Gamma_r}\rho\right)dr = \int_\Omega \rho\frac{|\nabla\phi|}{|\phi_{x^3}|}|\phi_{x^3}|dx^1dx^2dx^3 = \int_\Omega \rho|\nabla\phi|d\mathbf{x}. \tag{2.128}$$

$$\int_{\inf_\Omega}^{\sup_\Omega}\left(\int_{\Gamma_r}\rho\right)dr = \int_\Omega \rho|\nabla\phi|d\mathbf{x}. \tag{2.129}$$

This concludes proof of the Coarea formula on hypersurface. For more general proof and discussion on coarea formula, we kindly refer to Nicolaescu [82]. □

Lemma 2.5.2. *(Eulerian integration by parts)*
Assume that the following quantities exist. For a scalar function ρ and a vector field Q we have

$$\int_\Omega \nabla_{\Gamma(t)}\rho|\nabla\phi| = -\int_\Omega \rho H\boldsymbol{n}|\nabla\phi| + \int_{\partial\Omega}\rho(\boldsymbol{n}_{\partial\Omega}-\boldsymbol{n}\cdot\boldsymbol{n}_{\partial\Omega}\boldsymbol{n})|\nabla\phi|, \tag{2.130}$$

$$\int_\Omega \nabla_{\Gamma(t)}\cdot Q|\nabla\phi| = -\int_\Omega HQ\cdot\boldsymbol{n}|\nabla\phi| + \int_{\partial\Omega}Q\cdot(\boldsymbol{n}_{\partial\Omega}-\boldsymbol{n}\cdot\boldsymbol{n}_{\partial\Omega}\boldsymbol{n})|\nabla\phi|, \tag{2.131}$$

$$\begin{aligned}\int_\Omega \nabla_{\Gamma(t)}\cdot Q\rho|\nabla\phi| \quad &+ \quad \int_\Omega Q\cdot\nabla_{\Gamma(t)}\rho|\nabla\phi| = \\ -\int_\Omega Q\cdot\boldsymbol{n}\rho H|\nabla\phi| \quad &+ \quad \int_{\partial\Omega}Q\cdot(\boldsymbol{n}_{\partial\Omega}-\boldsymbol{n}\cdot\boldsymbol{n}_{\partial\Omega}\boldsymbol{n})\rho|\nabla\phi|,\end{aligned} \tag{2.132}$$

where $\boldsymbol{n}_{\partial\Omega}$ is an outward normal to $\partial\Omega$.

Proof. Let us use the Einstein notations $\partial_i = \frac{\partial}{\partial x_i}$ and $\partial_{ij} = \frac{\partial^2}{\partial x_i \partial x_j}$ and derive the desired results, following similar procedure like in [27].
Some basic calculations using chain rules and definition of Hessian matrix, we get

$$\begin{aligned} \partial_i|\nabla\phi| &= \boldsymbol{n}_k\partial_{ik}\phi = (\mathscr{D}^2\phi\boldsymbol{n})_i\,, \\ |\nabla\phi|\partial_j\boldsymbol{n}_k &= \partial_{ik}\phi - \boldsymbol{n}_k(\mathscr{D}^2\phi\boldsymbol{n})_j\,, |\nabla\phi|H = -Tr(\mathscr{D}^2\phi) + \boldsymbol{n}\cdot(\mathscr{D}^2\phi)\boldsymbol{n}\,, \end{aligned}$$

where H is the mean curvature and $\mathscr{D}^2\phi$ is the Hessian matrix of second derivatives defined as:

$$\mathscr{D}^2\phi = \begin{bmatrix} \frac{\partial^2\phi}{\partial x^1\partial x^1} & \frac{\partial^2\phi}{\partial x^1\partial x^2} & \cdots & \frac{\partial^2\phi}{\partial x^1\partial x^d} \\ \frac{\partial^2\phi}{\partial x^2\partial x^1} & \frac{\partial^2\phi}{\partial x^2\partial x^2} & \cdots & \frac{\partial^2\phi}{\partial x^2\partial x^d} \\ \vdots & \vdots & \ddots & \vdots \\ \frac{\partial^2\phi}{\partial x^d\partial x^1} & \frac{\partial^2\phi}{\partial x^d\partial x^2} & \cdots & \frac{\partial^2\phi}{\partial x^d\partial x^d} \end{bmatrix}$$

This matrix describes the local curvature and $Tr(\cdot)$ is the trace of the matrix, here we use the summation convention for repeated indices. From definition of ∇_Γ in equation (2.98), we get the left hand side (LHS) of equation (2.130) as:

$$LHS := \int_\Omega \nabla_{\Gamma(t)}\rho|\nabla\phi| = \int_\Omega |\nabla\phi|(\nabla\rho - \boldsymbol{n}\cdot\nabla\rho\boldsymbol{n})\,.$$

Using the standard integration formula on Ω

$$\begin{aligned} (LHS)_i &= -\int_\Omega \rho\partial_i|\nabla\phi| + \int_\Omega \rho\partial_m(\boldsymbol{n}_i\boldsymbol{n}_m|\nabla\phi|) + \int_\Omega \rho|\nabla\phi|((\boldsymbol{n}_{\partial\Omega})_i - \boldsymbol{n}_i(\boldsymbol{n}\cdot\boldsymbol{n}_{\partial\Omega})), \\ &= I + II + III\,, \end{aligned}$$

and the integration by parts in the II term is given by

$$II = \int_\Omega \rho\left(\boldsymbol{n}_i Tr(\mathscr{D}^2\phi) + (\mathscr{D}^2\phi\boldsymbol{n})_i - \boldsymbol{n}\cdot\mathscr{D}^2\phi\boldsymbol{n}\boldsymbol{n}_i\right).$$

Combining I and II and using formula for the mean curvature, produce the desired results. □

Lemma 2.5.3. *(Implicit surface Leibniz formula)*
Let ρ be an arbitrary level set function defined on Ω such that the following formula exists.

$$\frac{d}{dt}\int_\Omega \rho|\nabla\phi| = \int_\Omega (\partial_t^\bullet\rho + \rho\nabla_{\Gamma(t)}\cdot\boldsymbol{v})|\nabla\phi| - \int_{\partial\Omega}\rho\boldsymbol{v}\cdot\boldsymbol{n}_{\partial\Omega}|\nabla\phi|\,. \qquad (2.133)$$

Proof. On the one hand, we already proved the Leibniz formula in §2.3 for transport equation on the surface and on the other hand, here we show the implicit surface Leibniz formula from Dziuk and Elliott [27, 29]

$$\frac{d}{dt}\int_\Omega \rho|\nabla\phi| = \int_\Omega \rho_t|\nabla\phi| + \rho\partial_t|\nabla\phi|\,, \qquad (2.134)$$

for the second term in the integrand using the results from equation (2.116), we have

$$\partial_t|\nabla\phi| = \boldsymbol{n}\cdot\nabla\phi_t\,, \tag{2.135}$$

plugging (2.135) in (2.134), we get

$$\frac{d}{dt}\int_\Omega \rho|\nabla\phi| = \int_\Omega(\rho_t|\nabla\phi| + \rho\boldsymbol{n}\cdot\nabla\phi_t) = I + II\,. \tag{2.136}$$

From remark 8, we have the following relation for the velocity vector $V(\mathbf{x},t)$:

$$V(\mathbf{x},t) = -\frac{\phi_t(\mathbf{x},t)}{|\nabla\phi(\mathbf{x},t)|}\,. \tag{2.137}$$

Using integration by parts on the second term in RHS of equation (2.136):

$$\begin{aligned} II = \int_\Omega(\rho\boldsymbol{n})\cdot\nabla\phi_t &= -\int_\Omega\nabla\rho\cdot\boldsymbol{n}\phi_t - \int_\Omega\rho\nabla_\Gamma\cdot\boldsymbol{n}\cdot\phi_t - \int_{\partial\Omega}\rho\boldsymbol{n}\cdot\boldsymbol{n}_{\partial\Omega}\phi_t\,,\\ &= III + IV + V\,, \end{aligned} \tag{2.138}$$

using (2.137) we obtain

$$III = -\int_\Omega\nabla\rho\cdot\boldsymbol{n}\phi_t = \int_\Omega\nabla\rho\cdot\boldsymbol{n}\frac{-\phi_t}{|\nabla\phi|}|\nabla\phi| = \int_\Omega\nabla\rho\cdot\boldsymbol{n}V|\nabla\phi|\,, \tag{2.139}$$

from the mean curvature definition and using equation (2.117), we have

$$\begin{aligned} IV = -\int_\Omega\rho\nabla\cdot\boldsymbol{n}\cdot\phi_t &= \int_\Omega\rho\nabla_\Gamma\cdot(-\boldsymbol{n})\cdot\frac{\partial\phi}{\partial\mathbf{x}}\frac{\partial\mathbf{x}}{\partial t} = \int_\Omega\rho\boldsymbol{v}\cdot\boldsymbol{n}H\nabla\phi\,,\\ &= \int_\Omega\rho\boldsymbol{v}\cdot H\frac{\nabla\phi}{|\nabla\phi|}|\nabla\phi| = \int_\Omega\rho\boldsymbol{v}\cdot\boldsymbol{n}H|\nabla\phi|\,. \end{aligned} \tag{2.140}$$

$$\begin{aligned} V = -\int_{\partial\Omega}\rho\boldsymbol{n}\cdot\boldsymbol{n}_{\partial\Omega}\phi_t &= -\int_{\partial\Omega}\rho\boldsymbol{n}\cdot\boldsymbol{n}_{\partial\Omega}\boldsymbol{v}\nabla\phi = -\int_{\partial\Omega}\rho\boldsymbol{n}\cdot\boldsymbol{n}_{\partial\Omega}\boldsymbol{v}\frac{\nabla\phi}{|\nabla\phi|}|\nabla\phi|\,,\\ &= -\int_{\partial\Omega}\rho\boldsymbol{n}\cdot\boldsymbol{n}_{\partial\Omega}\boldsymbol{n}\boldsymbol{v}|\nabla\phi|\,. \end{aligned} \tag{2.141}$$

Using values from equations (2.139)–(2.141) in (2.138), we get

$$\begin{aligned} II = \int_\Omega(\rho\boldsymbol{n})\cdot\nabla\phi_t &= \int_\Omega\nabla\rho\cdot\boldsymbol{n}V|\nabla\phi| + \int_\Omega\rho\boldsymbol{v}\cdot\boldsymbol{n}H|\nabla\phi|\\ &- \int_{\partial\Omega}\rho\boldsymbol{n}\cdot\boldsymbol{n}_{\partial\Omega}\boldsymbol{n}\boldsymbol{v}|\nabla\phi|\,. \end{aligned} \tag{2.142}$$

Now using the Eulerian divergence formula (2.131)

$$\int_\Omega\rho\boldsymbol{v}\cdot\boldsymbol{n}H|\nabla\phi| = \int_\Omega\nabla_\Gamma\cdot(\rho\boldsymbol{v})|\nabla\phi| - \int_{\partial\Omega}\rho\boldsymbol{v}\cdot(\boldsymbol{n}_{\partial\Omega} - \boldsymbol{n}\cdot\boldsymbol{n}_{\partial\Omega}\boldsymbol{n})|\nabla\phi| \tag{2.143}$$

Substituting (2.143) in equation (2.142)

$$\begin{aligned}\int_\Omega (\rho \boldsymbol{n})\cdot\nabla\phi_t &= \int_\Omega \nabla\rho\cdot\boldsymbol{n}V|\nabla\phi| \\ &+ \int_\Omega \nabla_\Gamma(\rho\boldsymbol{v})|\nabla\phi| - \int_{\partial\Omega}\rho\boldsymbol{v}\cdot(\boldsymbol{n}_{\partial\Omega}-\boldsymbol{n}\cdot\boldsymbol{n}_{\partial\Omega}\boldsymbol{n})|\nabla\phi| \\ &- \int_{\partial\Omega}\rho\boldsymbol{v}\boldsymbol{n}\cdot\boldsymbol{n}_{\partial\Omega}\boldsymbol{n}|\nabla\phi|\,. \end{aligned} \tag{2.144}$$

After canceling similar terms from equation (2.144) and equation (2.136), we have

$$\begin{aligned}\frac{d}{dt}\int_\Omega \rho|\nabla\phi| &= \int_\Omega(\rho_t|\nabla\phi| + \int_\Omega \nabla\rho\cdot\boldsymbol{n}V|\nabla\phi| \\ &+ \int_\Omega \nabla_\Gamma(\rho\boldsymbol{v})|\nabla\phi| - \int_{\partial\Omega}\rho\boldsymbol{v}\cdot\boldsymbol{n}_{\partial\Omega}|\nabla\phi|\,. \end{aligned} \tag{2.145}$$

Since we have

$$V\nabla\rho\cdot\boldsymbol{n} + \nabla_{\Gamma(t)}\cdot(\rho\boldsymbol{v}) = \boldsymbol{v}\cdot\nabla\rho + \rho\nabla_{\Gamma(t)}\cdot\boldsymbol{v} \tag{2.146}$$

$$\begin{aligned}\frac{d}{dt}\int_\Omega \rho|\nabla\phi| &= \int_\Omega(\rho_t|\nabla\phi| + \boldsymbol{v}\cdot\nabla\rho + \rho\nabla_{\Gamma(t)}\cdot\boldsymbol{v}\,, \\ &- \int_{\partial\Omega}\rho\boldsymbol{v}\cdot\boldsymbol{n}_{\partial\Omega}|\nabla\phi|\,. \end{aligned} \tag{2.147}$$

hence proved the desired result. □

2.6 Conclusion

We sketched the mathematical formulation including preliminary concepts on surface PDEs. One of the essential parts of this chapter is the derivation of the model equations to understand the peculiar characteristics of the surface PDEs. We will study the model in the subsequent part of the thesis, which usually takes the form of a coupled reaction-diffusion-advection equation posed on a continuously evolving-in-time surface. We formulated the properties of the level set equation and derive the most frequently used physical quantities on the surface using the level set function ϕ. We conclude the chapter after deriving large numbers of formulae on the surface. The notion of weak formulation and finite element method will employ these formulae for surface PDEs. However the approximation of the finite element solution remains unanswered, thus finally we searched for solutions in the Sobolev spaces which are considered to be the natural spaces for solutions of elliptic PDEs [27].

3 Discretization techniques

The aim of this chapter is to introduce discretization of the derived mathematical models. These mathematical formulations reflect a vast variety of well-defined physical models. Here the surface finite element method (FEM) is used for spatial discretization. The FEM discretization is used directly on the surface geometry without further transformation. Furthermore, the level set technique is applied in the surface embedding space. We employ the temporal discretization using variants of θ-schemes. In addition, we introduce the idea of algebraic flux corrected stabilization techniques of FCT and TVD-types. Moreover, we address the surface triangulation and theory on a priori error estimate.

3.1 General model for surface PDEs

3.1.1 Convection-diffusion reaction equations

Mathematically the most generic model for unsteady convection-diffusion/advection chemotaxis like phenomena with chemical reaction can be described by the following system of equations.

$$\frac{\partial c^i}{\partial t} = D_c^i \Delta c^i - \nabla \cdot \left[\chi_c^i \mathbf{w}_c^i(\boldsymbol{c},\boldsymbol{\rho}) c^i\right] + f^i(\boldsymbol{c},\boldsymbol{\rho}) \text{ in } \Omega \times T, \tag{3.1}$$

$$\frac{\partial^* \rho^j}{\partial t} = D_\rho^j \Delta_{\Gamma(t)} \rho^j - \nabla_{\Gamma(t)} \cdot (\chi_\rho^j \mathbf{w}_\rho^j(\boldsymbol{c},\boldsymbol{\rho}) \rho^j) + g^j(\boldsymbol{c},\boldsymbol{\rho}) \text{ on } \Gamma(t) \times T. \tag{3.2}$$

Let's briefly clarify the physical meaning of few terms appearing in the generic model. The concentration of the species $c^i(\mathbf{x},t)$ for $i = 1,\ldots,d$ are defined in the whole domain Ω and are solutions of (3.1). The rate of change term $\frac{\partial c^i}{\partial t}$ is the net gain and loss of concentration per unit time. In contrast to c^i, the unknown functions $\rho^j(\mathbf{x},t)$ for $j = 1,\ldots,n$ live on the surface $\Gamma(t) \subset \Omega$ and are possible solutions of (3.2). The parameter χ is known as chemo-sensitivity if $\chi \geqslant 0$ called chemo-attractant and $\chi < 0$ indicates chemo-repellent, we assume mostly the chemo-attractant case. The terms $-\nabla \cdot \left[\chi_c^i \mathbf{w}_c^i(\boldsymbol{c},\boldsymbol{\rho}) c^i\right]$ and $-\nabla_{\Gamma(t)} \cdot (\chi_\rho^j \mathbf{w}_\rho^j(\boldsymbol{c},\boldsymbol{\rho}) \rho^j)$ are the convective terms provide transport of c and ρ, respectively, with a velocity function $\mathbf{w}$. The functions $f^i(\boldsymbol{c},\boldsymbol{\rho})$ and $g^j(\boldsymbol{c},\boldsymbol{\rho})$ are the reactive kinematic terms.

These terms play a vitally important role in patterns formation. The diffusive terms D_c^j and D_ρ^j indicate the uniform spatial distribution of c and ρ, respectively. Where $\frac{\partial^* \rho^j}{\partial t}$ is a surface material derivative, which takes into account the evolution of $\Gamma(t)$ defined as:

$$\frac{\partial^* \rho}{\partial t} = \partial_t^\bullet \rho + \rho \nabla_{\Gamma(t)} \cdot \boldsymbol{v}, \tag{3.3}$$

here

$$\partial_t^\bullet \rho = \partial_t \rho + \boldsymbol{v} \cdot \nabla \rho \,. \tag{3.4}$$

Where $\boldsymbol{v} \cdot \nabla \rho$ denotes the advective surface material derivative with surface velocity $\boldsymbol{v}$.

The generic structure of mathematical model based on system of equations (3.1)–(3.2) suggest an organized approach to get solution through discretization, simulation and mathematical analysis. A systematic strategy will only facilitate in mathematical development, implementation of scheme and numerical testing of biological phenomena. The general system (3.1)–(3.2) will be helpful in choosing mathematical models of our own choice to find solution of surface defined PDEs. Besides the conceptual simplicity, it provides an easy way to investigate the solution behavior for different cases. One can simply design test cases to find pure-convection, diffusion and/or heat equations on surfaces. We can deduce even more simple cases to investigate the solution profile analytically. The corresponding initial and boundary conditions have to be provided.

3.1.2 Initial and boundary conditions

The system of differential equations (3.1)–(3.2) may describes a wide range of problems depending on initial and/or boundary conditions. This additional information is essential to complete the problem statement. Thus the problem's statement would be able to articulate a realistic problem starting in a finite interval of time within a well-defined domain. The assumed domain and time intervals of a physical model mostly considered keeping in view the restriction of numerical and computational resources. The choice of initial and/or boundary values is also essential to the well-posedness of any problem [59]. The physical domain and initial conditions are vital for observation of structures of biological patterns [74].

Let $\Omega \subset \mathbb{R}^d$ is a bounded domain and $[0,T]$ is a finite time interval. In case of IBVP to treat time derivatives we must define the initial distribution in time.

$$c(\mathbf{x}, t=0) = c_0 \quad \forall\, \mathbf{x} \in \Omega\,, \tag{3.5}$$

$$\rho(\mathbf{x}, t=0) = \rho_0 \quad \forall\, \mathbf{x} \in \Gamma\,. \tag{3.6}$$

Additionally, for the physical terms such a concentration describe on the domain Ω with surrounding medium it is essential to prescribe suitable conditions at the boundary $\partial\Omega$. In case, the values are known we can prescribe the Dirichlet type boundary condition otherwise a given normal flux depending on convective and/or

diffusive parts can be prescribed on the complementary boundary part, known as Neumann boundary condition. In the case for Γ, to treat the close surface Γ for instance, if Γ is empty which implies that the Γ has no boundary then defining a boundary condition makes no sense. This would be the case when Γ is bounding surface of the domain, although we never seriously used this case. Furthermore, if Γ is non-empty then we may impose boundary conditions similar to flat surface as defined in [29]. For the case of homogeneous Dirichlet boundary conditions, we have

$$c(\mathbf{x},t) = 0 \quad \text{on} \quad \partial\Omega, \qquad \rho(\mathbf{x},t) = 0 \quad \text{on} \quad \Gamma, \tag{3.7}$$

similarly, the no-flux condition as:

$$\boldsymbol{n} \cdot \nabla c = 0 \quad \text{on} \quad \partial\Omega, \qquad \boldsymbol{n} \cdot \nabla_{\Gamma} \rho = 0 \quad \text{on} \quad \Gamma. \tag{3.8}$$

3.2 Temporal discretization

The evolving partial differential equations on surfaces are unsteady problems. These PDEs are parabolic or hyperbolic in nature. To achieve an efficient and robust method for such kinds of partial differential equations, we must rely on semi-discrete method like finite difference or method of line. Thus to solve initial boundary value problem (IBVP), we require the basic techniques to solve both spatial and temporal discretization. The temporal discretization are settled through variants of θ-schemes. Other possible time stepping schemes for evolving surface PDEs could be high order Runge-Kutta time discretization by Gottlieb et al. [46] and Dziuk et al. [32] and/or backward difference method by Lubich et al. [66] for parabolic type partial differential equation on surface including error estimates, stability and regularity of the method may be needed as well. For temporal discretization it is essential to choose an appropriate time stepping scheme. Different combination of schemes have their own advantages and disadvantages. For discretization in time the interval $[0,T]$ is defined with the following stepping procedure.

$$0 = t^0 < t^1 \cdots < t^M = T$$

The time steps $k = \Delta t = t^{m+1} - t^m$ in most cases is uniform and can be defined as $t^m = m\Delta t \quad \forall\, m = 0,1,\ldots,M$. The value of the approximate solution with nodal value i at time value t^m is denoted by

$$\rho_i^m = \rho_i(t^m)\,.$$

Because of initial condition (3.6) the value of $\rho_i^0 = \rho(0)$ is supposed to be known value. The time stepping methods initialized the vector in discrete form, e.g., $\rho^0 = \{\rho_i^0\}$ and simultaneously use $\rho^m = \{\rho_i^m\}$ as initial value for the computation of the $\rho^{m+1} = \{\rho_i^{m+1}\}$. This process is fast and requires less computational memory than coupled space and time discretization.

3.2.1 Time stepping methods

The θ-schemes

Let's assume an initial value problem of the following form:

$$\frac{\partial \rho}{\partial t} + f(\rho, t) = 0, \qquad \forall t > 0, \tag{3.9}$$

$$\rho(0) = \rho_0, \tag{3.10}$$

where $\rho(t) \in \mathbb{R}^d$ and the dimension $d = 1, 2, 3$. The $f(\rho, t)$ may contains the discretized spatial derivatives, reactive terms and boundary conditions. Suppose that ρ^m is the value of ρ at time instance $t = t^m$ and $\Delta t = k = t^{m+1} - t^m$, then we can solve for $\rho = \rho^{m+1}$. The simplest time stepping schemes are based on finite difference discretization of time derivative.

$$\rho^{m+1} + \theta k f\left(\rho^{m+1}, t^{m+1}\right) = \rho^m - (1-\theta) k f(\rho^m, t^m), \tag{3.11}$$

here θ is taken in the interval $[0, 1]$ is called an implicitness parameter. The explicit time-stepping schemes, can be obtained for $\theta = 0$ in (3.11) which has been commonly applied to the steady-state problems. The proposed method can produce instability in the solution profile and may requires a very small time step to provide a robust and efficient numerical solution. The explicit scheme is as follows:

$$\rho^{m+1} + k f(\rho^m, t^m) = \rho^m.$$

The implementation and parallelization of explicit schemes is much easier, and has low cost per time steps. A very small time steps is required for stability of the solution profile, mostly in the case where velocity or the mesh size are varying strongly [100]. In the choice of time-stepping methods, implicit schemes (for $\theta = 1$ in equation (3.11)) are most preferable. The implicit methods have become more feasible because of linear and nonlinear solvers. This category of schemes frequently use either simple first order backward-Euler scheme or more preferably the second order Crank-Nicholson (CN). These two methods are included as part of the one-step θ-schemes as given below

$$\rho^{m+1} + k f\left(\rho^{m+1}, t^{m+1}\right) = \rho^m.$$

Backward Euler method is only first order accurate but it is strongly A-stable, which implies that the numerical solution is bounded. The backward Euler method is used for the present study of the mathematical model.

From equation (3.11) the Crank-Nicholson (CN) method reads as:

$$\rho^{m+1} + \frac{k}{2} f\left(\rho^{m+1}, t^{m+1}\right) = \rho^m - \frac{k}{2} f(\rho^m, t^m).$$

This scheme is a second order accurate sometimes suffers from numerical instabilities as well. CN is not strongly A-stable it possesses weak damping properties.

The implicit schemes are stable over a wide range of time steps sometimes they are unconditionally stable. They constitute excellent iterative solvers for steady-state problem. The implementation and parallelization are challenging, these types of schemes have a very high cost per time step. It is insufficiently accurate for truly transient problems at large Δt and convergence of linear solvers may deteriorates as time step increases.

Fractional θ-Schemes

The fractional-θ-scheme divide the time step into the following consecutive sub steps thus introducing new variable $\widehat{\theta} = \alpha\theta k = \beta\breve{\theta}k$.

$$\rho^{m+\theta} + \widehat{\theta} f\left(\rho^{m+\theta}, t^{m+\theta}\right) = \rho^{m} - \beta\theta k f\left(\rho^{m}, t^{m}\right),$$

$$\rho^{m+\theta} + \widehat{\theta} f\left(\rho^{m+1-\theta}, t^{m+1-\theta}\right) = \rho^{m+\theta} - \beta\breve{\theta} k f\left(\rho^{m}, t^{m}\right),$$

$$\rho^{m+1} + \widehat{\theta} f\left(\rho^{m+1}, t^{m+1}\right) = \rho^{m+1-\theta} - \beta\breve{\theta} k f\left(\rho^{m+1-\theta}, t^{m+1-\theta}\right).$$

Choosing the value of θ in the following manners.
$\theta = 1 - \frac{1}{\sqrt{2}}$ and $\breve{\theta} = 1 - 2\theta$ with $\alpha = \frac{1-2\theta}{1-\theta}$ and $\beta = 1 - \alpha$. It is strongly A-stable and possesses the full smoothing property which is critically important for the case of rough initial and/or boundary conditions. Further, it contains a minor amount of numerical dissipation, which is helpful in the damping of temporal oscillations. The theoretical and numerical study of fractional θ-scheme including the choice of θ, modified time-stepping and a posteriori error estimation are discussed in [72, 100, 124, 125]. The fractional θ-schemes combine several desirable properties like strongly A-stable and second order accurate. Strictly speaking, it brings together the advantages of Crank-Nicholson and Backward-Euler methods.

Modified fractional step schemes

A modified θ-scheme with comparatively larger time steps can be written in a three consecutive sub steps. Here $\theta = 1 - \frac{1}{\sqrt{2}}$ and $\rho^0 = \rho_0$ for all $m \geq 0$ and ρ^m is known.

$$\rho^{m+1-\theta} + \theta k f\left(\rho^{m+\theta}, t^{m+\theta}\right) = \rho^{m},$$

$$\rho^{m+\theta} = \frac{1-\theta}{\theta}\rho^{m+\theta} + \frac{2\theta - 1}{\theta}\rho^{m},$$

$$\rho^{m+1} + \theta k f\left(\rho^{m+1}, t^{m+1}\right) = \rho^{m+1-\theta}.$$

The promising attributes of this type of θ-schemes include strongly A-stable, fully implicit, second and nearly third order accurate and the boundedness of the numerical solution [100, 125]. Based on this discussion the backward Euler method has been used for the temporal discretization.

3.3 Spatial discretization

Recently, finite element method is emerged as a strong numerical technique to solve differential equations with practical applications. In the initial stages the method was successfully employed in aerodynamics, within a short span of time it became famous among researchers in structure mechanics, fluid mechanics, engineering, applied mathematics and numerics communities. The technique provides an approximate solution to a large class of physical problems governed by partial differential equations. For a brief historical development and applications of finite element method for variety of problems, we refer interested reader to Braess[8] and Zienkiewicz [143]. Finite element method is most flexible to apply w.r.t. geometries (domain shape) and boundary conditions. The convergence of the solution can be improved while choosing an appropriate basis function and high mesh refinement. FEM provide system of algebraic equations which can be solved through efficient and accurate direct and/or iterative solvers from open source software tools like FEATFLOW.
Literature review reveals that there are large class of finite element method [106, 143] further description is beyond the scope of this section. Although, in the subsequent sections we introduce Galerkin finite element method and modification in the matrix representation to include the stabilization techniques. We restrict the presentation to a sample linear elliptic problem. Assuming a sufficiently smooth boundary, we show error bounds of order h^k in the H^1-norm and order h^{k+1} in the L^2-norm, where k is the degree of polynomial for the underlying finite element space and h is the fixed length of the mesh.

The standard finite element approximation is mainly based on the Galerkin FEM formulation through method of weighted residuals.

Method of weighted residual

The solution of ρ must belong to some special class of space of function which are continuous and contain first and second order derivatives. In other words, it must be smooth to get a wide class of admissible functions. First of all, we develop weak formulation. The generalized solution is supposed to satisfy the weak form. Here we would like to notice some of the integrals that arise during finite element approximation. Let us assume $\mathscr{R}$ denote the residual of a simple PDE derived from system of the differential equations (3.1)–(3.2) with a source function g.

$$\mathscr{R}[\rho_h] \quad = \quad \partial_t \rho_h + \boldsymbol{v} \cdot \nabla \rho_h + \rho_h \nabla_{\Gamma(t)} \cdot \boldsymbol{v} - g. \qquad (3.12)$$

A solution ρ_h should be sufficiently smooth. If ρ is an exact solution then we get $\mathscr{R}[\rho] = 0$. In the weighted residual formulation we multiply the residual by a suitable test function and integrate over the computational domain.

$$\int_\Omega \mathscr{R}[\rho] v d\Omega = 0, \quad \text{for all} \quad v \in \mathsf{V},$$

with V is the space of test function vanishing on the Dirichlet boundary condition. This can be obtained if the projection of the residual is orthogonal to all test functions $v \in \mathsf{V}$. Using Green's formula for integration by parts and substitution of boundary conditions (3.7)–(3.8) lead to weak form of the solution. The residual formulation is handy to shift derivatives from the function of trial space ρ onto the test function. In consequence, we obtain linear and/or bi/tri-linear forms will be discussed in §3.4.2. The classical residual approximation is applicable in Galerkin finite element method which is applied for a large class of mathematical problems in comparison to other numerical counterparts.

3.4 Laplace-Beltrami equation

For simplicity of the problem let us assume the Poisson equation on an arbitrary surface. We start via describing the prerequisite assumption for weak formulation on the surface and provide proofs of related lemmas and theorems. The state-of-the-art literature on surface PDEs can be found in [27, 29, 31, 97].
Consider

$$\rho : \Gamma \to \mathbb{R},$$

$$-\Delta_\Gamma \rho + c\rho = f \text{ on } \Gamma, \tag{3.13}$$

with $f \in L^2(\Gamma)$, constant $c \geq 0$ and $\int_\Gamma f d\Gamma = 0$ in order to guarantee uniqueness of solutions assume $\rho \in H^1(\Gamma)$, then the weak formulation of (3.13) reads:

$$\int_\Gamma (\nabla_\Gamma \rho \cdot \nabla_\Gamma \varphi + c\rho\varphi)\, d\Gamma = \int_\Gamma f\varphi d\Gamma \tag{3.14}$$

Here to achieve the desire solution, we state the following lemma [27, 29, 31, 97].

Lemma 3.4.1. *There exists a unique solution $\rho \in H^1(\Gamma)$ for (3.14) if $\Gamma \in C^3$ and $\rho \in H^2(\Gamma)$ with the bound*

$$\|\rho\|_{H^2(\Gamma)} \leq \|f\|_{L^2(\Gamma)}. \tag{3.15}$$

Moreover, we introduce a bilinear form $a(\cdot,\cdot)$ as:

$$a(\cdot,\cdot) : H^1(\Gamma) \times H^1(\Gamma) \to \mathbb{R}$$

and a linear form $l(\cdot)$ as:

$$l(\cdot) : H^1(\Gamma) \to \mathbb{R},$$

the bilinear and linear forms from equation (3.14) as:

$$a(\rho,\varphi) := \int_\Gamma \nabla_\Gamma \rho \cdot \nabla_\Gamma \varphi d\Gamma. \tag{3.16}$$

$$l(\varphi) := \int_\Gamma f\varphi d\Gamma. \tag{3.17}$$

Using the notations from (3.16) and (3.17) the equation (3.14) becomes:

$$a(\rho,\varphi) = l(\varphi) \quad \text{for all} \quad \rho \in H^1(\Gamma)\,. \tag{3.18}$$

Where φ is the basis function and the transport property of the basis function is stated in the following remark.

Remark 12. *Let $\varphi : \Gamma_h \to \mathbb{R}$ is the nodal basis function and φ_j is the value of basis function at node j and satisfying the following transport property [25, 29, 31, 97].*

$$\partial_t^\bullet \varphi_j = 0\,. \tag{3.19}$$

Proof. Since for the nodal basis function, we have

$$\varphi_j\left(\mathbf{x}^i(t),t\right) = \delta_j^i\,. \tag{3.20}$$

Where δ_j^i is the Dirac delta function. The differentiation w.r.t. time variable, gives

$$0 = \frac{d}{dt}\varphi_j\left(\mathbf{x}^i(t),t\right) = \frac{\partial}{\partial t}\varphi_j\left(\mathbf{x}^i(t),t\right) + \nabla\varphi_j\left(\mathbf{x}^i(t),t\right)\cdot\mathbf{x}_t^i(t)\,. \tag{3.21}$$

Introducing V_h as the discrete velocity function, we have

$$0 = \frac{\partial}{\partial t}\varphi_j\left(\mathbf{x}^i(t),t\right) + \nabla\varphi_j\left(\mathbf{x}^i(t),t\right)V_h\left(\mathbf{x}^i(t),t\right) = \partial_t^\bullet\varphi_j\,. \tag{3.22}$$

Hence this result prove an important property of nodal basis function. □

Discrete Laplace-Beltrami equation

To find the discrete counterpart of the equation (3.14) through finite element method, given a triangulation of the discrete surface Γ_h. We take a continuous piecewise bi-linear (Q_1) finite element space on Γ_h and $\rho_h \in S_h$ such that

$$S_h := \{\varphi_h \in C(\Gamma_h) : \varphi_h|_e \in Q_1 \quad \text{for all elements}\},$$

$$\int_{\Gamma_h} (\nabla_\Gamma \rho_h \cdot \nabla_{\Gamma_h}\varphi_h + c\rho_h\varphi_h)\,d\Gamma = \int_{\Gamma_h} f\varphi_h d\Gamma_h\,, \tag{3.23}$$

assuming $\int_{\Gamma_h} f d\Gamma_h = 0$ if $c = 0$ and $f \in L^2(\Gamma_h)$ with some approximation of f which is assumed to satisfy:

$$\|\ f\|_{L^2(\Gamma_h)} \le c\|f\|_{L^2(\Gamma)}\,. \tag{3.24}$$

3.4.1 Surface PDEs

Now we provide a general advection/reaction-diffusion equation of an evolving surface PDE. We use the mathematical formulation from the preceding chapter 2. The following parabolic chemotaxis-like PDE on an evolving-in-time surface can be derived from (3.2) the general model described in §3.1 with the following parameter setting:

$$j=1, \quad D_\rho^j = D, \quad \chi_\rho^j = \chi, \quad \mathbf{w}_\rho^j = \nabla_{\Gamma(t)} c \quad \text{and} \quad g^j(c,\rho) = g(\rho),$$

we get

$$\frac{\partial^* \rho}{\partial t} = D\Delta_{\Gamma(t)}\rho - \nabla_{\Gamma(t)} \cdot (\chi \rho \nabla_{\Gamma(t)} c) + g(\rho) \text{ on } \Gamma(t) \times T\,. \tag{3.25}$$

Where the derivative $\dfrac{\partial^* \rho}{\partial t}$ on the left hand side is due to evolution of surface $\Gamma(t)$ can be defined as:

$$\frac{\partial^* \rho}{\partial t} = \partial_t^\bullet \rho + \rho \nabla_{\Gamma(t)} \cdot \boldsymbol{v} \tag{3.26}$$

the Leibniz formula defined in equation (2.65) states in the following manner:

$$\frac{d}{dt}\int_{\Gamma(t)} \rho = \int_{\Gamma(t)} \partial_t^\bullet \rho + \rho \nabla_{\Gamma(t)} \cdot \boldsymbol{v} \tag{3.27}$$

here $\partial_t^\bullet \rho = \partial_t \rho + \boldsymbol{v} \cdot \nabla \rho$ denotes the advective surface material derivative. The surface velocity $\boldsymbol{v} = V\boldsymbol{n} + \boldsymbol{v}_S$ can be decomposed into velocity components in the normal direction $V\boldsymbol{n}$ (where $\boldsymbol{n}$ is the surface outward unit normal vector) and the tangential component $\boldsymbol{v}_S$, respectively. Using the relations:

$$\nabla_\Gamma \cdot \boldsymbol{v} = \nabla_\Gamma \cdot \boldsymbol{V\boldsymbol{n} + \boldsymbol{v}_S} = \nabla_\Gamma V \cdot \boldsymbol{n} + V\nabla_\Gamma \cdot \boldsymbol{n} + \nabla_\Gamma \cdot \boldsymbol{v}_S = V\nabla_\Gamma \cdot \boldsymbol{n} + \nabla_\Gamma \cdot \boldsymbol{v}_S = -VH + \nabla_\Gamma \cdot \boldsymbol{v}_S\,,$$

$$\boldsymbol{v} \cdot \nabla \rho = V\boldsymbol{n} \cdot \nabla \rho + \boldsymbol{v}_S \cdot \nabla \rho = V\frac{\partial \rho}{\partial \boldsymbol{n}} + \boldsymbol{v}_S \cdot \nabla \rho\,.$$

Where H is mean curvature discussed in (2.117) and V is the velocity defined in (2.115) along the normal. The equation (3.25) can be rewritten in the following form

$$\partial_t \rho + \boldsymbol{v}_S \cdot \nabla \rho - VH\rho + V\frac{\partial \rho}{\partial \boldsymbol{n}} + \rho \nabla_{\Gamma(t)} \cdot \boldsymbol{v}_S = D\Delta_{\Gamma(t)}\rho - \nabla_{\Gamma(t)} \cdot (\chi \rho \nabla_{\Gamma(t)} c) + g(\rho)\,. \tag{3.28}$$

Simply in terms of the surface material derivative, we have

$$\partial_t^\bullet \rho + \rho \nabla_\Gamma \cdot \boldsymbol{v} = D\Delta_{\Gamma(t)}\rho - \nabla_{\Gamma(t)} \cdot (\chi \rho \nabla_{\Gamma(t)} c) + g(\rho)\,. \tag{3.29}$$

The numerical treatment of the general model §(3.1) or the recently derived equation (3.29) can be complemented by usual prescription of initial conditions (3.6) and certain boundary conditions e.g., Dirichlet boundary condition (3.7), homogeneous Neumann boundary condition (3.8) and/or a mixed-type boundary conditions. Now we will derive the variational formulation for the obtained equation (3.29) on surface.

3.4.2 Variational formulation

The finite element formulation derived here is based on the conventional Galerkin type FEM, known as evolving surface finite element method [26, 29, 33, 114]. We will discuss the fully discretized finite element scheme for the general model §3.1. Moreover, we keep in hand the formulation derived through the level set approach §2.4 to capture the evolution of the interface. Let us proceed with the weak formulation of the equation (3.29) assuming that the solution ρ exists in some sufficiently regular space V. We multiply the equation (3.29) by a suitable test function φ. Let $\varphi \in V_h \subset V$, now compute integral of the equation over the underlying computational domain Ω. Here φ denotes test function assume the level set function $\phi \in C^2(\Omega)$, then using the Coarea formula (2.121) we can write the variational formulation of (3.29) as:

$$\begin{aligned}\int_\Omega (\partial_t^\bullet \rho + \rho \nabla_\Gamma \cdot \boldsymbol{v})\, \varphi |\nabla \phi| &= \int_\Omega \left(D\Delta_{\Gamma(t)}\rho - \nabla_{\Gamma(t)} \cdot (\chi \rho \nabla_{\Gamma(t)} c) \right) \varphi |\nabla \phi| \\ &+ \int_\Omega g(\rho)\varphi |\nabla \phi|. \end{aligned} \tag{3.30}$$

Due to the implicit surface Leibniz formula from lemma 2.5.3 the left hand side is calculated as:

$$\begin{aligned}\int_\Omega (\partial_t^\bullet \rho + \rho \nabla_{\Gamma(t)} \cdot \boldsymbol{v}) \varphi |\nabla \phi| &= \frac{d}{dt}\int_\Omega \rho \varphi |\nabla \phi| \\ -\int_\Omega \rho \partial_t^\bullet \varphi |\nabla \phi| &+ \int_{\partial\Omega} \rho \varphi \boldsymbol{v} \cdot \boldsymbol{n}_{\partial\Omega} |\nabla \phi|. \end{aligned} \tag{3.31}$$

In general the boundary integral cannot be neglected. Numerical experiments reveals that the non-inclusion of boundary integral into the numerical scheme can cause kinks and wiggles in the solution near boundaries [114]. This non-physical behavior may spread throughout the domain as time evolves. Since

$$\left(D\nabla_{\Gamma(t)}\rho - \chi \rho \nabla_{\Gamma(t)} c \right) \cdot \boldsymbol{n} = 0\,,$$

integration by parts in (2.132) gives

$$\begin{aligned}&\int_\Omega (D\nabla_{\Gamma(t)}\rho - \chi\rho\nabla_{\Gamma(t)}c) \cdot \nabla_{\Gamma(t)}\varphi |\nabla\phi| = \\ &-\int_\Omega \varphi \nabla_{\Gamma(t)} \cdot (D\nabla_{\Gamma(t)}\rho - \chi\rho\nabla_{\Gamma(t)}c) |\nabla\phi| \\ &+\int_{\partial\Omega} (D\nabla_{\Gamma(t)}\rho - \chi\rho\nabla_{\Gamma(t)}c) \cdot \boldsymbol{n}_{\partial\Omega} \varphi |\nabla\phi|\,. \end{aligned} \tag{3.32}$$

The boundary integral

$$\int_{\partial\Omega} (D\nabla_{\Gamma(t)}\rho - \chi\rho\nabla_{\Gamma(t)}c) \cdot \boldsymbol{n}_{\partial\Omega} \varphi |\nabla\phi|$$

on the right hand side of (3.32) cannot be neglected in general sense as well. Its numerical treatment though can be performed in a similar way to the boundary integral $\int_{\partial\Omega}\rho\varphi\boldsymbol{v}\cdot\boldsymbol{n}_{\partial\Omega}|\nabla\phi|$ in the equation (3.31). For brevity, everywhere in this work we assume that the boundary $\partial\Omega$ is aligned with some level set Γ_r and therefore $(D\nabla_{\Gamma(t)}\rho-\chi\rho\nabla_{\Gamma(t)}c)\cdot\boldsymbol{n}_{\partial\Omega}=0$. Applying (2.133) and (3.32) to (3.30), we obtain

$$\frac{d}{dt}\int_\Omega\rho\varphi|\nabla\phi|+\int_\Omega(D\nabla_{\Gamma(t)}\rho-\chi\rho\nabla_{\Gamma(t)}c)\cdot\nabla_{\Gamma(t)}\varphi|\nabla\phi|=$$

$$\int_\Omega\rho\partial_t^\bullet\varphi|\nabla\phi|-\int_{\partial\Omega}\rho\varphi\boldsymbol{v}\cdot\boldsymbol{n}_{\partial\Omega}|\nabla\phi|+\int_\Omega g(\rho)\varphi|\nabla\phi|. \tag{3.33}$$

For the discretization in space we use conforming bilinear/trilinear finite elements with the corresponding space of test functions $Q_h=\text{span}\{\varphi_1,\dots,\varphi_N\}$. Therefore, using the transport property of test function from remark 12, we have

$$\dot{\varphi}=\boldsymbol{v}\cdot\nabla\varphi \tag{3.34}$$

and the semi-discretization problem for (3.33) reads: Find $\rho_h\in Q_h$ such that

$$\frac{d}{dt}\int_\Omega\rho_h\varphi|\nabla\phi|+\int_\Omega(D\nabla_{\Gamma(t)}\rho_h-\chi\rho\nabla_{\Gamma(t)}c)\cdot\nabla_{\Gamma(t)}\varphi|\nabla\phi|= \tag{3.35}$$

$$\int_\Omega\rho_h\boldsymbol{v}\cdot\nabla\varphi|\nabla\phi|-\int_{\partial\Omega}\rho_h\varphi\boldsymbol{v}\cdot\boldsymbol{n}_{\partial\Omega}|\nabla\phi|+\int_\Omega g(\rho)\varphi|\nabla\phi|\quad\forall\varphi\in Q_h.$$

Fully-discrete scheme of the implicit version:
Given ρ_h^m at the t^m-th time instance and the time step $\Delta t=t^{m+1}-t^m$, then solve for ρ_h^{m+1}

$$\frac{1}{\Delta t}\int_\Omega\rho_h^{m+1}\varphi|\nabla\phi^{m+1}|+\int_\Omega(D\nabla_{\Gamma^{m+1}}\rho_h^{m+1}-\mathbf{w}\rho_h^{m+1})\cdot\nabla_{\Gamma^{m+1}}\varphi|\nabla\phi^{m+1}|$$

$$-\int_\Omega\rho_h^{m+1}\boldsymbol{v}^{m+1}\cdot\nabla\varphi|\nabla\phi^{m+1}|+\int_{\partial\Omega}\rho_h^{m+1}\varphi\boldsymbol{v}^{m+1}\cdot\boldsymbol{n}_{\partial\Omega}|\nabla\phi^{m+1}|$$

$$=\frac{1}{\Delta t}\int_\Omega\rho_h^m\varphi|\nabla\phi^m|+\int_\Omega g\varphi|\nabla\phi^m|, \tag{3.36}$$

for all $\varphi\in S_h$. Using $\{\varphi_i\}$ as test functions for quadrilateral finite elements in space. The matrix form of the equation (3.36) is given as follows:

$$\begin{aligned}[\boldsymbol{M}(|\nabla\phi^{m+1}|) &+ \Delta t\boldsymbol{L}(D|\nabla\phi^{m+1}|)-\Delta t\boldsymbol{K}(\mathbf{w}^m|\nabla\phi^{m+1}|)\\ &- \Delta t\boldsymbol{N}(\boldsymbol{v}^{m+1}|\nabla\phi^{m+1}|)+\Delta t\boldsymbol{R}(|\nabla\phi^{m+1}|)]\rho_h^{m+1}\\ &= \boldsymbol{M}(|\nabla\phi^m|)\rho_h^m+\Delta t\boldsymbol{G}(|\nabla\phi^m|).\end{aligned} \tag{3.37}$$

Where $\boldsymbol{M}(\cdot)$ denotes the consistent mass matrix, $\boldsymbol{L}(\cdot)$ is the discrete Laplace-Beltrami operator, $\boldsymbol{K}(\cdot)$ is the discrete on-surface advection operator with the linearized velocity $\mathbf{w}^m$, $\boldsymbol{N}(\cdot)$ is the discrete operator due to the surface evolution, $\boldsymbol{R}(\cdot)$ is the discrete boundary integral and the discrete kinetic term $\boldsymbol{G}(\cdot)$ with the entries defined by the formulae

$$\boldsymbol{M} = m_{ij}(\psi) = \int_{\Omega} \varphi_i \varphi_j \psi. \tag{3.38}$$

$$\boldsymbol{L} = l_{ij}(\psi) = \int_{\Omega} \rho_{h\Gamma} \nabla \varphi_i \cdot \nabla \varphi_j \psi. \tag{3.39}$$

$$\boldsymbol{K} = k_{ij}(\psi) = \int_{\Omega} \varphi_i \psi \cdot \rho_{h\Gamma} \varphi_j. \tag{3.40}$$

$$\boldsymbol{N} = n_{ij}(\psi) = \int_{\Omega} \varphi_i \boldsymbol{v}^{m+1} \cdot \nabla \varphi_j \psi. \tag{3.41}$$

$$\boldsymbol{R} = r_{ij}(\psi) = \int_{\partial\Omega} \varphi_i \varphi_j \boldsymbol{v}^{m+1} \cdot \boldsymbol{n}_{\partial\Omega} \psi\,. \tag{3.42}$$

$$\boldsymbol{G} = g_i(\psi) = \int_{\Omega} \varphi_i g_i \psi. \tag{3.43}$$

Where the matrices $\boldsymbol{K}(\cdot)$, $\boldsymbol{N}(\cdot)$ and $\boldsymbol{R}(\cdot)$ can cause to produce oscillatory solution consequently, in the next section the stabilization has been discussed.

3.5 Stabilization

In case of surface PDEs the inclusion of boundary integral, the surface convection and convective dominated problem like chemotaxis require a stabilized FEM to achieve an adequate solution. In principal, the actual difference between the exact solution of the partial differential equation and an approximate solution obtained through numerical techniques is the sum of the numerical errors. Strictly speaking, none of the numerical solution can replace the closed-form solution but an improved numerical technique with reduction of errors (iteration, round off and discretization errors) can bring the numerical solution nearer to its analytic counterpart. The following criteria with a rigorous analysis are mainly concerned with the stabilization of a numerical solver to achieve a robust and an accurate physical solution.

Consistency:

The truncation error should vanish or mathematically the discretization of a partial differential equation should converge to the exact solution as the mesh size h approaches zero.

Stability of algorithm:

The numerical errors which occur due to solution of discretized partial differential equation should not increase.

Convergence:

The numerical solution should approach the exact solution of the partial differential equation and must converge as the mesh size approach to zero. From equivalence theorem the consistency and stability of the numerical scheme give convergence of the solution. For practical interest, the experimental order of convergence can be investigated numerically by comparing the results computed on a series of successively refined grids. Numerical results concerned to experimental order of convergence will be shown in the subsequent chapters.

Conservation laws:

The discretization of the PDEs must obey the laws of conservation of mass, momentum and energy. In other words it should avoid artificial source and sink at the discrete level.

Boundedness or positivity preserving:

The solution of the problem needs to be bounded, the physical quantities like concentration and densities must be non-negative and should avoid non-physical oscillations and spurious wiggles.

Stabilization of the convective terms is essential to achieve a physically accurate solution. These terms are occurring due to surface convection and chemotaxis-type PDEs. In the CFD circle, FEM upwinding [123], FEM streamline-diffusion [53] and algebraic flux correction of FCT/TVD types [61, 114, 118, 120] are among most frequently used techniques to achieve a physically accurate solution. Here we briefly introduce the AFC techniques.

3.5.1 Algebraic flux correction

In this section, we illustrate and develop the algebraic flux correction (AFC) with Galerkin finite element formulation for solution of the surface PDEs with convective dominated problems. We will develop multidimensional high resolution finite element schemes on the surface. Numerical experiments suggest that the pure Galerkin method produces oscillatory solutions as a result of surface convection. Consequently, we have to eliminate the negative off-diagonal coefficients from fully discrete transport operator and employ a central space discretization of oscillatory convective terms. This technical modification of the convective term provide a low order scheme which is nonoscillatory but highly diffusive. In order to over-come this drawback, a compensating antidiffusion is added to the solution. We will thoroughly discuss two closely flux correction techniques which are used in this thesis for convective dominated surface PDEs. These techniques are known as algebraic flux correction methods of FCT and TVD-types based on implicit finite element methods.

In principal, each numerical scheme has its own limitation on applicability sometimes only suitable to specific problems. In case of geometries (e.g., evolving-surface) with complex physical phenomena (convection/advection/chemotaxis) with a variety of discretization schemes we may get non-physical solutions. In consequences, we need algebraic flux correction algorithms. In short, the main purpose is to design the AFC methods to achieve a positivity preserving finite element solution for PDEs on surface.

The high resolution nonlinear schemes of AFC for convective dominated problems are introduced by Boris and Book [6]. Furthermore, Zalesak [141] proposed a general framework to design flux-corrected transport based on fully multidimensional linear high and low order approximation. Möller et al. [75, 76] and Kuzmin [60] added further development in the algorithm and extended it for large class of flow problems and chemotaxis like PDEs [118, 120]. The foundation of the current AFC technique is mainly based on that of Möller [75], Kuzmin [60], Kuzmin and Turek [61], Möller et al. [76] and Strehl et al. [118, 120]. From these literature we concluded that the introduction of modern front capturing techniques put forward set of mathematical constraints on the discrete solution to give a physically accurate solution through preventing the evolution of spurious over and under-shoots in the vicinity of steep gradient [75, 76].

Now we present a short description of the embedding of the FCT/TVD-stabilized algorithm into the implicit algorithm (3.36) more precisely into its discrete counterpart written in the matrix form (3.37).

The following algorithm will use in the process.

- High order schemes may fail to produce the desired results.
- Low order schemes may provide desired results but can be less accurate.
- A schematic process to decompose the difference between the above into sum of skew-symmetric inter-nodal fluxes can be manipulated keeping in view mass conservation.
- Finally, a mechanism to adjust the antidiffusive fluxes in an adaptive way so that the imposed limitations can be satisfied for a given solution.

In case of AFC we adopt an algebraic technique to design a high resolution method which consists of certain mathematical constraints on discrete operators to get favorable matrix properties. Let us assume the semi-discrete scheme of the form

$$\frac{d\rho_i}{dt} = \sum_{i,j} c_{ij}\,(\rho_j - \rho_i) \quad c_{ij} \geq 0 \quad \forall j \neq i. \tag{3.44}$$

Harten's TVD theorem suggests that the above equation hold local extremum diminishing (LED). After time discretization such schemes are still positivity-preserving

provided that the solution converge to steady state and satisfy an algebraic system of the form.

$$\boldsymbol{M}\rho^{m+1} = \boldsymbol{B}\rho^{m} + g^{m}(\rho), \tag{3.45}$$

where $\boldsymbol{M} = \{m_{ij}\}$ is $\boldsymbol{M}$-matrix, $\boldsymbol{B} = \{b_{ij}\}$ and $g(\rho) = \{g_i(\rho)\}$ have no negative entries. These condition lead to positivity of the previous solution to the new one.

$$\rho^{m} \geq 0 \implies \rho^{m+1} = [\boldsymbol{M}^{-1}\boldsymbol{B}\rho^{m} + g^{m}(\rho)] \geq 0. \tag{3.46}$$

If this spatial discretization is local extremum diminishing then the coefficients of the off-diagonal entries of both matrices have right sign. The positivity condition for the diagonal entries of $\boldsymbol{B}$ yields a readily computable upper bound in an admissible time step.

$$1 + \Delta t(1-\theta)\min c_{ii}^{n} \geq 0, \quad \text{for} \quad 0 \leq \theta < 1. \tag{3.47}$$

In general these algebraic constraints are sufficient but not necessary condition for numerical scheme to be LED or positivity preserving. Godunov theorem states that linear schemes satisfying these conditions are at most first order. In case of a high order discretization which may fails to satisfy the above mentioned conditions, thus can be adjusted with AFC method.

The fundamental steps of the AFC technique can be drawn in the following patterns.
Consider an unsteady continuity equation for a scalar quantity ρ transported by a known velocity field $\boldsymbol{v}$.

$$\frac{\partial \rho}{\partial t} + \nabla \cdot (\boldsymbol{v}\rho) = 0\,. \tag{3.48}$$

After semi-discretization in space by Galerkin finite element method the above equation transformed with vector at nodal values

$$\boldsymbol{M}_C \frac{d\rho}{dt} = K\rho\,, \tag{3.49}$$

where $\boldsymbol{M}_C = \{m_{ij}\}$ represents the consistent mass matrix and $\boldsymbol{K} = \{k_{ij}\}$ is the discrete counterpart of continuous transport operator. For linear discretizations the mathematical constraints (3.44) and (3.45) can be obtained through discrete upwinding scheme [61, 76]. In the semi-discretized FE scheme (3.49) we can impose the following matrix manipulation. First of all, we use mass lumping and replace the consistent mass matrix $\boldsymbol{M}_C$ by lumped mass matrix $\boldsymbol{M}_L$. Secondly, to avoid the negative off-diagonal entries add artificial diffusion operator $\boldsymbol{D} = d_{ij}$. This post processing convert equation (3.49) into the following form

$$\boldsymbol{M}_L \frac{d\rho}{dt} = \mathscr{L}\rho \quad \text{where} \quad \mathscr{L} = \boldsymbol{K} + \boldsymbol{D}. \tag{3.50}$$

As shown by Möller [75], Kuzmin and Turek [61] the positivity constraints can be readily enforced at the discrete level using a conservative manipulation of the matrices $\boldsymbol{M} = \{m_{ij}\}$ and $\boldsymbol{K} = \{k_{ij}\}$ assuming that the source term $g^m(\rho)$ does not cause problem to positivity. The former is approximated by its diagonal counterpart $\boldsymbol{M}_L$ constructed using row-sum mass lumping

$$\boldsymbol{M}_L := \text{diag}\{m_i\} \quad \text{where} \quad m_i = \sum_j m_{ij}(|\nabla\phi|). \tag{3.51}$$

Now all negative off-diagonal entries of $\boldsymbol{K}$ are eliminated by adding an artificial diffusion operator $\boldsymbol{D}$. To obey conservation principals, this matrix must be symmetric with zero row and column sums. For any pair of neighboring nodes i and j the entry d_{ij} is defined as [61, 75]

$$d_{ij} = \begin{cases} \max\{-k_{ij}, 0, -k_{ji}\}, & j \neq i, \\ -\sum\limits_{k\neq i} d_{ik}, & j = i. \end{cases} \tag{3.52}$$

It is clear that $d_{ij} = d_{ji}$. Thus the result is a positivity-preserving discretization of low order.

The addition of artificial diffusion d_{ij} leads to over diffusive solution . In order to avoid the formation of non-physical undershoots and overshoots, the raw antidiffusive fluxes f_{ij} should be multiplied by a suitable correction factor.
The equation (3.50) is rewritten as follows:

$$\boldsymbol{M}_L \frac{d\rho}{dt} = \mathscr{L}\rho + \tilde{f}(\rho) \quad \text{where} \quad \tilde{f}(\rho) = \sum_{j\neq i} \alpha_{ij} f_{ij}, \tag{3.53}$$

here $0 \leq \alpha_{ij} \leq 1$ is a correction factor. Keeping in view the positivity constraints the main task of flux limiter is to get an optimal value of each correction factor and to remove the artificial diffusion [75, 76]. In case of $\alpha_{ij} = 0$, we get low order scheme and for $\alpha_{ij} = 1$ the high order scheme.

Consider ρ_h is a positivity preserving solution and by construction of the difference between the residual of the low order scheme and that of the underlying Galerkin approximation, denoted by F as follows:

$$F = (\boldsymbol{M}_L - \boldsymbol{M}_C(|\nabla\phi|)) \frac{\rho_h^{m+1} - \rho_h^m}{\Delta t} - \boldsymbol{D}\,\rho_h^{m+1} \tag{3.54}$$

admits a conservative decomposition into a sum of skew-symmetric antidiffusive fluxes

$$F = \sum_{j\neq i} f_{ij} \quad \text{where} \quad f_{ij} = \left[m_{ij}\frac{d}{dt} + d_{ij} \right] (\rho_{h_i} - \rho_{h_j}) = -f_{ji} \;\forall\, j \neq i. \tag{3.55}$$

To obtain a high resolution solution profile while maintaining the scheme positivity-preserving, we apply the *limiting process*. It means that each flux is multiplied by a

solution-dependent correction factor $\alpha_{ij} \in [0,1]$ and is inserted into the right-hand side of the nonoscillatory low-order scheme. The original Galerkin discretization corresponds to the setting $\alpha_{ij} := 1$. It may be used in those regions where the numerical solution is smooth and well-resolved. The parameter setting $\alpha_{ij} := 0$ is appropriate in the neighborhood of steep fronts. Roughly speaking, we can say that the flux limiting is of the TVD-type, if the antidiffusive flux limiting takes into account only modification of the convective operator $\boldsymbol{K}$, i.e. $F = -\boldsymbol{D}\,\rho_h^{m+1}$. Otherwise, we can say that the flux limiting is of the FCT-type, if the antidiffusive flux limiting takes into account including modification of the convective operator $\boldsymbol{K}$ and the corresponding modification of the mass matrix $\boldsymbol{M}$ i.e.,

$$F = (\boldsymbol{M}_L - \boldsymbol{M}(|\nabla\phi|))\,\frac{\rho_h^{m+1} - \rho_h^m}{\Delta t} - \boldsymbol{D}\,\rho_h^{m+1}.$$

In essence, the off-diagonal entries of the sparse matrices $\boldsymbol{M}$ and $\boldsymbol{K}$ are replaced by

$$m_{ij}^* := \alpha_{ij} m_{ij} \quad \text{and} \quad k_{ij}^* := k_{ij} + (1-\alpha_{ij}) d_{ij}$$

while the diagonal coefficients of the flux-corrected Galerkin operators are given by

$$m_{ii}^* := m_i - \sum_{j\neq i} \alpha_{ij} m_{ij} \quad \text{and} \quad k_{ii}^* := k_{ii} - \sum_{j\neq i} (1-\alpha_{ij}) d_{ij}.$$

In the implicit FEM-FCT schemes [61, 75] the optimal values of α_{ij} are determined using Zalesak's algorithm [141]. The limiting process begins with canceling all fluxes that are diffusive in nature and tend to flatten the solution profiles. The required modification is:

$$f_{ij} := 0 \quad \text{if} \quad f_{ij}(\rho_{hj} - \rho_{hi}) > 0,$$

where ρ_h is a positivity-preserving solution of low order [61, 75].

The remaining fluxes are genuinely antidiffusive and the computation of the correction factor α_{ij} involves the following algorithmic steps:

(a) Compute the sums of positive/negative antidiffusive fluxes into node i

$$S_i^+ = \sum_{j\neq i} \max\{0, f_{ij}\}, \qquad S_i^- = \sum_{j\neq i} \min\{0, f_{ij}\}.$$

(b) Compute the distance to a local extremum of the auxiliary solution ρ_h

$$Q_i^+ = \max\{0, \max_{j\neq i}(\rho_{hj} - \rho_{hi})\}, \qquad Q_i^- = \min\{0, \min_{j\neq i}(\rho_{hj} - \rho_{hi})\}.$$

(c) Compute the nodal correction factors for the net increment to node i

$$R_i^+ = \min\left\{1, \frac{m_i Q_i^+}{\Delta t S_i^+}\right\}, \qquad R_i^- = \min\left\{1, \frac{m_i Q_i^-}{\Delta t S_i^-}\right\}.$$

(d) Check the sign of the antidiffusive flux and apply the correction factor

$$\alpha_{ij} = \begin{cases} \min\{R_i^+, R_j^-\}, & \text{if } f_{ij} > 0, \\ \min\{R_i^-, R_j^+\}, & \text{otherwise.} \end{cases}$$

Summary of AFC test cases

To summarize this section we present the flow chart of required algebraic manipulations of the FCT/TVD stabilization technique for the implicit fully-discrete scheme

1. Obtain the low-order scheme

$$\begin{aligned} [\boldsymbol{M}_L \quad + \quad & \Delta t \boldsymbol{L}(D|\nabla\phi^{m+1}|) - \Delta t \mathscr{L}(|\nabla\phi^{m+1}|)]\rho_h^{m+1} \\ & = \boldsymbol{M}_L\rho_h^m + \Delta t \boldsymbol{G}(|\nabla\phi^m|), \end{aligned} \tag{3.56}$$

   by performing mass lumping $\boldsymbol{M} \to \boldsymbol{M}_L$ and transforming the high-order operator $\boldsymbol{K}$ into its nonoscillatory low-order counterpart $\mathscr{L}$ by adding a discrete diffusion operator $\boldsymbol{D}$ stated in (3.50).

2. Remove excessive diffusion where possible by adding the limited antidiffusion operator $F(\alpha)$

$$\begin{aligned} [\boldsymbol{M}_L \quad + \quad & \Delta t \boldsymbol{L}(D|\nabla\phi^{m+1}|) - \Delta t \mathscr{L}(|\nabla\phi^{m+1}|)]\rho_h^{m+1} + F(\alpha) \\ & = \boldsymbol{M}_L\rho_h^m + \Delta t \boldsymbol{G}(|\nabla\phi^m|), \end{aligned} \tag{3.57}$$

   where $F(\alpha)$ is constructed according to the *limiting process* described above and α's are found from algorithmic steps (a)–(d).

Latter in the numerical experiments we need to distinguish the following five test cases:

- The implicit scheme without stabilization (IS) corresponds to (3.37).
- The explicit scheme without stabilization (ES) corresponds to

$$\begin{aligned} [\boldsymbol{M}(|\nabla\phi^{m+1}|) \quad + \quad & \Delta t \boldsymbol{L}(D|\nabla\phi^{m+1}|) - \Delta t \boldsymbol{K}(\mathbf{w}^m|\nabla\phi^{m+1}|) \\ + \quad & \Delta t \boldsymbol{R}(|\nabla\phi^{m+1}|)]\,\rho_h^{m+1} = \boldsymbol{M}(|\nabla\phi^m|)\rho_h^m \\ + \quad & \Delta t \boldsymbol{N}(\boldsymbol{v}^m|\nabla\phi^m|)\rho_h^m + \Delta t \boldsymbol{G}(|\nabla\phi^m|). \end{aligned} \tag{3.58}$$

- The implicit scheme without boundary term (ISwB) corresponds to (3.37)

$$\begin{aligned} [\boldsymbol{M}(|\nabla\phi^{m+1}|) \quad + \quad & \Delta t \boldsymbol{L}(D|\nabla\phi^{m+1}|) - \Delta t \boldsymbol{K}(\mathbf{w}^m|\nabla\phi^{m+1}|) \\ - \quad & \Delta t \boldsymbol{N}(\boldsymbol{v}^{m+1}|\nabla\phi^{m+1}|)]\,\rho_h^{m+1} \\ = \quad & \boldsymbol{M}(|\nabla\phi^m|)\rho_h^m + \Delta t \boldsymbol{G}(|\nabla\phi^m|). \end{aligned} \tag{3.59}$$

- The implicit scheme with TVD stabilization (IS-TVD) corresponds to (3.57) where $F(\alpha)$ is of the TVD-type.
- The implicit scheme with FCT stabilization (IS-FCT) corresponds to (3.57) where $F(\alpha)$ is of the FCT-type.

The level set methodology and the algebraic nature of the flux-corrected schemes, TVD and FCT methods will be implemented for the equation (3.36) without further major changes (one should operate with proper $\boldsymbol{M}(\cdot)$, $\boldsymbol{L}(\cdot)$ and $\boldsymbol{K}(\cdot)$ matrices). Nevertheless, there are certain FCT schemes which necessitate the evaluation of ρ during the antidiffusive flux-limiting (3.57) e.g., *Gradient-based slope limiting* in [60]. In this case the corresponding projection onto the tangential space $T\Gamma$ is required. Numerical tests showed that the solution of the TVD scheme is less accurate as compared to that of FCT algorithm: neglecting the $(\boldsymbol{M}_L - \boldsymbol{M}(|\nabla\phi|))\dfrac{\rho_h^{m+1}-\rho_h^m}{\Delta t}$ term results in a smeared solution. Therefore, the FCT-based algorithms are preferable in this case.
Positivity constraints are enforced using a nonlinear blend of high- and low-order approximations through an algebraic manipulation of the matrices $\boldsymbol{M}$ and $\boldsymbol{K}$. The limiting strategy is fully multidimensional and applicable to (multi-)linear finite element discretizations on unstructured meshes. The approach was successfully tested for domain-defined equations for chemotaxis in 2- and 3-spatial dimensions, e.g., Sokolov et al. [113] and Strehl et al. [120] for chemotaxis equations which are defined on stationary surfaces. For detailed presentation of the FEM-FCT methodology, including theoretical study such as stability analysis, positivity preserving, mass conservation, convergence including technical implementation details like data structures, matrix assembly can be found in related publications, such as Kuzmin [60], Kuzmin and Turek [61], Möller et al. [76] and Strehl et al. [118, 120].

3.6 Surface triangulation

The most widely used numerical schemes for the approximation of partial differential equations are finite difference, finite volume and finite element methods. All these schemes use a triangulated geometry to approximate the numerical solution. The finite difference method approximate the solution by replacing the continuous PDEs with finite difference operators defined on triangulated mesh. Similarly, the finite element method is used to approximate solutions of the problems in variational forms [8]. The triangulation is used to transform continuous problem of the infinite dimensional space into an appropriate finite dimensional discrete form. Although we solve the discrete problem on a stationary mesh, to deal with complex geometries the solution can be approximated on a moving grids e.g., Budd et al. [10] and Huang and Russell [52].

Consider an open connected subset $\Gamma \subset \Omega$ in $\mathbb{R}^d$ for $d = 1,2,3$. The idea to cover the surface $\Gamma \subset \Omega$ with a finite number of sets of triangles/squares T_k of

simple shape. The domain $\Omega = \bigcup_{k=1}^{N} \mathscr{T}$, with $\mathscr{T} = \{T_k\}$. This decomposition will be used to transform the continuous partial differential equations from the integral form into its discrete sum. The surface triangulation used here, is based on an extensive work of Budd et al. [10], Dziuk and Elliott [26, 29, 30], Ranner [97] and Dziuk et al. [31]. The triangulation structure must fulfill the following basic criteria:

- $T_k \bigcap T_l = 0$ for $k \neq l$. The T_k are squares in this case.
- The domain is union of the all possible squares, i.e., $\Omega = \bigcup_{k=1}^{N} \mathscr{T}$.

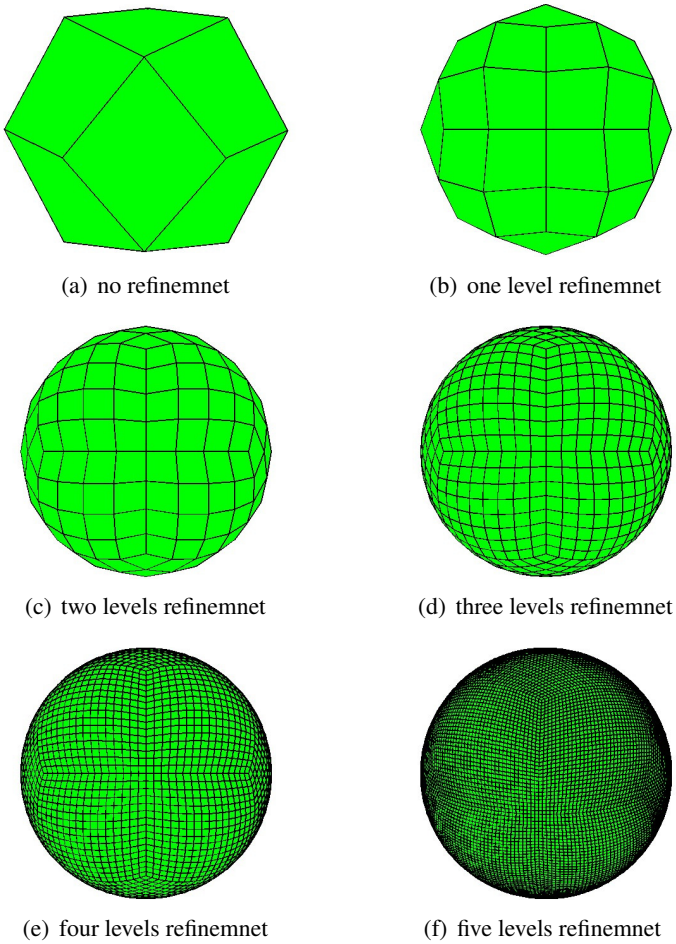

(a) no refinemnet (b) one level refinemnet

(c) two levels refinemnet (d) three levels refinemnet

(e) four levels refinemnet (f) five levels refinemnet

Figure 3.1: Three dimensional visualization of surface going through successive global refinement.

Thus without loss of generality, the sides of square are taken to be parallel

the coordinate axis. As T_k are squares and $\Gamma \subset \Omega$ is a polygon, such a configuration of the mesh on surface will be called triangulation, even in the case of the square/rectangle etc. The T_k are called elements, their sides the edge and the unknown values are calculated at the vertices known as mesh nodal values.

Now we are able to discuss the triangulation of the surface partial differential equations. In the process of triangulation and discretization the continuous surface Γ is replaced by its discrete counterpart, in most cases we replace it by piecewise polynomial surface Γ_h. This process may introduce a geometric error between Γ and Γ_h discussed in §3.7. In the earliest stage of triangulation we construct a polyhedral approximation of Γ with restriction on the nodes $\{T_j\}_{j=1}^{N}$ of Γ_h to lie on continuous surface Γ. In general there are different ways to construct triangulation, for instance by hand we can draw a coarse or macro sketch of triangulation. In this case, the elements could be large and may not be sufficient to capture the essential characteristics of surface. Particularly, Γ_h lie in the neighborhood U_ε, in results the triangulation process can be refined using some known strategies such as bisectional refinement or triangulation. To ensure that our new triangulation still satisfies basic assumptions on surface, thus all newly created nodes are projected onto the surface. The triangulation $\mathscr{T}_h$ of Γ_h are assumed to be closed d-simplices defined in $\mathbb{R}^{d+1}$, in particular can be line segments or polygonal curve $(d = 1)$, triangles or polyhedral $(d = 2)$ and tetrahedrons $(d = 3)$. Here h is defined to be maximum diameter of elements in $\mathscr{T}_h$ (e.g., see Dziuk and Elliott [29])

$$h := \max\{\operatorname{diam}(E) : E \in (\mathscr{T}_h)\}. \tag{3.60}$$

It is assumed that the triangulation $\mathscr{T}_h$ is a quasi-uniform triangulation, wherein Γ_h be a family of polyhedral approximation of surface Γ with $h > 0$ for each triangle $\mathscr{T}_h$. Then the family $\{\mathscr{T}_h\}$ is said to be quasi-triangulation then $\exists\ \beta_1 > 0$ such that

$$\min\{\operatorname{diam} B_E : E \in (\mathscr{T}_h)\} \geq \beta_1 h \ \operatorname{daim}\Gamma,$$

exists for all h where B_E is the largest ball contained in E [29]. Consequently, the triangulation $\mathscr{T}_h$ is said to be quasi-uniform triangulation Γ_h if it is part of quasi-uniform family of triangulated surface. As the nodes of Γ_h lie on Γ and the regularity of triangles $\mathscr{T}_h$ can be considered as an interpolent of Γ to estimate any geometric error [9, 29, 97]. The interpolated surface Γ_h is Lipschitz surface, in consequences we can define $H^1(\Gamma_h)$ with integration on Γ_h. Let ρ_h is the discrete counterpart of the continuous function ρ, reads as:

$$\rho_h : \Gamma_h \to \mathbb{R}.$$

The continuous gradient operator (2.98) of the function ρ, is defined by

$$\nabla_\Gamma \rho = \nabla\rho - (\nabla\rho \cdot \boldsymbol{n})\,\boldsymbol{n}.$$

Thus the element-wise discrete gradient operator is defined as

$$\nabla_{\Gamma_h}\rho_h := \nabla\tilde{\rho}_h - (\nabla\tilde{\rho}_h \cdot \boldsymbol{n}_h)\,\boldsymbol{n}_h. \tag{3.61}$$

For each $E \in \mathscr{T}_h$ with $\boldsymbol{n}$ defined along outward normal direction. The $\nabla\tilde{\rho}_h$ is any arbitrary extension of $\nabla\rho_h$ away from Γ_h. The projection operator defined in the continuous case (2.102)

$$\mathscr{P}_\Gamma(x) \quad = \quad (I - \boldsymbol{n} \otimes \boldsymbol{n}), \forall\, x \in \Gamma$$

can be replaced with the discrete counterpart:

$$\mathscr{P}_{\Gamma_h}(x) \quad := \quad (I - \boldsymbol{n}_h \otimes \boldsymbol{n}_h), \forall\, x \in \Gamma_h\,. \tag{3.62}$$

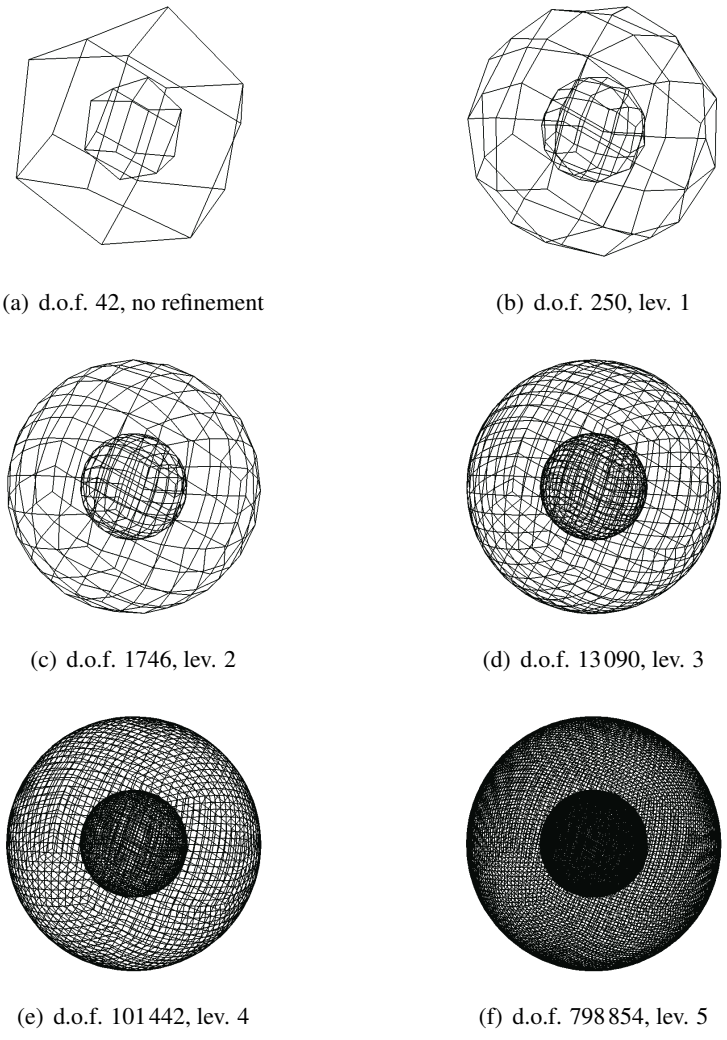

(a) d.o.f. 42, no refinement

(b) d.o.f. 250, lev. 1

(c) d.o.f. 1746, lev. 2

(d) d.o.f. 13 090, lev. 3

(e) d.o.f. 101 442, lev. 4

(f) d.o.f. 798 854, lev. 5

Figure 3.2: 3-D visualization of mesh with an increase in d.o.f. at successive refinement. Each square is split into four parts using a bisectional refinement.

The continuous piecewise finite element space on Γ_h will be replaced through

the surface finite element space denoted by S_h and defined as:

$$S_h := \{\phi_h \in C(\Gamma_h) : \phi_h|_E \in Q_1(E), \forall E \in \mathscr{T}_h\}. \tag{3.63}$$

The set of figures (3.1)–(3.2) are showing different levels of mesh refinement for the surface. At each refine level a square is partition into four different equal size squares. The figure 3.2(a) is showing mesh of the sphere without any refinement with 42 degrees of freedom. The figure 3.2(b) shows the first level of mesh refinement with d.o.f. 250. Similar, figures 3.2(c)–3.2(f) are representing grid refinement levels $2,3,4$ and 5 with 1746, 13090, 101442 and 798854, respectively, are the corresponding numbers of degrees of freedom.

3.7 Error analysis

In this section, we prove error bound for the numerical solution of the surface finite element method based on those of Dziuk and Elliott [26, 29, 30], Ranner [97] and Dziuk et al. [31]. In addition, we formulate the error between the solution of the continuous space and its discrete counterpart. We start with the basic definition of the L^p-space and corresponding norms.

Definition 6. *The (L^p-space)*
Let $L^p(\Gamma)$ denote the space of measurable function with respect to the d-dimensional Hausdorff measure (surface measure dA) the space of measurable functions are defined with a finite norm $\|\rho\|_{L^p(\Gamma)}$ where the L^p-norm is defined by

$$\|\rho\|_{L^p(\Gamma)} = \left(\int_\Gamma |\rho|^p dA\right)^{\frac{1}{p}} \tag{3.64}$$

for $p < \infty$ the $L^p(\Gamma)$ is a Banach space. Now we can extract the following results.

Remark 13. *From equation (3.64) we deduce the following useful remarks.*

- *for $p = 2$ a Hilbert space. Roughly speaking, L^2 is the space of square integrable functions.*
- *In the interval $1 < p < \infty$ the spaces $C^0(\Gamma)$ and $C^1(\Gamma)$ are dense in $L^p(\Gamma)$.*
- *For $p = \infty$ in (3.64) means the essential supremum norm.*

Now we will define the $H^1(\Omega)$ space and corresponding norm for the approximate solution.

Definition 7. *The $H^1(\Omega)$-space The Sobolev space of order 1 on Ω the space $H^1(\Omega)$ is defined in [30] by*

$$H^1(\Omega) = \{\rho \in L^2(\Omega), \quad \nabla\rho \in L^2(\Omega)\}.$$

The space $H^1(\Omega)$ is endowed with the norm defined by the inner product

$$\langle \rho, c \rangle_{1,\Omega} = \int_\Omega \left(\rho c + \sum_{i=1}^{d} \partial_i \rho \, \partial_i c \right) d\Omega$$

and the corresponding norm is noted as:

$$\|\rho\|_{1,\Omega} = \sqrt{\langle \rho, \rho \rangle_{1,\Omega}} = \left(\int_\Omega |\rho|^2 dx + \int_\Omega |\nabla \rho|^2 d\Omega \right)^{1/2}.$$

Lemma 3.7.1. *There exists a unique solution ρ_h to the problem (3.23) that satisfies the following bound*

$$\|\rho_h\|_{H^1(\Gamma_h)} \leq c \|f\|_{L^2(\Gamma)}. \tag{3.65}$$

This lemma is similar to that of (3.4.1) and it is essential for the well-posedness of solution.

We can define the discrete bilinear and linear forms, in the following way:

$$a_h(\cdot,\cdot) : S_h \times S_h \to \mathbb{R}$$

$$l_h(\cdot) : S_h \to \mathbb{R}$$

using these relations we have the discrete forms:

$$a_h(\rho_h, \varphi_h) := \int_{\Gamma_h} \nabla_{\Gamma_h} \rho_h \cdot \nabla_{\Gamma_h} \varphi_h + c \rho_h \varphi_h d\Gamma_h, \tag{3.66}$$

$$l_h(\varphi_h) := \int_{\Gamma_h} f \varphi_h d\Gamma_h. \tag{3.67}$$

This formulation leads to the following form of (3.23), find $\rho_h \in S_h$ such that

$$a_h(\rho_h, \varphi_h) = l(\varphi) \quad \text{for all} \quad \rho_h \in S_h. \tag{3.68}$$

Lemma 3.7.2. *(Strang Lemma)*
Let $V_h \subset V$ and $a(\cdot,\cdot)$ is bilinear form on $V \times V$ and $l(\cdot)$ linear form on V. Furthermore, let $a_h(\cdot,\cdot)$ is bilinear form $V_h \times V_h$ and linear forms $l_h(\cdot)$ in V_h, defined in (3.66) and (3.67), respectively. Assuming that each pair satisfies the Lax-Milgram theorem. In addition, suppose that $\rho \in V$ and $\rho_h \in V_h$ satisfy (3.18) and (3.68), respectively. We will define a norm $\|\cdot\|_a$ induced by the bilinear form $a(\cdot,\cdot)$ as follows

$$\|\rho\|_a := a(\rho,\rho)^{\frac{1}{2}} \quad \textit{for} \quad \rho \in V.$$

Define $F_h : V_h \to \mathbb{R}$ by

$$F_h(\varphi_h) := a(\rho - \rho_h, \varphi), \tag{3.69}$$

then

$$\|\rho - \rho_h\|_a \leq 2 \inf_{v_h \in V_h} \|\rho - v_h\|_a + \sup_{w_h \in V_h \setminus \{0\}} \frac{F_h(w_h)}{\|w_h\|_a}. \tag{3.70}$$

Proof. Let for any $v_h \in V_h$,

$$\begin{aligned}
\|\rho - \rho_h\|_a &\leq \|\rho - v_h\|_a + \|v_h - \rho_h\|_a \\
&\leq \|\rho - v_h\|_a + a(v_h - \rho_h, v_h - w_h)^{\frac{1}{2}} \\
&\leq \|\rho - v_h\|_a + \sup_{w_h \in V_h \setminus \{0\}} \frac{a(v_h - \rho_h, w_h)}{\|w_h\|_a} \\
&\leq 2\|\rho - v_h\|_a + \sup_{w_h \in V_h \setminus \{0\}} \frac{a(\rho - \rho_h, w_h)}{\|w_h\|_a}
\end{aligned}$$

□

Assume that we have a Hilbert space $(H, \langle \cdot, \cdot \rangle)$ and a Banach space $(Z, \|\cdot\|_Z)$ with $Z \subset V \subset H$ with continuous inclusion. This implies that for $\eta \in H$ the functional is defined as:

$$\mathscr{X}_\eta(\varphi) = \langle \eta, \varphi \rangle_H,$$

is a bounded linear functional on V with

$$|\mathscr{X}_\eta(\varphi)| \leq \|\eta\|_H \, \|\varphi\|_H \leq c\|\eta\|_H \|\varphi\|_V.$$

Hence, there exists a unique solution $z \in V$ of

$$a(\varphi, z) = \mathscr{X}_\eta(\varphi) \quad \text{for all} \quad \varphi \in V. \tag{3.71}$$

Assume that the solution $z \in Z$ satisfies the bound

$$\|z\|_Z \leq c\|\eta\|_H. \tag{3.72}$$

Moreover, we assume that for all $v \in Z$ there exist $v_h^* \in V_h$ satisfying

$$\|v - v_h^*\|_a \leq ch\|v\|_Z. \tag{3.73}$$

Lemma 3.7.3. *(Aubin-Nitsche Lemma)*
Let the above assumptions (3.71)–(3.73) hold and suppose $e \in V$. Define $F_h : V_h \to \mathbb{R}$ by

$$F_h(\varphi_h) = a(e, \varphi_h), \tag{3.74}$$

then

$$\|e\|_H \leq ch\|e\|_a + \sup_{\varphi_h \in V_h \setminus \{0\}} \frac{F_h(\varphi_h)}{\|\varphi_h\|_a}. \tag{3.75}$$

Proof. Since $e \in V \subset H$, from the assumptions (3.71) and (3.72) there exist a unique $z \in Z$ such that

$$a(\varphi, z) = \mathscr{X}_e(\varphi) \quad \text{for all} \quad \varphi \in V,$$

and

$$\|z\|_Z \leq c\|e\|_H.$$

Using assumption (3.73), we know there exists $z_h^* \in V_h$ with

$$\|z - z_h^*\| \leq ch\|z\|_Z.$$

We calculate,

$$\begin{aligned}
\|e\|_H^2 &= \langle e, e\rangle_H, \\
&= a(e,z), \\
&= a(e, z - z_h^*) + a(e, z_h^*), \\
&\leq \left(ch\|e\|_a + \sup_{\varphi_h \in V_h \setminus \{0\}} \frac{a(e,\varphi_h)}{\|\varphi_h\|_a} \right) \|z\|_Z, \\
&\leq \left(ch\|e\|_a + \sup_{\varphi_h \in V_h \setminus \{0\}} \frac{a(e,\varphi_h)}{\|\varphi_h\|_a} \right) \|e\|_H.
\end{aligned}$$

or

$$\|e\|_H \left(\|e\|_H - \left(ch\|e\|_a + \sup_{\varphi_h \in V_h \setminus \{0\}} \frac{a(e,\varphi_h)}{\|\varphi_h\|_a} \right) \right) \leq 0,$$

since $\|e\|_H \geq 0$, we have

$$\|e\|_H \leq ch\|e\|_a + \sup_{\varphi_h \in V_h \setminus \{0\}} \frac{a(e,\varphi_h)}{\|\varphi_h\|_a},$$

hence the required result. □

Lemma 3.7.4. *Let $z \in H^2(\Gamma)$ and consider that the lift of the nodal interpolate of z is $I_h z \in S_h^l$ is a well defined function in S_h^l satisfies the following bound:*

$$\|z - I_h z\|_{H^1(\Gamma)} \leq ch\|z\|_H^2(\Gamma). \tag{3.76}$$

Proof. The proof of this approximation property can be found in [27, 97]. □

Lemma 3.7.5. *Let $W_h, \Phi_h \in S_h$ with lift $w_h, \varphi_h \in S_h^l$, then the following geometric bound holds:*

$$\|a(w_h, \varphi) - a_h(W_h, \Phi_h)\| \leq ch^2 \|\nabla_\Gamma w_h\|_L^2(\Gamma) \|\nabla_\Gamma \varphi_h\|_L^2(\Gamma). \tag{3.77}$$

Proof. This lemma in known as geometric bound, proof can be found in [27, 97]. □

Lemma 3.7.6. *Let $\eta \in H^1(\Gamma)$ and $\mathscr{B}_h \subset \Omega$, we have*

$$\|\eta\|_{L^2(\mathscr{B}_h)} \leq ch^{1/2}\|\eta\|_H^1(\Omega). \tag{3.78}$$

Theorem 3.7.7. *Let $\rho \in H^2(\Gamma)$ be the solution (3.13) and let $\rho_h \in S_h$ be the solution of (3.23). Assume that the result of approximation property (3.76) holds. Then we have the following estimate defined in [97],*

$$\|\rho - \rho_h\|_{L^2(\Gamma)} + h\|\nabla_\Gamma(\rho - \rho_h)\|_{L^2(\Gamma)} \leq ch^2\|f\|_{L^2(\Gamma)}. \tag{3.79}$$

Proof. Let us consider the space $V = H^1(\Gamma)$ and the finite element space $V_h = S_h^l$. The notations for the continuous form of the problem (3.66) and (3.67) fit exactly for bilinear form $a(\cdot,\cdot)$ and the linear form $l(\cdot)$, respectively. Consequently, we have the following results

$$a_h(w_h, \varphi_h) := \int_{\Gamma_h} \nabla_{\Gamma_h} W_h \cdot \nabla_{\Gamma_h} \varphi_h + W_h \varphi_h d\Gamma_h,$$

$$l_h(\varphi_h) := \int_{\Gamma_h} f\varphi_h d\Gamma_h,$$

with $w_h = W_h^l$ and $\varphi_h = \varphi_h^l$.

For $F_h(\varphi_h) = a(\rho - \rho_h, \varphi_h)$ using the well-posed bound for stability from lemma (3.7.1) together with the geometric bounds (3.7.5).

$$\begin{aligned} F_h(\varphi_h) &= a(\rho - \rho_h, \varphi_h) = l(\varphi_h) - a(\rho_h, \varphi_h), \\ &= (l(\varphi) - l_h(\Phi_h)) + (a_h(\rho_h, \Phi_h) - a(\rho_h, \varphi_h)), \\ &\leq ch^2\|f\|_L^2\|\varphi_h\|_{H^1(\Gamma)} + ch^2\|\rho_h\|_{H^1(\Gamma)}\|\varphi_h\|_{H^1(\Gamma)}. \\ &\leq ch^2\|f\|_L^2\|\varphi_h\|_{H^1(\Gamma)}. \end{aligned} \tag{3.80}$$

The Strang Lemma §3.7.3 gives

$$\|\rho - \rho_h\|_{H^1(\Gamma)} \leq c \inf_{v_h \in S_h^l} \|\rho - v_h\|_{H^1(\Gamma)} + c \sup_{w_h \in V_h \setminus \{0\}} \frac{F_h(w_h)}{\|w_h\|_{H^1(\Gamma)}}.$$

The first term is known as approximation error, which is bounded via approximation property lemma §3.7.4 gives

$$\inf_{v_h \in S_h^l} \|\rho - v_h\|_{H^1(\Gamma)} \leq \|\rho - I_h\rho\|_{H^1(\Gamma)} \leq ch\|\rho\|_{H^2(\Gamma)} \leq ch\|f\|_{L^2(\Gamma)}. \tag{3.81}$$

Bringing together (3.80) and (3.81), we get the following approximation error:

$$\|\rho - \rho_h\|_{H^1(\Gamma)} \leq ch\|f\|_{H^1(\Gamma)}. \tag{3.82}$$

To find the L^2 estimates we use the abstract Aubin-Nitsche lemma with $H = L^2(\Gamma)$ and $Z = H^2(\Gamma)$. The regularity results in lemma §3.4.1 leads to the dual regularity

and the approximation property of §3.7.4 gives the equation (3.73). Substituting $e = \rho - \rho_h$, we get

$$\|\rho - \rho_h\|_{L^2(\Gamma)} \leq ch\|\rho - \rho_h\|_{H^1(\Gamma)} + \sup_{\varphi_h \in V_h \setminus \{0\}} \frac{F_h(\varphi_h)}{\|\varphi_h\|_{H^1(\Gamma)}}. \tag{3.83}$$

The first term in (3.83) is bounded using the H^1-norm bound defined in equation (3.82):

$$ch\|\rho - \rho_h\|_{H^1(\Gamma)} \leq \|f\|_{L^2(\Gamma)}. \tag{3.84}$$

Using (3.84) and (3.80) we get the following result:

$$\|\rho - \rho_h\|_{L^2(\Gamma)} \leq ch^2\|f\|_{L^2(\Gamma)}. \tag{3.85}$$

Which concludes the proof of an important theorem for the numerical calculation. These error estimates will be conformed using the numerical results. □

3.8 Conclusion

In this chapter, we investigated the generic model for surface PDEs, based on these discretizations in the later chapters we can deduce the reaction-diffusion equations for pattern forming models and reaction-diffusion-advection for chemotaxis like PDEs. We discussed thoroughly the applicability of the spatial and temporal discretization for these models. The FEM level set based discretization of the Laplace-Beltrami operator has been addressed. The variational formulations for the model equations are derived as well, including the boundary integral in the discretized model. We developed the basic algorithm for the algebraic flux correction technique of FCT and TVD-types, in order to avoid non-physical solutions, which occurs due to inclusion of boundary integral, surface convection and/or chemotaxis, The surface triangulation is shown with number of degrees of freedom at different mesh level. We concluded the chapter with deriving an important formulae on a priori error analysis. The theoretical results derived here are part and parcel for the justification to the assumptions we make on the continuous model in order to obtain the numerical approximation. In conclusion, in this chapter we proposed a fully implicit finite element method level set based numerical scheme for systems of reaction-diffusion-convection/chemotaxis equations on an evolving-in-time surface. The scheme is positivity preserving, which is guaranteed through the inclusion of the FCT and TVD stabilization technique. Based on the derived scheme, in the next chapter, the behavior of the numerical solution will be explored.

Part II

Numerical results and outlook

Nothing in biology makes sense except in the light of evolution.

Theodosius Dodzhansky

4 Numerical results

In this chapter, we highlight the software setup and present the results of numerical experiments which are obtained through a variant of test examples for the surface PDEs. The spatial and temporal discretization schemes including stabilized finite element method with necessary formulations will be used directly from the *Chapter 3*. The numerical evidence presents the efficiency and accuracy of the developed schemes. Some of these results appeared in a research article [114]. [1].

4.1 Introduction

We have established the theory of an algebraic flux-corrected finite element level set based scheme for solution of a class of partial differential equations on stationary and evolving-in-time surfaces. The proposed numerical scheme is positivity preserving. Now we will propose and analyze our numerical method to approximate the solution of PDEs on surface.

In general, the modeling of a physical phenomena with biological applications are complex and highly nonlinear partial differential equations. There is no systematic way to find an exact analytic solution for such kind of PDEs. Therefore, we look for a computational or numerical approximation of the solution. The numerical approximation can be constructed after discretization of the continuous model into its discrete counterpart. Then the resulting discrete equations can be solved computationally.

A large class of numerical methods are proposed for approximation of the geometric partial differential equations. In this chapter we will use conforming bilinear and trilinear finite elements, based on the constructed scheme in Chapter (3).

4.1.1 Software and implementation

The numerical simulations are implemented using Finite Element Analysis Tool FEATFLOW for flow problems. It is an open source multipurpose software package. The proposed numerical scheme are implemented in the open source FEM-library

[1] A. Sokolov, R. Ali, S. Turek, An AFC-stabilized implicit finite element method for partial differential equations on evolving-in-time surfaces, J. Comput. Appl. Math. 289, 101-115

FEATFLOW, which is developed and maintained at the department of applied mathematics at TU Dortmund. The downloading of the software and the corresponding applications is possible to find in FEATFLOW web page [2].

The FEATFLOW library is build up on the FORTRAN77 and FORTRAN90, mainly focusing on unstructured quadrilateral and hexahedral meshes applicable to 2-D and 3-D problems, respectively. The FEATFLOW uses nonconforming parametric/nonparametric finite element method with rotated bi/tri-linear shape functions for spatial discretization. The temporal discretization, e.g., see §3.2 are implemented with a variant of θ-schemes, namely, explicit schemes such as Forward-Euler and implicit-schemes like backward-Euler, Crank-Nicholson, fractional step θ-schemes, modified step θ-schemes and more depending mainly on the nature of the problems. This work has been implemented using the fully implicit θ-schemes for temporal discretization. In the numerical process, the continuous model is transformed into its discrete counterpart using spatio-temporal discretization, which can be solved through direct or indirect solvers. The BIO-APP (biological applications) solver provide implementation of problem through iterative algorithm and preconditioners can be chosen from Krylov space techniques such as conjugate gradient method (CG), biconjugate gradient method (BCG), biconjugate gradient stabilized method, generalized minimal residual method (GMRES) and etc.

The applications of FEATFLOW library include, just to name few, chemotaxis related problem [113, 117–120], level set method Turek et al. [128], fluid-structure interaction [102, 126, 127], hemodynamics [101, 134], Lattice Boltzmann technique, least square method, multi-phase flow, fictitious boundary method. The software library is in a constant evolution, capable to solve compressible and/or incompressible flow of Newtonian and non-Newtonian fluid models with magneto-hydrodynamics, heat/mass transfer, with optional hardware oriented advance parallel programming.

The numerical simulations are implemented in BIO-APP section of FEAT library. This application is capable to solve a wide variety of biological problems, such as chemotaxis, patterns forming models in two and three dimensional geometry. The application provide efficient, flexible and positivity preserving schemes for PDEs on stationary and evolving surfaces [113–115, 117–120]. The proposed framework is further extended it the an algebraic flux-corrected FEM level set based scheme to solve partial differential equations on stationary and evolving surfaces.

The meshes for the physical domains and surface triangulation are generated mainly through Grid DEVISOR (Design and Visualization Software Resource)[3]. The visualization of the graphical results are performed with GMV (General Mesh Viewer)[4] and ParaView[5].

[2] http://www.featflow.de
[3] http://www.feast.uni-dortmund.de/downloads.html
[4] http://www.generalmeshviewer.com
[5] http://www.paraview.org

4.2 Numerical experiments

This section aims to describe the numerical setup with visualization and numerical computation of the discretized scheme. The problem in hand is visualized through mesh generation of geometry. The numerical results will provide the solution profiles and the order of convergence for the proposed numerical schemes.

4.2.1 Visualization and computation

We are using the partial differential equations to describe physical phenomena on surface. As we mentioned earlier, the analytic solution for such models are often complicated to achieve, sometimes it is challenging to build up a numerical scheme to capture the solution behavior. To get the numerical insight for governing equations through a geometrical view, we solve the discretized problem on a given surface geometry represented by mesh. The mesh generation is comparatively easy for the domain of rectangular/square shape and even more challenging for 3-D geometry with curvalinear boundaries. The represented mesh can be structured/unstructured and block-structured depending on complexity of the physical problem.

Based on triangulation in §3.6, the unknowns (d.o.f) of the discrete problems are associated with a computational grid/mesh, which comprises number of subdomains of the whole domain. These sub-domains are intervals in 1-D, triangles or quadrilaterals in 2-D and tetrahedral or hexahedrals in 3-D geometries.

The discrete solution is initially defined on a mesh, using this initial profile at each time step a new solution is obtained, then the solution is interpolated for the next step. The newly generated solution may contains different number of nodes as compared to previous mesh.

In the numerical community, three grid adaptation are commonly used, depending on the prescription of nodes for a fixed and/or moving grid/mesh. Generally, the numerical algorithm can be categorized into Eulerian, Lagrangian and arbitrary Eulerian-Lagrangian (ALE) techniques. The most common refinement is h-refinement, where a static mesh use and also capable to add/remove nodes from the existing mesh. The second refinement is p-refinement, where a local polynomial is employed for the finite element discretization of partial differential equation. The order of the polynomial is increased and/or decreased to adapt the method w.r.t. smoothness of the solution. The combination of both refinement is known as the hp-refinement. However, the hp-refinement may be complex and challenging to get desire solution. For example, the calculation of error estimates, which heavily rely on certain assumptions. Thus there are variety of refinement techniques exist, we use an Eulerian approach. The theoretical and practical aspects of the Eulerian surface defined partial differential equations, are studied by Dziuk and Elliott [26, 29, 30] and [31, 97]. Another approach can be the moving mesh, which posses greater values and applications, interested readers are kindly refer to Budd et al. [10] and Huang and Russell [52].

4.2.2 Laplace-Beltrami on evolving surface

Here to solve numerical examples corresponding to surface PDEs with different configurations. We use the already constructed scheme of spatial discretization by finite element method §3.3 including temporal discretization §3.2. For instance, we solve partial differential equation on surface around a narrow band using FEM-level set based method with pure Galerkin (without further modification in the constructed matrices), AFC methods §3.5.1 of flux-corrected transport (FCT) and total variation diminishing (TVD) schemes.
Consider reaction-diffusion equations on an evolving surface:

$$\frac{\partial^* \rho}{\partial t} + \alpha\rho = D\Delta_{\Gamma(t)}\rho \qquad \text{on} \quad \Gamma(t). \tag{4.1}$$

Where $\alpha\rho$ is reactive kinetic. We observe that in this particular example α does not influence the physical significance, thus we may assume $\alpha = 0$. Furthermore, we use different values of α in rest of our study, keeping in view the importance of reactive kinetics in biological applications of pattern formations. On right hand side of equation (4.1), we have Laplace-Beltrami operator (see §2.2.4) and diffusion coefficient D. The first term on left hand side of equation(4.1) is surface material derivative defined as:

$$\frac{\partial^* \rho}{\partial t} = \partial_t^\bullet \rho + \rho \nabla_{\Gamma(t)} \cdot \boldsymbol{v}, \tag{4.2}$$

here $\partial_t^\bullet \rho$ is given as:

$$\partial_t^\bullet \rho = \frac{\partial \rho}{\partial t} + \boldsymbol{v} \cdot \nabla \rho. \tag{4.3}$$

Using the Leibniz formula from lemma:2.3.3

$$\frac{d}{dt}\int_\Gamma \rho = \int_\Gamma \left(\partial_t^\bullet \rho + \rho \nabla_\Gamma \cdot \boldsymbol{v}\right), \tag{4.4}$$

after employing equations (4.2), (4.3) and (4.4), we can obtain the following simplified equation on surface.

$$\frac{\partial \rho}{\partial t} + \boldsymbol{v} \cdot \nabla \rho + \rho \nabla_\Gamma \cdot \boldsymbol{v} + \alpha\rho = D\Delta_{\Gamma(t)}\rho \quad \text{on} \quad \Gamma(t). \tag{4.5}$$

As we use the level set methods to capture evolution of surface, for details description and formulation of level set methodology we kindly refer to §2.4.
Consider the following initial prescription of the level set function:

$$\phi(\mathbf{x},t) = |\mathbf{x}| - (1.0 + bt\,\sin(5\Theta)),$$

here b is an arbitrary constant, in this example we choose $b = 10$, t is time variable and the angle Θ is define as:

$$\Theta = atan2(x^2, x^1).$$

where the definition of $atan2(x^2,x^1)$ stated as follows:

$$atan2(x^2,x^1) = \begin{cases} \arctan\left(\frac{x^2}{x^1}\right) & \text{if} \quad x^1 > 0, \\ \arctan\left(\frac{x^2}{x^1}\right) + \pi & \text{if} \quad x^2 \geq 0 \quad \text{and} \quad x^1 < 0, \\ \arctan\left(\frac{x^2}{x^1}\right) - \pi & \text{if} \quad x^2 < 0 \quad \text{and} \quad x^1 < 0, \\ +\frac{\pi}{2} & \text{if} \quad x^2 > 0 \quad \text{and} \quad x^1 = 0. \end{cases} \tag{4.6}$$

and the initial condition $\rho(t=0) = \rho_0$,

$$\rho_0 = \begin{cases} 10 & \text{if } |\mathbf{x} - (0,1)^T| = 0\ , \\ 0 & \text{otherwise.} \end{cases} \tag{4.7}$$

The assumed computational domain is

$$\Omega = \{\mathbf{x} \in \mathbb{R}^2 : 0.5 \leq |\mathbf{x}| \leq 1.5\}. \tag{4.8}$$

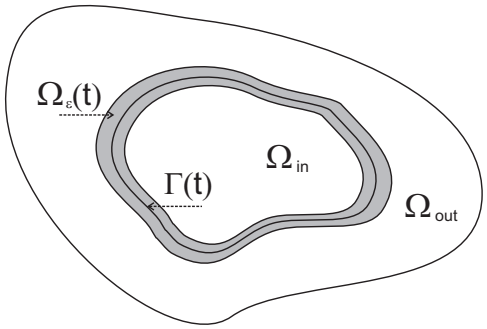

Figure 4.1: Geometric illustration of the computational domain $\Omega = \Omega_{in} \cup \Omega_{out} \cup \Gamma$

To get more insight to see the oscillations on the solution profile we will reduce the domain (e.g., see fig. 4.2.2) four-fold and denote it by ε. The figures 4.2(a)–4.2(d) show the evolution of the level set function $\phi(\mathbf{x},t)$ at different time instances. Figure 4.2(a) shows the initial prescription of the level set function. Figures 4.2(b), 4.2(c) and 4.2(d) are calculated at $t = 0.01, 0.02$ and 0.05, respectively. It is worth noting that the level set function $\phi(\mathbf{x},t)$ evolves in a regularized manner, applications of evolving level set in image processing are presented by Chunming et al. [20].

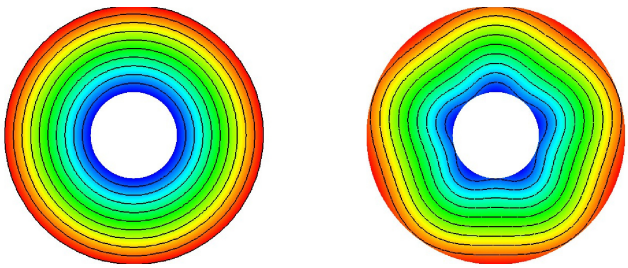

(a) level set, $t = 0.00$ (b) level set, $t = 0.01$

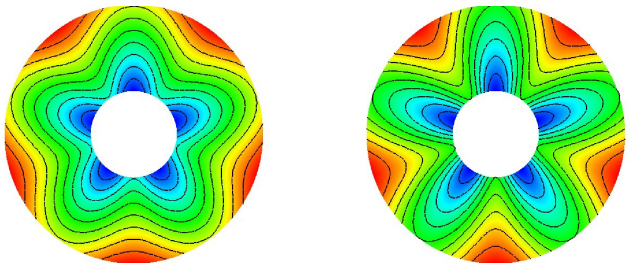

(c) level set, $t = 0.02$ (d) level set, $t = 0.05$

Figure 4.2: The evolution of the level set function $\phi(\mathbf{x},t)$ (a) initial value (b) ϕ at 0.01 (c) ϕ at (0.01) and (d) ϕ at 0.05 The colour stands for values of ρ between maximum (red) and minimum (blue).

Figure 4.3(a) shows the initial solution, from left to right in the rows we have an increase in the diffusion coefficients $D = 10^{-5}, 10^{-2}, 1.0$, respectively. Similarly in the column we have the levels of mesh refinement, i.e., $level = 3,...,8$, respectively. We did not include the solution profiles at certain levels, either they do not possess physical significance in this study or to avoid redundancy of results. A similar procedure is used in case of algebraic flux correction of FCT/TVD-type to approximate solutions.

Figures 4.3(b)–4.3(m) show the results obtained through standard Galerkin scheme (SG). It can be observed that for level 5 (which corresponds to 16640 d.o.f) we get kinks at solution profile even with a comparatively high diffusion coefficients. Furthermore, in some cases such a high diffusion are inappropriate for certain physical models. If we increase the level of refinements from 3 to 8, consequently the quality of the solution improve. But in results the computational costs of the numerical solution will increase exponentially. We noticed that even at 8th-level of refinement using a small diffusion coefficient we get oscillations in the solution close to steep gradient. Numerical oscillations in the solution profile of the Galerkin scheme with different experiments are clearly shown. In consequences, this system of partial differential equations on surface requires an alternative accurate and efficient technique to get solutions with low computational cost in a reasonable time frame.

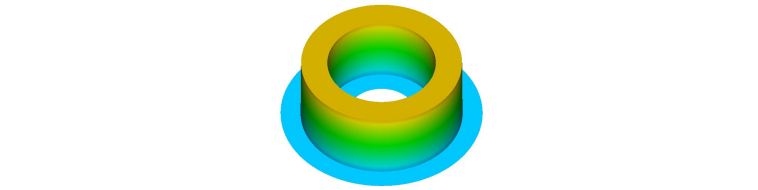

(a) initial solution

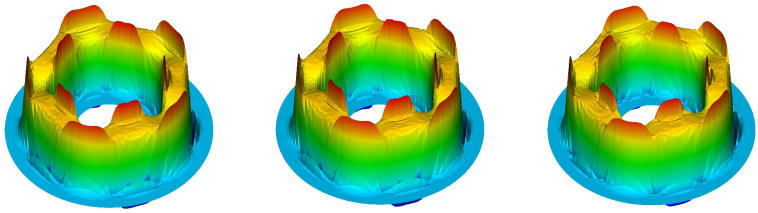

(b) lev. 4, D= 10^{-5} (c) lev. 4, D= 10^{-2} (d) lev. 4, D = 1.0

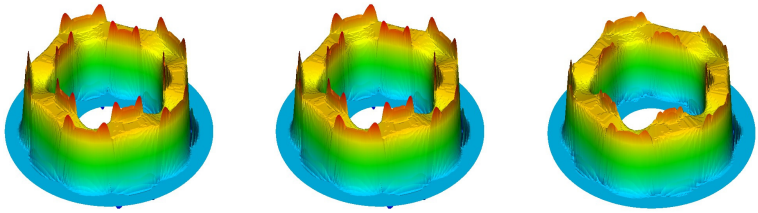

(e) lev. 5, D= 10^{-5} (f) lev. 5, D= 10^{-2} (g) lev. 5, D= 1.0

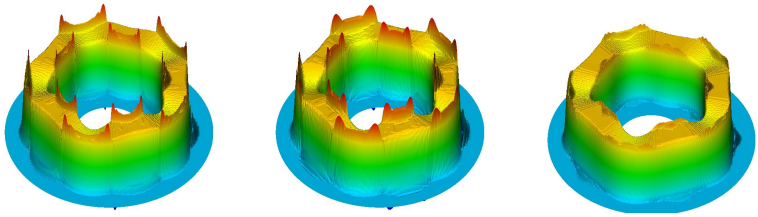

(h) lev. 6, D= 10^{-5} (i) lev. 6, D= 10^{-2} (j) lev. 6, D= 1.0

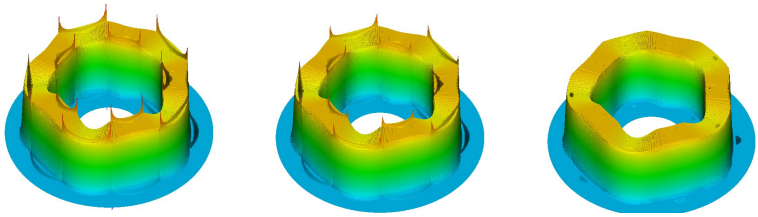

(k) lev. 8, D= 10^{-5} (l) lev. 8, D= 10^{-2} (m) lev. 8, D= 1.0

Figure 4.3: The pure Galerkin method, $\alpha = 0.0$, at $T = 0.05$ with fixed time step $\Delta t = 0.0005$, left to right an increase in diffusion coefficient and top to bottom an increase in mesh refinement levels. The light blue represents the value of $\rho = -0.85$ and red $\rho = 0.85$

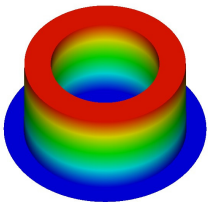

(a) initial solution

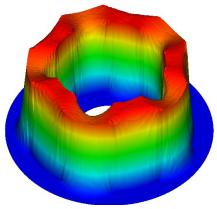

(b) lev. 4, D= 10^{-5}

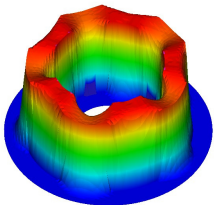

(c) lev. 4, D= 10^{-2}

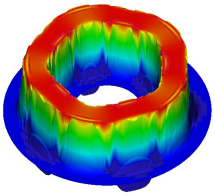

(d) lev. 4, D= 1.0

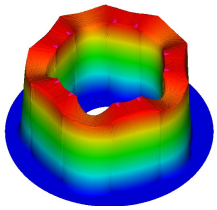

(e) lev. 6, D= 10^{-5}

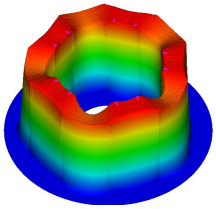

(f) lev. 6, D= 10^{-2}

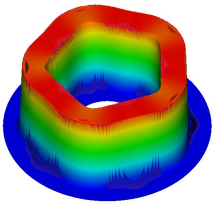

(g) lev. 6, D= 1.0

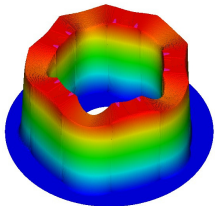

(h) lev. 7, D= 10^{-5}

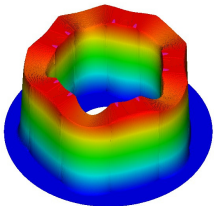

(i) lev. 7, D= 10^{-2}

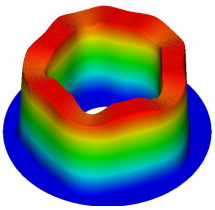

(j) lev. 7, D= 1.0

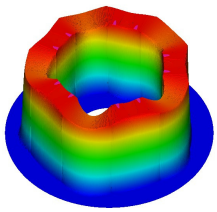

(k) lev. 8, D= 10^{-5}

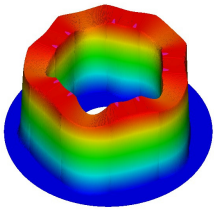

(l) lev. 8, D= 10^{-2}

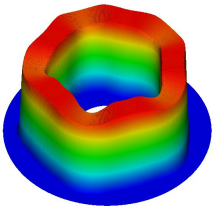

(m) lev. 8, D= 1.0

Figure 4.4: The TVD scheme, at $T = 0.05$ with fixed time step $\Delta t = 0.0005$, left to right an increase in diffusion coefficient and top to bottom an increase in mesh refinement levels. Blue represents the value of $\rho = -1.0$ and red $\rho = 1.0$

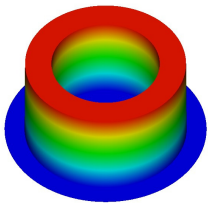

(a) initial solution

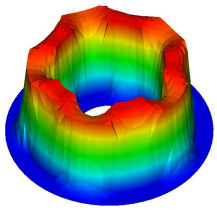

(b) lev. 3, D= 10^{-5}

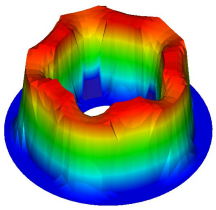

(c) lev. 3, D= 10^{-2}

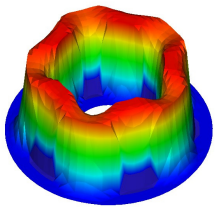

(d) lev. 3, D= 1.0

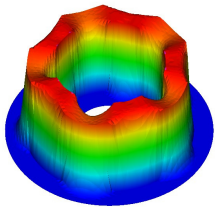

(e) lev. 4, D= 10^{-5}

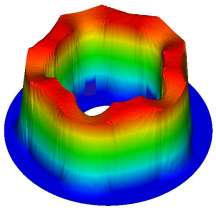

(f) lev. 4, D= 10^{-2}

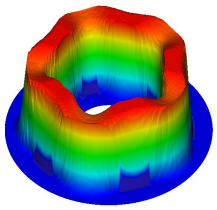

(g) lev. 4, D= 1.0

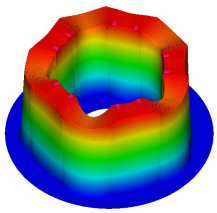

(h) lev. 7, D= 10^{-5}

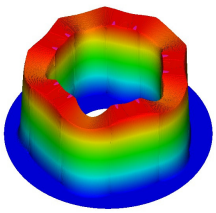

(i) lev. 7, D= 10^{-2}

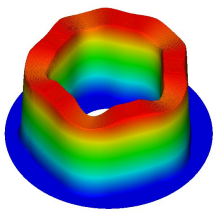

(j) lev. 7, D= 1.0

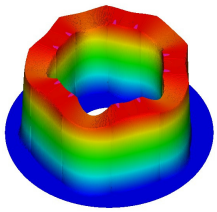

(k) lev. 8, D= 10^{-5}

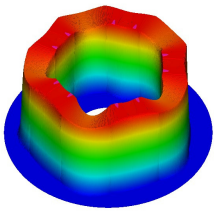

(l) lev. 8, D= 10^{-2}

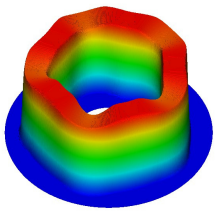

(m) lev. 8, D= 1.0

Figure 4.5: The FCT scheme, at $T = 0.05$ with fixed time step $\Delta t = 0.0005$, left to right an increase in diffusion coefficient and top to bottom an increase in mesh refinement levels. Blue represents the value of $\rho = -1.0$ and red $\rho = 1.0$

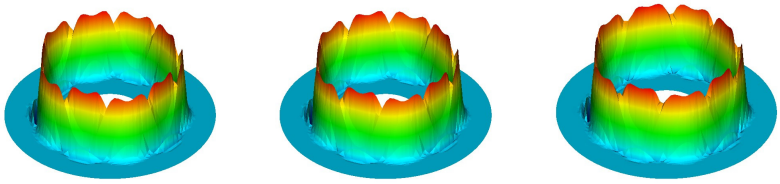

(a) lev. 4, D= 10^{-5} (b) lev. 4, D= 10^{-2} (c) lev. 4, D = 1.0

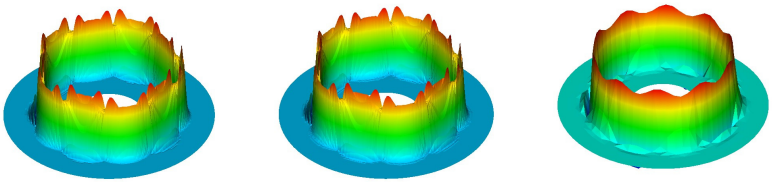

(d) lev. 5, D= 10^{-5} (e) lev. 5, D= 10^{-2} (f) lev. 5, D= 1.0

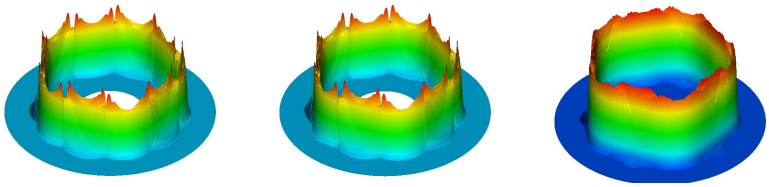

(g) lev. 6, D= 10^{-5} (h) lev. 6, D= 10^{-2} (i) lev. 6, D= 1.0

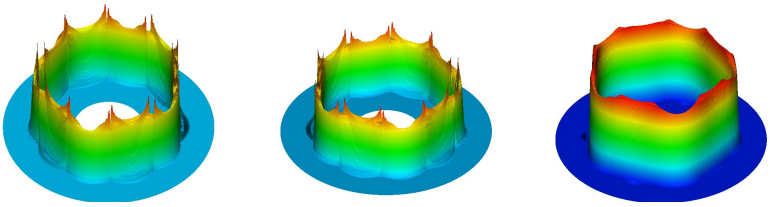

(j) lev. 7, D= 10^{-5} (k) lev. 7, D= 10^{-2} (l) lev. 7, D= 1.0

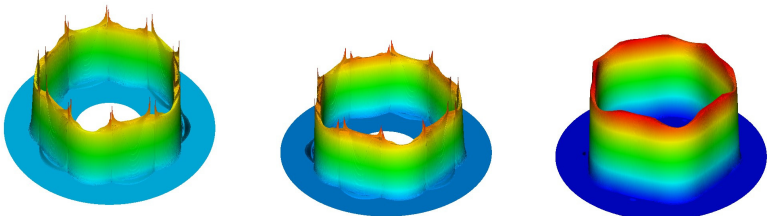

(m) lev. 8, D= 10^{-5} (n) lev. 8, D= 10^{-2} (o) lev. 8, D= 1.0

Figure 4.6: The pure Galerkin method, $\varepsilon = 0.125$, $\alpha = 0.0$, at $T = 0.05$ with fixed time step $\Delta t = 0.0005$, left to right an increase in diffusion coefficient and top to bottom an increase in mesh refinement levels. Blue represents the value of $\rho = -1.0$ and red $\rho = 1.0$

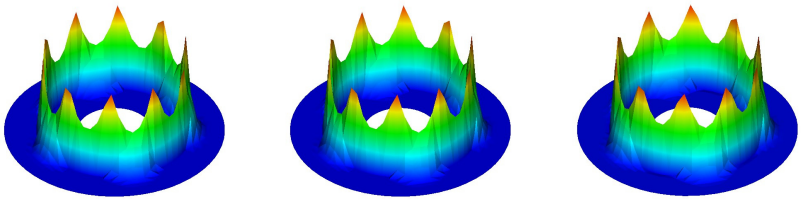

(a) lev. 3, D= 10^{-5} (b) lev. 3, D = 10^{-2} (c) lev. 3, D= 1.0

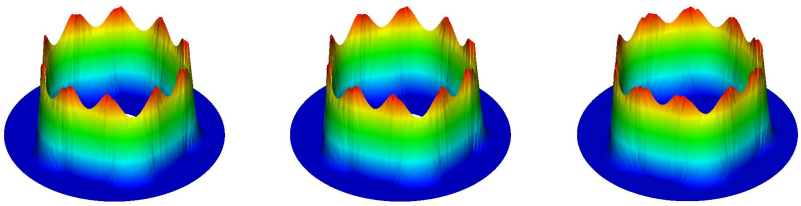

(d) lev. 4, D= 10^{-5} (e) lev. 4, D= 10^{-2} (f) lev. 4, D = 1.0

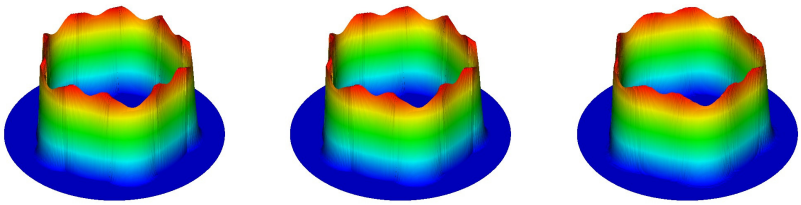

(g) lev. 5, D= 10^{-5} (h) lev. 5, D= 10^{-2} (i) lev. 5, D= 1.0

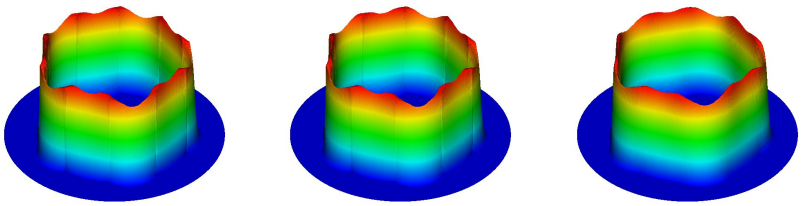

(j) lev. 6, D= 10^{-5} (k) lev. 6, D= 10^{-2} (l) lev. 6, D= 1.0

Figure 4.7: The TVD scheme, $\varepsilon = 0.125$, $\alpha = 0.0$, at $T = 0.05$ with fixed time step $\Delta t = 0.0005$, left to right an increase in diffusion coefficient and top to bottom an increase in mesh refinement levels. Blue represents the value of $\rho = -1.0$ and red $\rho = 1.0$

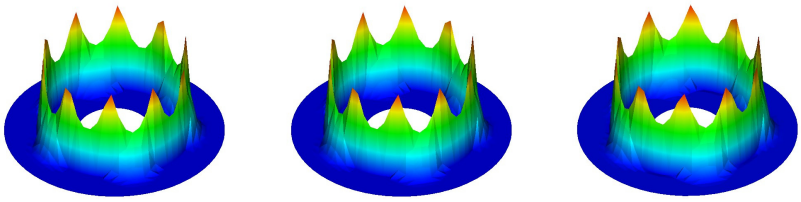

(a) lev. 3, D= 10^{-5} (b) lev. 3, D = 10^{-2} (c) lev. 3, D= 1.0

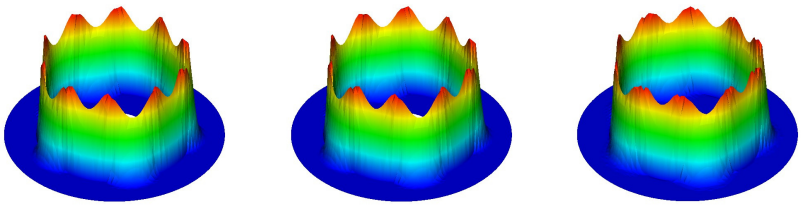

(d) lev. 4, D= 10^{-5} (e) lev. 4, D= 10^{-2} (f) lev. 4, D = 1.0

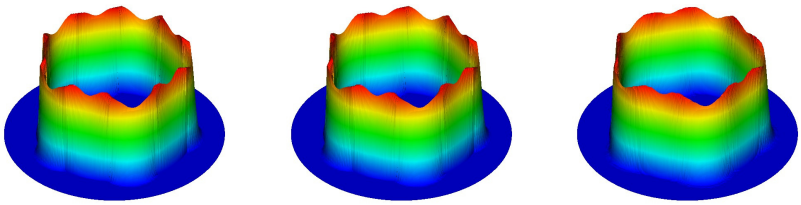

(g) lev. 5, D= 10^{-5} (h) lev. 5, D= 10^{-2} (i) lev. 5, D= 1.0

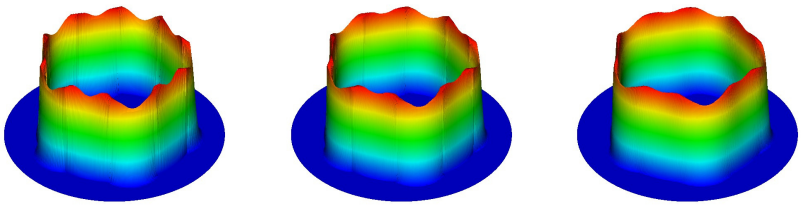

(j) lev. 6, D= 10^{-5} (k) lev. 6, D= 10^{-2} (l) lev. 6, D= 1.0

Figure 4.8: The FCT scheme, $\varepsilon = 0.125$, $\alpha = 0.0$, at $T = 0.05$ with fixed time step $\Delta t = 0.0005$, left to right an increase in diffusion coefficient and top to bottom an increase in mesh refinement levels.

The obtained solutions in figures 4.4(b)–4.4(m) are achieved through the TVD-schemes and 4.4(a) as the respective initial solution. In addition, we have a similar arrangement of solution profile with FCT schemes figures 4.5(b)–4.5(m), with corresponding initial solution 4.5(a). These numerical results are calculated at time

instance $T = 0.05$ with a fixed time step $\Delta t = 0.0005$. In these graphical representation of solution, to avoid redundancy of relatively similar results we ignored some figures concerns to mesh levels of refinement. With these test cases, we can conclude that the surface evolution due to convective term always leads to oscillations in the vicinity of Γ-band, especially for steep gradients of ρ with coarse mesh refinements. The proposed AFC-based schemes of TVD and/or FCT-types yield a smooth, positivity preserving and physically suitable numerical solution. At the same time TVD and FCT-schemes deliver smooth, oscillatory-free and an accurate solutions with low computational cost.
As the interface of the $\Gamma(t)$ is represented through zero-level set function $\phi(\mathbf{x}, t = 0)$, thus we are concerned to the solution profile close to the interface $\Gamma(t)$. We perform similar experiments to investigate the effects of the surface convection in case of small domain denoted by ε, which is approximately six times relatively smaller than the actual domain defined in (4.8). These experiments show that an increase in the value of diffusion coefficient D can bring solution profile almost identical to the initial solution. In case of Ω_ε-domain for small values of ε we are unable to get smooth solution profile which makes the use of stabilization techniques mandatory. We presented in figures 4.6(o)–4.6(a) the standard Galerkin scheme for the small value of the ε, in the Ω_ε–domain. Similarly, figures 4.7(c)–4.7(l) are shown for the TVD-scheme and figure 4.8(a)–4.8(l) for the FCT-type schemes. In figures 4.6(m) and 4.6(n) we can observe that for the diffusion coefficients $D = 10^{-5}$ and $D = 10^{-2}$ we get oscillations even at $8th$-level of mesh refinement. But we obtained a formidable solution profile in case of FCT and TVD-schemes, at mesh refinement level 5, e.g., see figures 4.8(g)–4.8(h) and figures 4.7(g)–4.7(h) with diffusion coefficients $D = 10^{-5}$ and $D = 10^{-2}$.

4.2.3 Surface PDE with different configuration

To check the accuracy and applicability of our numerical scheme, we performed more numerical tests for PDEs on surfaces. The following examples with numerical configurations are modified form of the article [27], where the authors did not include the boundary integrals and noticed that the boundary integral can cause numerical oscillations and suggested a stabilization scheme to avoid non-physical solution. We have experienced the same results using pure Galerkin scheme including the boundary integral expression in the weak formulation.
Lets solve the following partial differential equation posed on evolving surface:

$$\frac{\partial^* \rho(\mathbf{x},t)}{\partial t} = D\Delta_{\Gamma(t)}\rho(\mathbf{x},t) + g(\mathbf{x},t) \qquad \text{on} \quad \Gamma(t). \tag{4.9}$$

Where $\Gamma(t)$ is prescribed by the zero level set of the function

$$\phi(\mathbf{x},t) = |\mathbf{x}| - 1.0 + \sin(4t)(|\mathbf{x}| - 0.5)(1.5 - |\mathbf{x}|). \tag{4.10}$$

The computational domain is same as previous configuration. It is a circular disc with parameters $\Omega = \{\mathbf{x} \in \mathbb{R}^2 : 0.5 \leq |\mathbf{x}| \leq 1.5\}$. The boundary of the domain $\partial\Omega$

is aligned with a curve from the family Γ_r. The analytical solution is chosen to be

$$\rho(\mathbf{x},t) = e^{-t/|\mathbf{x}|^2} \cdot \frac{(x^1)}{|\mathbf{x}|}. \tag{4.11}$$

Since $\Gamma(t)$ is time-dependent, applying mathematical formulation of surface PDEs from §3.4.1 the equation (4.9) transforms into

$$\partial_t \rho + \boldsymbol{v}_S \cdot \nabla \rho + V \frac{\partial \rho}{\partial \boldsymbol{n}} - VH\rho + \rho \nabla_\Gamma \cdot \boldsymbol{v}_S - \Delta_\Gamma \rho = g(\mathbf{x},t)\,.S \tag{4.12}$$

Where H is the mean curvature of $\Gamma(t)$ and therefore $H = -1/|\mathbf{x}|$. Substituting the tangential component of the velocity $v_S = 0$ into (4.12), we get

$$\partial_t \rho + V \frac{\partial \rho}{\partial \boldsymbol{n}} - VH\rho - \Delta_\Gamma \rho = g(\mathbf{x},t). \tag{4.13}$$

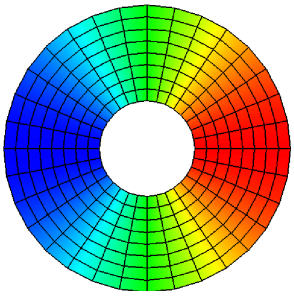

(a) The initial solution and mesh, level 2

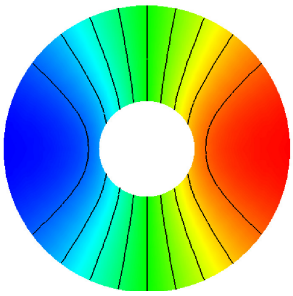

(b) The analytical solution

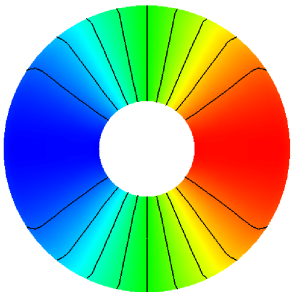

(c) The numerical solution, level 3

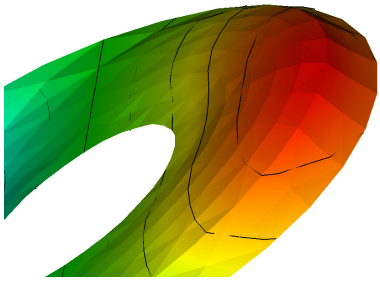

(d) boundary kinks, level 2

Figure 4.9: (a) initial solution and mesh (b) the analytic solution (4.11) (c) the numerical solution (d) the screen shot of implicit scheme with boundary integral(ISwB), the boundary integral causes kinks near boundaries. The 2nd and 3rd levels of mesh refinement consists of 288 and 1088 degrees of freedom, respectively. Blue represents the value of $\rho = -0.95$ and red $\rho = 0.95$

The function $\rho(\mathbf{x},t)$ from (4.11) solves the equation on the surface

$$\partial_t \rho - \Delta_\Gamma \rho = 0.$$

Therefore, using the mean curvature values, we found the following expression for $g(\mathbf{x},t)$

$$g = V\frac{\partial \rho}{\partial \boldsymbol{n}} - VH\rho = V\rho\left(\frac{2t}{|\mathbf{x}|^3} + \frac{1}{|\mathbf{x}|}\right).$$

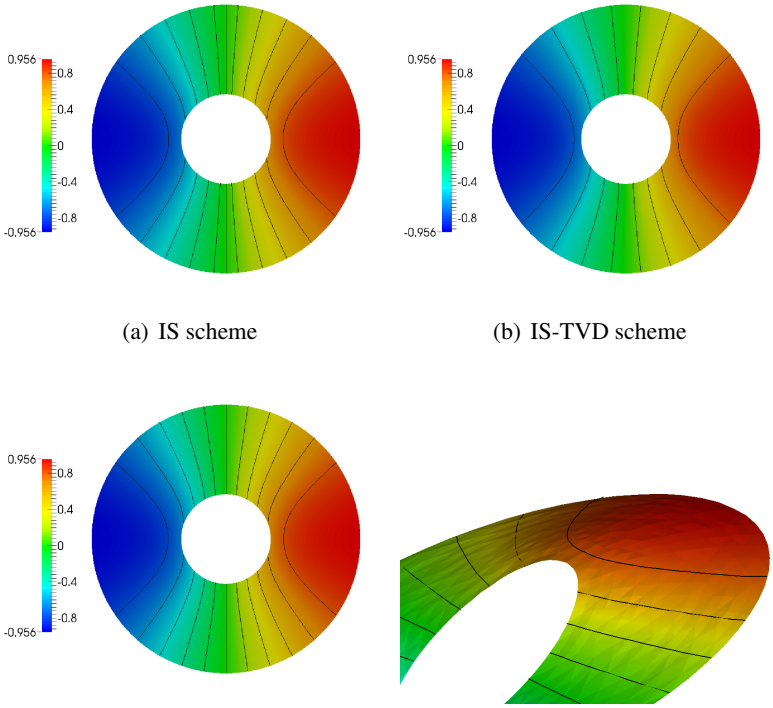

(a) IS scheme (b) IS-TVD scheme

(c) IS-FCT scheme (d) no boundary kinks

Figure 4.10: The numerical solutions obtained by adoption of the fully implicit scheme defined in equation (3.36). (a) is implicit scheme, (b) and (c) are solutions of implicit schemes of TVD and FCT-types, resp. (d) the numerical kinks at boundary are vanished.

As an initial condition, we set $\rho_{\text{init}} = \rho(\mathbf{x}, t=0) = \sin(4\Theta)$, where $\Theta \in [0, 2\pi]$. The Θ is an angle between x^1-axis and $\mathbf{x} = (x^1, x^2)^T$, defined in equation (4.6). The tangential velocity of the surface is $v_S = 0$. Since $\Theta_t = 0$, the normal component of the surface velocity is also vanishing. The mean value of ρ_0 vanishes at every level set Γ_r , hence the solution tends to zero as time approaches infinity. But this occurs at a rate depending on the radius of the circle due to different circles have different diffusion coefficients.

In figures 4.9(c) and 4.9(d) we demonstrate numerical results after the 100th iteration in time with a fixed time step $\Delta t = 0.0005$. The results obtained by a scheme, which include the boundary integral term. Here explicit and implicit schemes reveal the same artifact in the numerical solution. The artificial kinks near the boundary of the domain can propagate in time to the entire domain causing deterioration of the numerical solution. In figures 4.10(a), 4.10(b) and 4.10(c) we show numerical results, which are obtained by the implicit scheme (3.36). One can clearly see much better profiles of the numerical solution. The 3rd level of the mesh refinement is used. In figure 4.10(a) we demonstrate the numerical solution of (3.36) without any stabilization. In figure 4.10(b) the TVD and in figure 4.10(c) the FCT stabilization techniques are applied.

Numerical test with different tangential velocity

In previous example we have assumed that the tangential velocity is zero. To validate our FEM-level set scheme we take an exmaple from [27]. In this test example, everything is similar to last numerical configuration §4.2.3 but the tangential velocity of the surface is defined as:

$$\boldsymbol{v}_S = 10\frac{(-\phi_{x^2}, \phi_{x^1})}{|\nabla\phi|}. \tag{4.14}$$

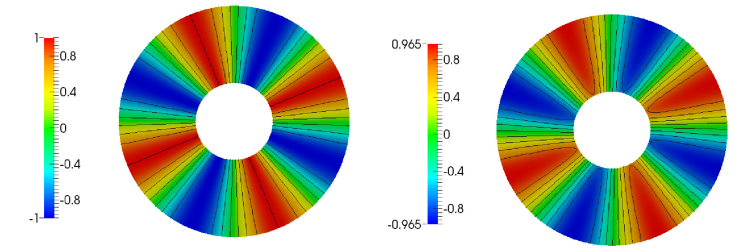

(a) at $t = 0.0$ (b) at $t = 0.002$

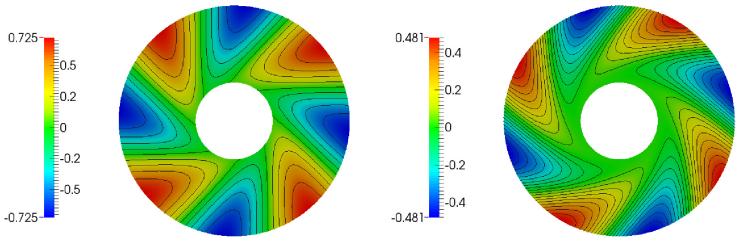

(c) at $t = 0.045$ (d) at $t = 0.1$

Figure 4.11: Numerical solution at various time instances, with fixed time step $\Delta t = 0.0001$

The numerical results at different instances are shown. The figure 4.11(a) is showing the initial solution, figures 4.11(b),4.11(b) and 4.11(b)are showing solution at $t = 0.002, 0.045, 0.1$, respectively.

4.2.4 Order of convergence

Now based on aforementioned test cases, we can provide a positivity preserving scheme embedded with FCT and TVD stabilization. Furthermore, in order to show results on error analysis, we calculate the $L^2(\Omega_\varepsilon)$ and $H^1(\Omega_\varepsilon)$ norms of error and experimental order of convergence (EOC). The corresponding $L^2(\Omega_\varepsilon)$ and $H^1(\Omega_\varepsilon)$ norms are defined by (cf. [27]) the following formulae:

$$L^2(\Omega_\varepsilon)\text{-error} = \left(\frac{1}{|\Omega_\varepsilon|} \int_{\Omega_\varepsilon} \left(\rho_{\text{analyt}}(\mathbf{x},t) - \rho_{\text{num}}(\mathbf{x},t)\right)^2 |\nabla\phi| \right)^{\frac{1}{2}},$$

$$H^1(\Omega_\varepsilon)\text{-error} = \left(\frac{1}{|\Omega_\varepsilon|} \int_{\Omega_\varepsilon} \left(\nabla_\Gamma\rho_{\text{analyt}}(\mathbf{x},t) - \nabla_\Gamma\rho_{\text{num}}(\mathbf{x},t)\right)^2 |\nabla\phi| \right)^{\frac{1}{2}}.$$

The tables (4.1), (4.2) and (4.3) are showing the $L^2(\Omega_\varepsilon)$ and $H^1(\Omega_\varepsilon)$-errors using the corresponding norms

$$L^2(\Omega_\varepsilon) = \|\rho_{\text{analyt}} - \rho_h\|_{L^2(\Gamma)} \quad \text{and} \quad H^1(\Omega_\varepsilon) = \|\nabla\rho_{\text{analyt}} - \nabla\rho_h\|_{H^1(\Gamma)}.$$

Thus, all tables validate the high order of spatial convergence i.e., our numerical scheme approximately is of second order in L^2 and first order in H^1.

Let us denote the numerical error $\{E_i\}_{i=0,\ldots,N}$ in the finite element level set based scheme on a series of uniform refinements of a triangulation $\{\mathscr{T}\}_{i=0,\ldots,N}$. Consider $\{h_i\}_{i=0,\ldots,N}$ as the mesh size and the experimental order of convergence (EOC) is assumed to be measure of the rate of convergence of the scheme, when the maximum mesh size $h_N \to 0$.
The experimental order of convergence are calculated using the following formula Dziuk and Elliott [26], Ranner [97] and Venkataraman [133].

$$EOC(E_{i,i+1}, h_{i,i+1}) = \frac{\log\left(\frac{E_{i+1}}{E_i}\right)}{\log\left(\frac{h_{i+1}}{h_i}\right)}.$$

lev.	d.o.f	$L^2(\Omega_\varepsilon)$ -errors	EOC	$H^1(\Omega_\varepsilon)$ -errors	EOC
$\varepsilon = 0.5$					
2	288	2.60532E-003	–	3.61167E-002	–
3	1088	6.76148E-004	1.946	1.80981E-002	0.996
4	4224	1.79701E-004	1.911	9.15163E-003	0.983
5	16640	4.93317E-005	1.865	4.68961E-003	0.964
$\varepsilon = 0.25$					
2	288	1.65152E-003	–	2.44530E-002	–
3	1088	4.12974E-004	1.999	1.22096E-002	1.00
4	4224	1.02201E-004	2.014	6.10269E-003	1.00
5	16640	2.44469E-005	2.063	3.05108E-003	1.00
$\varepsilon = 0.125$					
2	288	1.28775E-003	–	1.95126E-002	–
3	1088	3.21906E-004	2.000	9.74873E-003	1.001
4	4224	7.90935E-005	2.025	4.82267E-003	1.015
5	16640	1.90064E-005	2.057	2.42365E-003	0.992

Table 4.1: The fully implicit scheme (3.36), $L^2(\Omega_\varepsilon)$ and $H^1(\Omega_\varepsilon)$ errors, order of convergence and number of degrees of freedom in Ω_ε.

The experimental order of convergence and numbers of degrees of freedom (d.o.f) are calculated at 100th iteration with a fixed time step $\Delta t = 0.0005$. The tables (4.3) and (4.2) are shown to check the convergence of the established implicit FCT and TVD schemes. The tables assure the convergence of the AFC-type schemes for surface PDEs. The analysis of L^2 and H^1-errors confirm the theory of the error analysis (see §3.7) equations(3.82)–(3.85) for PDEs on surface. To get more insight we calculate the errors close to steep gradient after modifying the given domain Ω. Let us denote the area of the strip inside annular domain $0.5 \leq \Omega \leq 1.5$, where $\varepsilon = 0.5$. Numerical results for $\varepsilon = 0.25$ and $\varepsilon = 0.125$ are calculated as well. Here again our goal is to get numerical results for smaller value of ε to know solution behavior close to the steep gradient.

lev.	d.o.f	$L^2(\Omega_\varepsilon)$ -errors	EOC	$H^1(\Omega_\varepsilon)$ -errors	EOC
$\varepsilon = 0.5$					
2	288	5.04310E-003	–	7.59220E-002	–
3	1088	1.28061E-003	1.9775	3.81000E-002	0.9947
4	4224	3.26672E-004	1.9709	1.93023E-002	0.9810
5	16640	8.47900E-005	1.9459	9.97292E-003	0.9527

Table 4.2: The TVD scheme for $L^2(\Omega_\varepsilon)$ and $H^1(\Omega_\varepsilon)$–errors, order of convergence and number of degrees of freedom in Ω_ε.

lev.	d.o.f	$L^2(\Omega_\varepsilon)$ -errors	EOC	$H^1(\Omega_\varepsilon)$ -errors	EOC
$\varepsilon = 0.5$					
2	288	5.00131E-003	–	7.59073E-002	–
3	1088	1.27154E-003	1.9757	3.81005E-002	0.9944
4	4224	3.24777E-004	1.9691	1.93052E-002	0.9808
5	16640	8.43970E-005	1.9442	9.97574E-003	0.9525

Table 4.3: The FCT scheme for $L^2(\Omega_\varepsilon)$ and $H^1(\Omega_\varepsilon)$–errors, order of convergence and number of degrees of freedom in Ω_ε.

4.2.5 Transport of species on surface

Consider transport of species ρ on the surface Γ. In this numerical example we would like to demonstrate that numerical stabilization of certain PDEs on surfaces is inevitable even for simple equations. Consequently, we consider the following transport equation

$$\partial_t \rho + \boldsymbol{v} \cdot \nabla_\Gamma \rho = 0, \tag{4.15}$$

on the 3-dimensional geometry of a unit sphere $\Gamma = \{\mathbf{x} : |\mathbf{x}| = 1\}$. Applying the level set methodology, we solve the transport equation (4.15) on level sets $\Gamma_r \subset \Omega$. For the sake of simplicity, the computational domain Ω is chosen to be a union of all level sets Γ_r with $r \in [0.5, 1.5]$. We assume the following initial condition

$$\rho(\mathbf{x},t) = \begin{cases} 10 & \text{if } |\mathbf{x} - (0,0,1)^T| \leq 0.3\ , \\ 0 & \text{else.} \end{cases} \tag{4.16}$$

The advective velocity vector-field is defined by

$$\boldsymbol{v} = \{x^1, 0, -x^3\}^T.$$

The mesh is constructed by refining the coarsest level via connecting opposite midpoints several times. We provide the number of cells and degrees of freedom at every level of refinement in the table (4.4).

level	cells	d.o.f.
0	24	42
1	192	250
2	1 536	1 746
3	12 288	13 090
4	98 304	101 442
5	786 432	798 850
6	6291 456	6340 866

Table 4.4: Levels of mesh refinements, cells and number of degrees of freedom on the computational domain Ω.

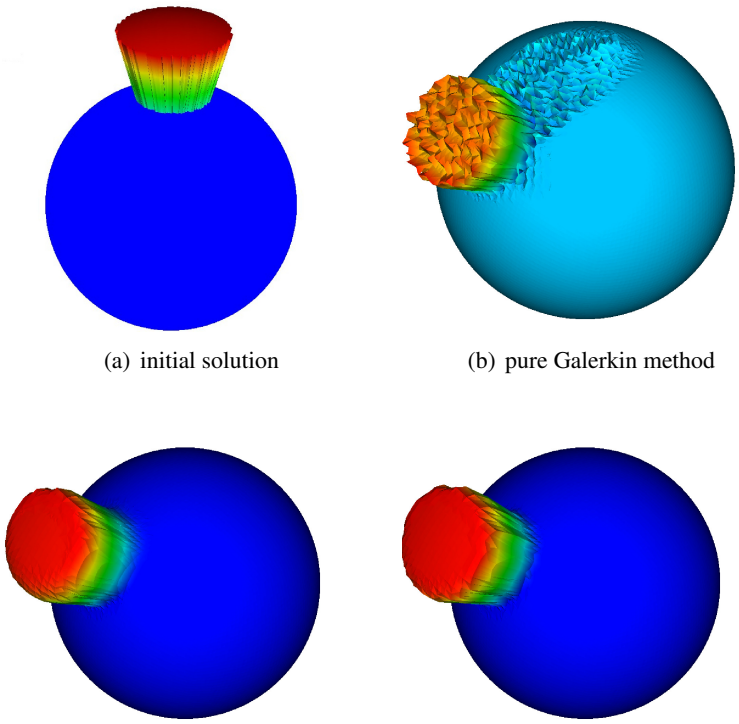

(a) initial solution (b) pure Galerkin method

(c) TVD (d) FCT

Figure 4.12: The numerical results for the transport problem, with fixed time step $\Delta t = 0.001$. Blue represents the value of $\rho = -1.0$ and red $\rho = 10$

For this numerical experiments we use a grid of trilinear finite elements at the 5th level of mesh refinement and edges of hexahedrals are aligned with the level sets. For corresponding reconstruction of level set processes we refer to Turek et al. [128].
We have presented two sets of figures 4.12(a)–4.12(d) and figures 4.13(a)–4.13(d) for species $\rho(\mathbf{x},t)$ on surface Γ. On one hand the first set of figures are showing the specie on the surface, on the other hand the second set of figures are drawn through cutline over x^3-axis. The figure 4.12(a) shows the initial condition for $\rho(\mathbf{x},t)$. The numerical solution for the pure Galerkin scheme at an exemplary time-point $T = 0.2$ is demonstrated in figure 4.12(b). We can clearly observe an artificial oscillations and negative values of $\rho(\mathbf{x},t)$ near region of steep gradient when the specie $\rho(\mathbf{x},t)$ is traveling on surface, see figure 4.13(b). These nonphysical values grow rapidly as time evolve, which leads to the divergence of the algorithm and termination of the simulation. Sokolov et al. [113] showed that the pure Galerkin scheme for chemotaxis problems on stationary surfaces cannot guarantee the positivity preserving and smoothness of the solution. The corresponding FCT/TVD

methodology enable to stabilization of this type of problems and deliver a sufficiently accurate solution, see figures 4.12(c) and 4.12(d) as well as 4.13(c)–4.13(d).

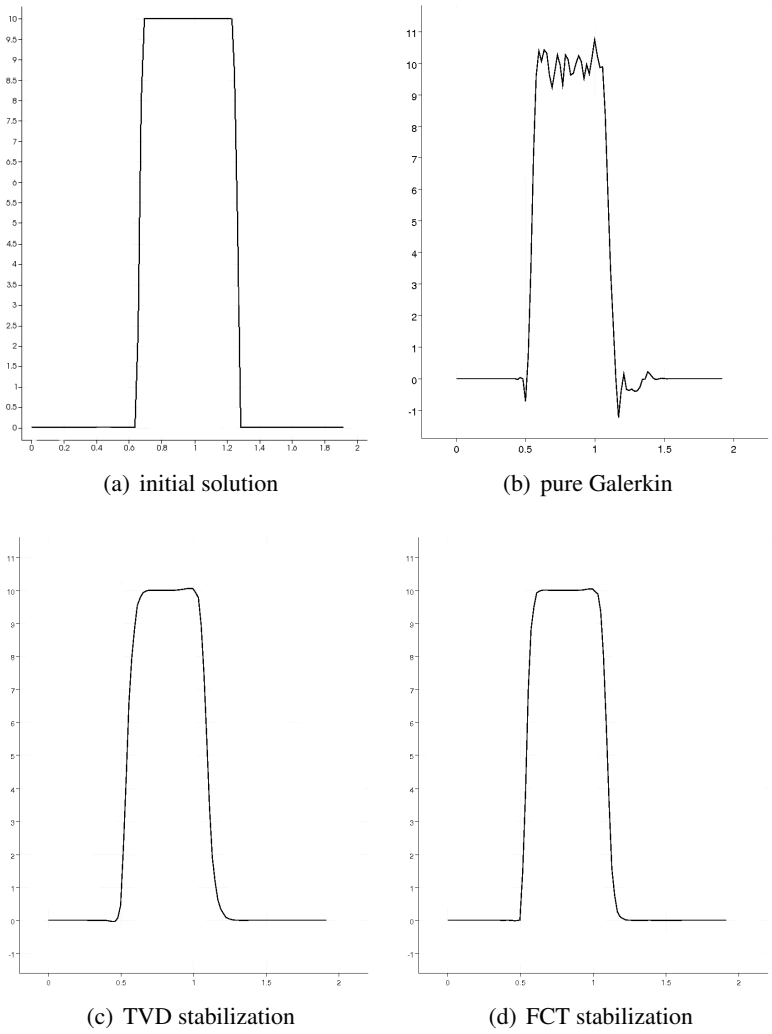

(a) initial solution (b) pure Galerkin

(c) TVD stabilization (d) FCT stabilization

Figure 4.13: Visualization of the solution profile for initial, pure Galerkin, TVD and FCT schemes using cutline along the x^3-axis.

In addition, we observe that the boundary integral term $\int_{\partial\Omega} \rho\varphi\boldsymbol{v}\cdot\boldsymbol{n}_{\partial\Omega}|\nabla\phi|$ can also leads to undesired kinks near the boundary of the computational domain, which can also spread through the entire domain and spoil the numerical solution. An advective term to the surface evolution requires special numerical treatment as well. We show that the pure Galerkin discretization without any stabilization method can leads to artificial oscillations in numerical solutions, especially in the regions with steep gradients.

4.3 Conclusion

A large class of biological and biomedicine problems involve modeling of partial differential equations on manifolds. Recent advancements in developmental biology demand a robust and efficient mathematical technique to find an accurate solution for a realistic model. Such mathematical models includes PDEs on surface and their coupling with domain-defined PDEs. Most biological problems involve evolution and growth. Thus it is essential to execute the modeling of partial differential equations on evolving in time surface [114, 115]. In case of evolving surface we have more complex models describing the surface e.g., the surface convection causes non-physical oscillatory solution. The level set methodology allows for coupling of these mathematical models and provides a systematic procedure to capture the interface. The complexity of the problem substantially increases when the surface and its corresponding level set function are non-stationary. Then we have to treat the surface convection carefully and also we need a robust technique for stabilization of the advective terms appeared due to deformation of the surface, boundary integral, chemotaxis and advective surface material derivatives. In this chapter, we drawn attention to the non-physical solution due to surface convection and inclusion of the boundary integral in the finite element formulation.

In addition, we provided a brief introduction on software implementation and visualization of the numerical solution. We carefully analyzed the scheme with inclusion of boundary integral, pure Galerkin methods, and with FCT/TVD stabilized scheme. From a number of numerical experiments we concluded that stabilization is necessary for the surface PDEs. We shown numerical results for the Ω_ε-domain, to get more insight to the oscillatory solution. We presented numerical results showing the accuracy of the mathematical method. The experimental order of convergences in $L^2(\Omega_\varepsilon)$ and $H^1(\Omega_\varepsilon)$ errors, are calculated for pure Galerkin, FCT and TVD methods, respectively.

The employed mathematical techniques including the level set method, finite element discretization in space and TVD/FCT stabilization of convective and/or advective (chemotaxis) terms with implicit Euler technique for temporal discretization are extended for the 3-dimensional space.

Nature uses only the longest threads to weave her patterns.

Richard P. Feynman

5 Pattern forming models

This chapter addresses the mathematical background and mechanism behind patterns forming models. We introduce the reaction-diffusion system of equations and provide linearization for the nonlinear reactive terms. In addition, we study the order of convergence for patterns forming models. We demonstrate numerical simulations based on finite element level set techniques for a collection of mathematical models, which exhibit patterns. These models are defined for both stationary and evolving in time surfaces. Some of the contents and numerical results of this chapter are already archived in [115].

5.1 Introduction

In general there is a variety of patterns forming models, in particular the biological patterns can arise due to chemotaxis and/or Turing-type instabilities. The pattern-formation mechanisms based on chemotaxis are discussed by Mimura and Tsujikawa [73] and Painter [94]. The diffusion-driven patterns can be developed based on Turing mechanisms [129]. The Turing patterns in the beginning of §1.4.2 has been introduced. In his seminal work on morphogenesis, Turing [129] reveals that chemicals reacts and diffuse in such a way they get steady state patterns. However in his original work he did not consider the effects of geometry and growth, although these processes have a vital role in the development of any organism. It is certain that the mechanism of patterns in animal world are not clearly understood, either experimentally or theoretically. Murray [79, 80] suggests that the mechanism must be genetically controlled. Thus we have to focus on the genetic coding behind patterns. One of the open question in mathematical biology is that how genetic codes are physically translated to forms. Large group of researchers both from experimental and theoretical communities [13, 41, 42, 79, 80, 83, 93, 94, 98, 107] are concerned with the understanding of the mechanism.

It has been discussed that the reaction-diffusion equations exhibit Turing-type instabilities [129]. Miura and Maini [74] reviewed the sensitivity of patterns forming models. They reported that domains, initial and boundary conditions can influence patterns. An important feature of their model addresses the understanding in symmetry of similar size of forms. If the domain size vary the number of structure can change as well. Simply if the domain changes the number of structures

(patterns) increases. This concludes that the number of structures are domain-dependent, e.g., see [74, 94, 133]. The system develop steady state patterns by amplifying specific wavelengths of small fluctuations in the initial guess. Although the solution of the system globally exist, if one change the initial condition, the final structure more or less remains the same. As mentioned in the earlier, the patterns forming mechanisms play a very important role in bio-medical applications. The driven factors of patterns occurrence could be chemotaxis or Turing instability. In this chapter we will focus on systems of Turing-instability type and chemotaxis. The reason is two-fold: on the one hand, there is a wide range of applications for such patterns forming systems (see, e.g., protein-protein interaction on a cell membrane by Goryachev and Pokhilko [45], Rätz and Röger [98]). On the other hand, these are convenient systems to verify the usability of the numerical scheme.

Now we will introduce the conservation law for reaction-diffusion chemotaxis models, which are fundamental equations mainly used to describe patterns in nature.

5.1.1 Reaction-diffusion chemotaxis equation

The reaction-diffusion equation are applied to study the patterns formations. Consider Γ to be an arbitrary surface enclosed in a domain Ω. According to general conservation law the rate of change of the amount of material in a domain Ω is equal to the rate of flow of the material across Γ into Ω added by any reaction g of the material within the domain Ω [80]. We have

$$\frac{\partial}{\partial t}\int_{\Omega}\rho(\mathbf{x},t)d\Omega = -\int_{\Gamma}\boldsymbol{J}\cdot d\Gamma + \int_{\Omega} g(\rho)d\Omega,$$

where ρ is the concentration of the species. The flux of the material is denoted by $\boldsymbol{J}$. Assuming that ρ is continuous and using the divergence theorem to the surface, we obtained the following relation:

$$\int_{\Omega}\left[\frac{\partial}{\partial t}\rho(\mathbf{x},t) + \nabla\cdot\boldsymbol{J} - g\right]d\Omega = 0,$$

since the domain is arbitrary, we get the conservation law for ρ as:

$$\frac{\partial}{\partial t}\rho(\mathbf{x},t) + \nabla\cdot\boldsymbol{J} = g. \tag{5.1}$$

This equation holds for general flux transport $\boldsymbol{J}$.

Chemotaxis model

First taking the chemotaxis phenomena in the system, we can simply define the chemotaxis flux

$$\boldsymbol{J} = \boldsymbol{J}_{\text{diff}} + \boldsymbol{J}_{\text{chemo}},$$

the flux is represented as:

$$\boldsymbol{J}_{\text{diff}} = -\nabla \cdot D^c \nabla c, \quad \text{and} \quad \boldsymbol{J}_{\text{chemo}} = -\rho\chi\nabla c.$$

$$\boldsymbol{J} = -\nabla \cdot D^c \nabla c - \rho\chi\nabla c.$$

Where D^c is diffusion coefficient of the chemical. The system can be chemo-attractant or chemo-repellent depending on the chemo-sensitivity parameter χ. Using these fluxes the Mimura-Tsujikawa chemotaxis reaction-diffusion system will be discussed in §5.2.4.

Reaction-diffusion model

For a classical diffusion case, the generalization of the flux transport is define as:

$$\boldsymbol{J} = \boldsymbol{J}_{\text{diff}} = -D^\rho \nabla \rho,$$

here D^ρ is diffusion of the cell ρ. Now from (5.1) the reaction-diffusion equation for classical model reads:

$$\frac{\partial}{\partial t}\rho(\mathbf{x},t) = \nabla \cdot (D^\rho \nabla \rho) + g(\rho). \tag{5.2}$$

Where $g(\rho)$ is reactive kinetic representing growth or reduction, it can depends on ρ, spatial variable $\mathbf{x}$ and time variable t. Most reaction-diffusion models vary in nature depending on the choice of reactive terms. The diffusion coefficient D^ρ is a matrix depending on ρ and $\mathbf{x}$. In case of no cross diffusion among species it can simply be a diagonal matrix [79, 80]. In this study, we assume D^ρ independent of the spatial variable $\mathbf{x}$, for anisotropic diffusion e.g., see [122], we have

$$\frac{\partial}{\partial t}\rho(\mathbf{x},t) = D^\rho \nabla \cdot \nabla \rho + g(\rho). \tag{5.3}$$

The equation (5.3) can be generalized for more practical phenomena in nature, such as interaction of multi-species or chemicals, each has its own density or concentration, reaction and diffusion coefficients. Hereafter, we are concerned mainly with mathematical models for two variables ρ and ζ on surface Γ.

$$\frac{\partial^* \rho}{\partial t} = D^\rho \Delta_\Gamma \rho + f(\rho,\zeta) \text{ on } \Gamma \times T, \tag{5.4}$$

$$\frac{\partial^* \zeta}{\partial t} = D^\zeta \Delta_\Gamma \zeta + g(\rho,\zeta) \text{ on } \Gamma \times T. \tag{5.5}$$

Where $f(\rho,\zeta)$ and $g(\rho,\zeta)$ are the reactive kinetics. The reaction terms are highly nonlinear in nature for most cases. For example the Schnakenberg model [65] of reaction-diffusion equation on a surface reads as follows:

$$\frac{\partial \rho}{\partial t} = \Delta_\Gamma \rho + \gamma(a - \rho + \rho^2\zeta) \text{ on } \Gamma \times T, \tag{5.6}$$

$$\frac{\partial \zeta}{\partial t} = D\Delta_\Gamma \zeta + \gamma(b - \rho^2\zeta) \text{ on } \Gamma \times T. \tag{5.7}$$

In next section, we discuss linearization of the reactive kinetics based on the Taylor series expansion. The discretization is based on the finite element level set schemes developed in *Chapter 3*.

5.1.2 Linearization of nonlinear reactive terms

Turing systems are often characterized by intricately coupled nonlinear reaction-diffusion equations. Hence, their appropriate treatment in a numerical framework is an important task. In the following we consider the system of reaction-diffusion equations (5.6)–(5.7) with $\Gamma(t)$ being developed according to level set defined in (2.87). We employ the Taylor series expansion to handle the nonlinear reaction terms after splitting the time interval $T = [0, t^M]$ by discrete time instants $0 < t^1 < \ldots < t^M$ and denoting the time step size by $\Delta t = t^{m+1} - t^m$

$$f(\rho^{m+1}, \zeta^{m+1}) \approx f(\rho^m, \zeta^m) + \nabla f(\rho^m, \zeta^m) \cdot \begin{pmatrix} \rho^{m+1} - \rho^m \\ \zeta^{m+1} - \zeta^m \end{pmatrix}, \tag{5.8}$$

$$g(\rho^{m+1}, \zeta^{m+1}) \approx g(\rho^m, \zeta^m) + \nabla g(\rho^m, \zeta^m) \cdot \begin{pmatrix} \rho^{m+1} - \rho^m \\ \zeta^{m+1} - \zeta^m \end{pmatrix}. \tag{5.9}$$

Herein the superscript m denotes the evaluation of the underlying function at the time instant $t = t^m$. We further assume that both $f(\cdot)$ and $g(\cdot)$ can be (naturally) prolonged from $\Gamma(t)$ to the outer region.
By employing the numerical scheme (3.37) together with formulas (5.8) and (5.9) we end up with a linear system of equations for the discrete solution $\mathbf{x}^{m+1} = (\rho_h^{m+1}, \zeta_h^{m+1})^T$ where ρ_h and ζ_h represent the finite element coefficient vectors of ρ and ζ as before:

$$A(\mathbf{x}^m)\mathbf{x}^{m+1} = b(\mathbf{x}^m), \tag{5.10}$$

where the matrix $A(\cdot)$ on the left-hand-side and the vector $b(\cdot)$ on the right-hand-side are defined as

$$A(\mathbf{x}^m) = \begin{pmatrix} \boldsymbol{M} + \Delta t \left(D^\rho \boldsymbol{L} - \boldsymbol{N} + \boldsymbol{R} - \boldsymbol{F}^\rho \right) & -\Delta t \boldsymbol{F}^\zeta \\ -\Delta t \boldsymbol{G}^\rho & \boldsymbol{M} + \Delta t \left(D^\zeta \boldsymbol{L} - \boldsymbol{N} + \boldsymbol{R} - \boldsymbol{G}^\zeta \right) \end{pmatrix}$$

and

$$b(\mathbf{x}^m) = \begin{pmatrix} \boldsymbol{M}\rho_h^m + \Delta t \left(\boldsymbol{F} - \boldsymbol{F}^\rho \rho_h^m - \boldsymbol{F}^\zeta \zeta_h^m \right) \\ \boldsymbol{M}\zeta_h^m + \Delta t \left(\boldsymbol{G} - \boldsymbol{G}^\rho \rho_h^m - \boldsymbol{G}^\zeta \zeta_h^m \right) \end{pmatrix}.$$

Here we use the notations (3.38)–(3.42) to define entries of matrices $\boldsymbol{M}$, $\boldsymbol{L}$, $\boldsymbol{N}$ and $\boldsymbol{R}$ and dropped their dependencies. Moreover, we define the discrete counterparts

of the reaction terms as follows:

$$\boldsymbol{F} = f(\boldsymbol{\rho}_h^m, \boldsymbol{\zeta}_h^m, |\nabla\boldsymbol{\phi}^m|) \quad \text{with} \quad f(\rho_h^m, \zeta_h^m, |\nabla\phi^m|) = \int_\Omega f(\rho_h^m, \zeta_h^m)\varphi_i|\nabla\phi^m|,$$

$$\boldsymbol{G} = g(\boldsymbol{\rho}_h^m, \boldsymbol{\zeta}_h^m, |\nabla\boldsymbol{\phi}^m|) \quad \text{with} \quad g(\rho_h^m, \zeta_h^m, |\nabla\phi^m|) = \int_\Omega g(\rho_h^m, \zeta_h^m)\varphi_i|\nabla\phi^m|,$$

$$\boldsymbol{F}^\rho = f^\rho(\boldsymbol{\rho}_h^m, \boldsymbol{\zeta}_h^m, |\nabla\boldsymbol{\phi}^m|) \quad \text{with} \quad f^\rho(\rho_h^m, \zeta_h^m, |\nabla\phi^m|) = \int_\Omega \partial_\rho f(\rho_h^m, \zeta_h^m)\varphi_i\varphi_j|\nabla\phi^m|,$$

$$\boldsymbol{F}^\zeta = f^\zeta(\boldsymbol{\rho}_h^m, \boldsymbol{\zeta}_h^m, |\nabla\boldsymbol{\phi}^m|) \quad \text{with} \quad f^\zeta(\rho_h^m, \zeta_h^m, |\nabla\phi^m|) = \int_\Omega \partial_\zeta f(\rho_h^m, \zeta_h^m)\varphi_i\varphi_j|\nabla\phi^m|,$$

$$\boldsymbol{G}^\rho = g^\rho(\boldsymbol{\rho}_h^m, \boldsymbol{\zeta}_h^m, |\nabla\boldsymbol{\phi}^m|) \quad \text{with} \quad g^\rho(\rho_h^m, \zeta_h^m, |\nabla\phi^m|) = \int_\Omega \partial_\rho g(\rho_h^m, \zeta_h^m)\varphi_i\varphi_j|\nabla\phi^m|,$$

$$\boldsymbol{G}^\zeta = g^\zeta(\boldsymbol{\rho}_h^m, \boldsymbol{\zeta}_h^m, |\nabla\boldsymbol{\phi}^m|) \quad \text{with} \quad g^\zeta(\rho_h^m, \zeta_h^m, |\nabla\phi^m|) = \int_\Omega \partial_\zeta g(\rho_h^m, \zeta_h^m)\varphi_i\varphi_j|\nabla\phi^m|.$$

The system (5.10) has to be solved in every time step.
Let us summarize the main algorithmic steps required to perform one iteration in time for finding the corresponding solutions at t^{m+1}:

1. Update the recent position of the surface $\Gamma(t^{m+1}) = \{\mathbf{x} : \phi(\mathbf{x}, t^{m+1}) = 0\}$ by solving the transport for the level set function $\phi(\mathbf{x}, t^{m+1})$. equation

$$\frac{\partial\phi}{\partial t} + \boldsymbol{v}\cdot\nabla\phi = 0, \tag{5.11}$$

   This algorithmic step is done by applying the finite element discretization in space §3.3 and the implicit Euler scheme §3.2.1 in time with optional flux-corrected stabilization §3.5 of the convective term $\boldsymbol{v}\cdot\nabla\phi$. Here, we do not explicitly explain the corresponding regularization and reinitialization techniques. Although the analysis of a proper choice is highly demanding and problem dependent. For exemplary studies in this direction the interested readers are therefore kindly referred to corresponding literature, e.g., Turek et al. [128].

2. Calculate the gradient of the level set function $\nabla\phi^{m+1}$. Reassemble matrices, which depend on $|\nabla\phi^{m+1}|$ or $\boldsymbol{v}^{m+1}$. If necessary, perform linearization of the reactive terms, based on (5.8) and (5.9).

3. Solve the system of linear equations (5.10) for the tuple $(\rho^{m+1}, \zeta^{m+1})^T$.

5.2 Numerical results on patterns forming models

In this section we will undertake the convergence studies for patterns forming model in finite element method framework demonstrating the applicability of the coupled finite element level set scheme to selected examples. In the following

section §5.2.1, the spatial convergence of the scheme is validated by considering an example of the heat equation on a curve which is prescribed by the zero level set of the function $\phi(\mathbf{x},t)$. In the next section §5.2.2, the numerical solution of the Schnakenberg model on a nontrivial stationary surface in the three dimensional Euclidean space are shown. In §5.2.3 we exhibit the coupling of the Koch-Meinhardt reaction-diffusion model of the Turing-instability type with the evolution of the level sets, where the velocity is proportional to the numerical solution of the model. The section §5.2.4 is devoted to demonstrate the patterns formation due to chemotaxis-type model.

5.2.1 Convergence study

Let us consider a case study of the convergence of the finite element level set based scheme. For validation purposes we solve the two dimensional heat equation on a pulsating circle as suggested by Dziuk and Elliott [27]. The underlying computational domain Ω is an annular region with outer radius 1.5 and inner radius 0.5, denoted by $R_{0.5}^{1.5}$, such that

$$\Omega \quad = \quad R_{0.5}^{1.5} = \left\{ \mathbf{x} = (x^1, x^2) \in \mathbb{R}^2 \,\middle|\, 0.5 < |\mathbf{x}| < 1.5 \right\}.$$

The analytical reference solution is prescribed as:

$$\rho(\mathbf{x},t) \quad = \quad e^{-t/|\mathbf{x}|^2} \cdot \frac{(x^1)}{|\mathbf{x}|}, \tag{5.12}$$

and solve the heat equation on surface $\Gamma(t)$:

$$\frac{\partial^* \rho(\mathbf{x},t)}{\partial t} = \Delta_{\Gamma(t)} \rho(\mathbf{x},t) + f(\rho).$$

Where on the right hand side $f(\rho)$ must be calculated accordingly. The pulsating circle is determined by the zero level sets of the following analytical reference function

$$\phi(\mathbf{x},t) \quad = \quad |\mathbf{x}| - 1 + \sin(4t)(|\mathbf{x}| - 0.5)(1.5 - |\mathbf{x}|). \tag{5.13}$$

This function is numerically approximated by solving the corresponding level set transport equation (5.11) starting with the initial solution $\phi(\mathbf{x},0) = |\mathbf{x}| - 1$ from equation (5.13). The finite element discretization of (5.11) follows the regular Galerkin approach with first order implicit time integration (Implicit Euler). The transport velocity is determined to fit the analytical reference solution, i.e., ϕ solves

$$\frac{\partial \phi}{\partial t} + \boldsymbol{v} \cdot \nabla \phi \quad = \quad 0,$$

where $\boldsymbol{v} = (v^1, v^2)$ is given by

$$v^1 \quad = \quad -\frac{(x^1)}{|\mathbf{x}|} \frac{4\cos(4t)(|\mathbf{x}| - 0.5)(1.5 - |\mathbf{x}|)}{1 + 2\sin(4t)(1 - |\mathbf{x}|)} = -\frac{\phi_t}{\phi_{x^1}} (x^1)^2 / |\mathbf{x}|,$$

$$v^2 \quad = \quad -\frac{(x^2)}{|\mathbf{x}|} \frac{4\cos(4t)(|\mathbf{x}| - 0.5)(1.5 - |\mathbf{x}|)}{1 + 2\sin(4t)(1 - |\mathbf{x}|)} = -\frac{\phi_t}{\phi_{x^2}} (x^2)^2 / |\mathbf{x}|.$$

We use $\rho(\mathbf{x},0)$ as an initial condition for the simulation and monitor the numerical approximations to the analytical reference solution at the corresponding instance of time. The following numerical data is obtained after 100 time steps with a fixed time stepping of $\Delta t = 0.0001$. This choice accounts for the purpose of documenting the numerical convergence in terms of the spatial discretization and neglecting errors in time. We monitor the numerical error to the reference solutions ρ and ϕ, defined in (5.12) and (5.13), respectively. In figure 5.1 we capture the L^2 and H^1 error of ρ in the annular region $R^{1.125}_{0.875}$ as we are interested mainly in the error close to the zero level set which is located at $|\mathbf{x}| \approx 0.99$.

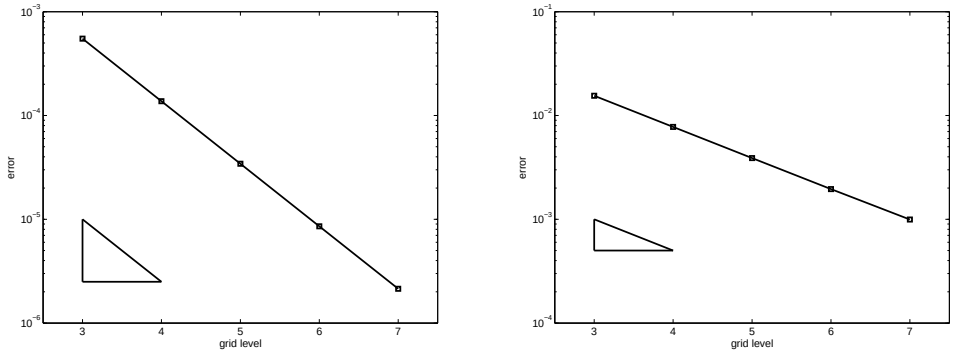

Figure 5.1: Reduction of the numerical L^2 (left) and H^1 (right) error of ρ in the annular strip $R^{1.125}_{0.875}$ for successive grid levels. The reference second and first order of convergence is visualized in terms of the bottom-left triangles, respectively.

Figure 5.2 depicts the L^2_ϕ error of ρ, where

$$L^2_\phi(\Omega) \quad = \quad \left\{ \rho \;\middle|\; \langle \rho, \rho \rangle_\phi < \infty \right\}$$

with the following definition of the inner product and induced norm (cf. [27])

$$\begin{aligned} \langle \rho, \zeta \rangle_\phi &= \int_\Omega \rho \zeta |\nabla \phi| \,, \\ ||\rho||_{L^2_\phi(\Omega)} &= \sqrt{\langle \rho, \rho \rangle_\phi} \end{aligned}$$

Note that this norm is consistent with the definition of the mass matrix in (3.38). The choice of this norm is motivated by the anticipation that $|\nabla\phi|$ is approximately equal to 1 due to sign distance property 2.4.1 at the zero level set. In this case L^2_ϕ is an approximation of $L^2(\Gamma)$. The next plots in figure 5.3 document the L^2 and H^1 errors of the level set function ϕ in the restricted annular region $R^{1.125}_{0.875}$.
All figures validate the high order of spatial convergence, i.e., the scheme is of second order in L^2 and first order in H^1 for both solutions ρ and ϕ. This can be readily observed from the decline of the corresponding plots.

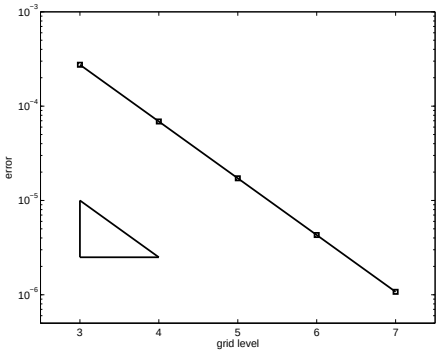

Figure 5.2: Reduction of the numerical L^2_ϕ error of ρ for successive grid levels. The reference second order of convergence is visualized in terms of the bottom-left triangle.

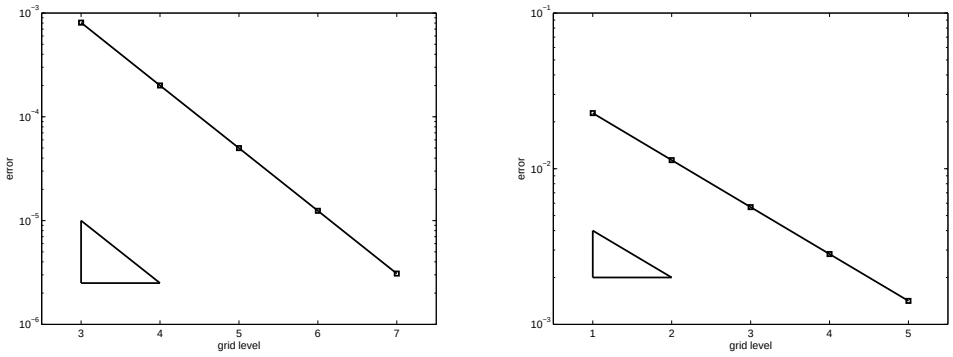

Figure 5.3: Reduction of the numerical L^2 (left) and H^1 (right) error of ϕ in the annular strip $R^{1.125}_{0.875}$ for successive grid levels. The reference second and first order of convergence is visualized in terms of the bottom-left triangles, respectively.

5.2.2 Schnakenberg model on the stationary surface

In this example we consider the performance of the solver for Schnakenberg model of the Turing-type instability on stationary surface. For this purpose we compute the numerical solution of the Schnakenberg model on a stationary surface Γ, which mathematically reads as follows

$$\frac{\partial \rho}{\partial t} = \Delta_\Gamma \rho + \gamma(a - \rho + \rho^2 \zeta) \text{ on } \Gamma \times T, \tag{5.14}$$

$$\frac{\partial \zeta}{\partial t} = D\Delta_\Gamma \zeta + \gamma(b - \rho^2 \zeta) \text{ on } \Gamma \times T. \tag{5.15}$$

Where a, b are constants and γ is showing the relative strength of the reaction terms. The increase in γ may results an increase in the activity of some rate of the

reaction-kinetics. An increase in γ can also be assumed a decrease in the diffusion coefficients. The diffusion coefficient for $D > 1$, will provide the concept of local activation and inhibition. This is a generic spatial mechanism essential for the spatial patterning. It is obvious to assume that the diffusion coefficient of the inhibition must be larger than that of the activator.

Now for the underlying computational domain Ω we choose the cube $\Omega = (-2.5, 2.5)^3$. The zero level set of the function $\phi(\cdot)$ implicitly prescribes the stationary surface Γ of an animal-like geometry. The presented numerical results are courtesy of Penstorf [95].
For certain parameter settings it is known that the solution $(\rho, \zeta)^T$ of the system (5.14)–(5.15) reveals instabilities due to Turing-type effects. The objective of the following numerical assay is to verify that the finite element method level set scheme can capture these instabilities.

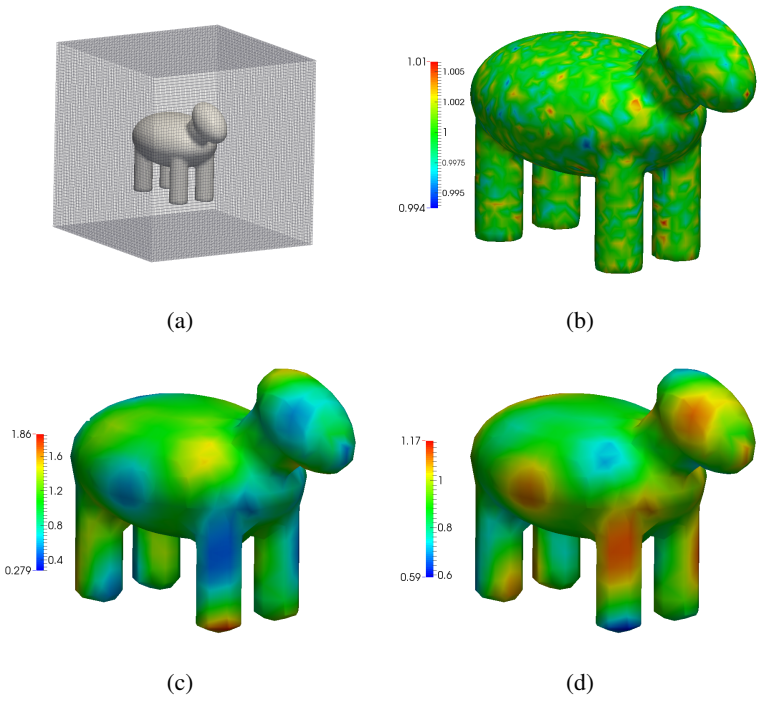

(a) (b)

(c) (d)

Figure 5.4: (a) Mesh with an embedded zero-level set prescription of Γ (b) Initial condition for ρ (c) values of ρ and (d) values of ζ at $t = 1.0$ for the parameter-setting $\gamma = 25.0, D = 10.0$.

The configuration reads as follows: We take the constants as

$$a = 1.0, \quad b = 1.0,$$

set the initial conditions $\rho(\mathbf{x}, t = 0) = \rho_{init}$ and $\zeta(\mathbf{x}, t = 0) = \zeta_{init}$ as a random small

perturbation from the steady state point $(0,0)^T$ i.e.,

$$\rho_{init} = 1.0 + \text{rand} \cdot 10^{-2},$$
$$\zeta_{init} = 1.0 + \text{rand} \cdot 10^{-2},$$

with rand to be a random number in the interval $[-1.0, 1.0]$. We start from the time point $t = 0$ and proceed in time with the time step $\Delta t = 0.005$ until $t = 1.0$, i.e., performing 200 iteration steps. The mesh of the underlying geometry embedded with zero level set function placed as surface Γ in 5.4(a). The random initial condition of ρ_{init} is presented in 5.4(b). For the parameter setting $\gamma = 25$, $D = 5$ we observe that the numerical solution converges back to its steady state $(0,0)^T$. Whereas for parameter settings $\gamma = 25$, $D = 10$ and $\gamma = 85$, $D = 10$ we obtain patterns that arise due to Turing instabilities, see figures 5.4(c) and 5.4(d).

5.2.3 Koch-Meinhardt model on an evolving surface

We consider the following reaction-diffusion model for Turing on evolving surface from Koch and Meinhardt [57]:

$$\frac{\partial \rho}{\partial t} = \alpha_1 \rho \left(1 - r_1 \zeta^2\right) - \zeta \left(1 - r_2 \rho\right) + D^{\rho} \Delta_{\Gamma(t)} \rho \text{ on } \Gamma(t) \times T, \qquad (5.16)$$

$$\frac{\partial \zeta}{\partial t} = \beta_1 \zeta \left(1 + \frac{\alpha_1 r_1}{\beta_1} \rho \zeta\right) + \rho \left(\gamma_1 - r_2 \zeta\right) + D^{\zeta} \Delta_{\Gamma(t)} \zeta \text{ on } \Gamma(t) \times T \qquad (5.17)$$

Where the surface $\Gamma(t)$ is the unit circle situated at the origin of the coordinate system. The surface evolves in time with the velocity field $\boldsymbol{v}$. Again, it is known that under certain conditions on the parameters the Koch-Meinhardt reaction-diffusion model exhibits a Turing instability.
This example shall prove that the finite element level set scheme allows to study the complex patterns formations on a surface those deformations are monitored by the solution of a PDE system (such as the Koch-Meinardt model (5.16)–(5.17) given above). Therefore we choose the velocity $\boldsymbol{v}$ of $\Gamma(t)$ to be proportional to ρ, i.e., we set

$$\boldsymbol{v} = 0.01 \rho \boldsymbol{n}, \qquad (5.18)$$

with $\boldsymbol{n} = \nabla\phi(\mathbf{x},t)/|\nabla\phi(\mathbf{x},t)|$ denoting the outward normal defined in equation (2.82) at a certain level set. While solving the transport equation for the level set function ϕ, we assume that its zero level set is located at a significant distance away from $\partial\Omega$ and therefore the boundary $\partial\Omega$ does not influence a position of $\Gamma(t^{m+1}) = \{\mathbf{x} : \phi(t^{m+1}, \mathbf{x}) = 0\}$ during the time point t^{m+1} (i.e., no prescription of ϕ on $\partial\Omega$ is required). We choose the annular region $R_{0.5}^{1.5}$ as underlying domain as its inner and outer boundaries are aligned with some initial level set $\Gamma_r(t=0) = \{\mathbf{x} \,|\, \phi(\mathbf{x}, t=0) = r\}$.

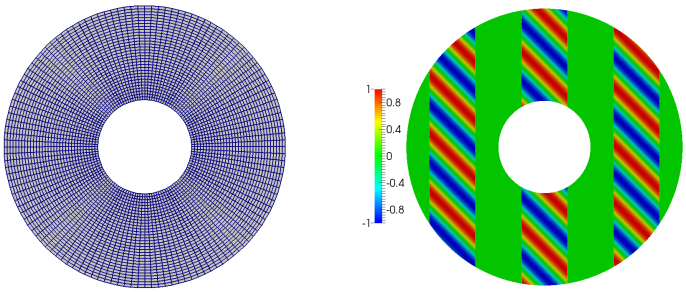

(a) mesh (b) $\rho(\mathbf{x}, t=0)$

Figure 5.5: (a) Mesh of a four-fold refinement, (b) initial condition for ρ.

The parameter setting in (5.16)–(5.17) is taken to be as follows

$$D^{\rho} = 0.88 \cdot \delta_1\,, \qquad D^{\zeta} = 5.16 \cdot \delta_1\,,$$
$$\delta_1 = 0.0045\,, \qquad \gamma_1 = -0.899\,,$$
$$\alpha_1 = 0.899\,, \qquad \beta_1 = -0.91\,.$$

The time-step is taken to be $\Delta t = 0.001$. For the spatial discretization we use an 'almost' uniform mesh of 262 144 quadrilaterals which corresponds to a seven-fold mesh refinement. This level of refinement results in an overall of 263 168 degrees of freedom. Exemplary, in figure 5.5(a) we depict the level 4 mesh resulting from a four-fold mesh refinement. As a particular example of emergence of complicated patterns we choose the following sinusoidal initial conditions for ρ and ζ, see figure 5.5(b),

$$\rho(\mathbf{x})\,|_{t=0} = \begin{cases} \sin\Big(10(x^1+x^2)\Big), & \text{if } x^1 \in [-1.25,-0.75]\cup[-0.25,0.25]\cup[0.75,1.25]\,, \\ 0, & \text{else}\,. \end{cases}$$

$$\zeta(\mathbf{x})\,|_{t=0} = \begin{cases} \cos\Big(10(x^1+x^2)\Big), & \text{if } x^1 \in [-1.25,-0.75]\cup[-0.25,0.25]\cup[0.75,1.25]\,, \\ 0, & \text{else}\,. \end{cases}$$

Concerning the evolution of the level set function $\phi(\cdot)$, we solve the level set transport equation (5.11) with the velocity as defined above in equation (5.18). Initially we prescribe the solution $\phi(\mathbf{x},0)$ to satisfy

$$\phi(\mathbf{x},0) = |\mathbf{x}| - 1.0\,. \qquad (5.19)$$

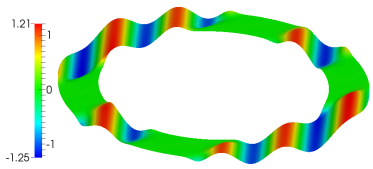

(a) ρ at $t = 0.2$

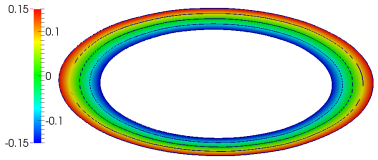

(b) level set ϕ at $t = 0.2$

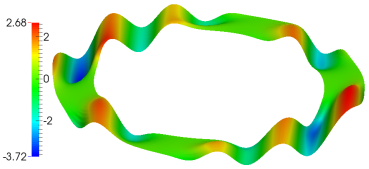

(c) ρ at $t = 1.0$

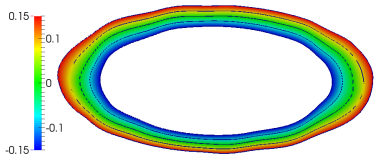

(d) level set ϕ at $t = 1.0$

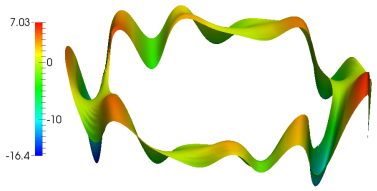

(e) ρ at $t = 2.0$

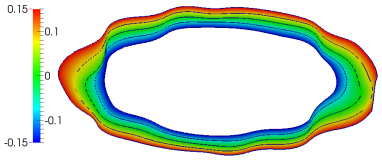

(f) level set ϕ at $t = 2.0$

Figure 5.6: Numerical solutions for ρ and ϕ in the ε-band Ω_ε of the width $\varepsilon = 0.15$ at different time points.

The numerical solution of the system (5.16)–(5.17) reveals classical characteristics of Turing-type instabilities. Herein the solutions' maxima and minima increase and decrease, respectively, as time evolves. The coupling of (5.16)–(5.17) with the transport equation (5.11) through (5.18) leads to the deformation of the level sets Γ_r which in turn influences the system (5.16)–(5.17). Figure 5.6 depicts the dynamics of the numerical solution for ρ and ϕ in a Γ-band of width 0.15. As time evolves we recognize a strong deformation of the level sets in the vicinity of large values of the solution ρ as expected by the choice of the level set velocity (5.18).

5.2.4 Chemotaxis patterns formation on a sphere

Now we will discuss chemotaxis patterns forming model from the reaction-diffusion advection equations (1.8) and (1.9), we have

$$c_t = D^c \Delta c - \alpha c + \beta \rho \quad \text{in} \quad \Omega, \tag{5.20}$$

$$\frac{\partial^* \rho}{\partial t} = D^\rho \Delta_{\Gamma(t)} \rho - \nabla \cdot (\chi \rho \nabla_{\Gamma(t)} c) + \rho(1-\rho) \quad \text{on } \Gamma. \tag{5.21}$$

For a stationary surface with the following parameter setting

$$D^c = 1, \quad D^\rho = 0.0625, \quad \alpha = 32.0, \quad \beta = 1 \quad \text{and} \quad \chi = 8.5,$$

we have an example of chemotaxis patterns formation from Mimura and Tsujikawa [73] and Sokolov et al. [113]

$$c_t = \Delta c - 32.0c + \rho \quad \text{in} \quad \Omega, \tag{5.22}$$

$$\partial_t \rho = 0.0625 \Delta_\Gamma \rho - 8.5 \nabla \cdot (\rho \nabla_\Gamma c) + \rho(1-\rho) \quad \text{on } \Gamma. \tag{5.23}$$

Here we show coupling of a surface-defined equation with an equation which is defined in the entire domain Ω. For this reason, we solve the Mimura-Tsujikawa-type model [73, 113] which describes the propagation of motile cells of *E coli*, in such a way that the cell density ρ travels along a membrane $\Gamma \subset \Omega$, while the chemoattractant c lives in Ω e.g., wherein the cell density ρ can be naturally prolongated to Ω as well. The initial conditions are chosen as follows

$$\begin{aligned} \rho(\mathbf{x}, t=0) &= 1 + \sigma(\mathbf{x}), \\ c(\mathbf{x}, t=0) &= 1/32, \end{aligned}$$

where $\sigma(\mathbf{x})$ is defined as

$$\sigma(\mathbf{x}) = \begin{cases} 0.2, & \text{if} \quad |\mathbf{x} - (5,0,0)^T| \leq 1.5, \\ 0, & \text{otherwise.} \end{cases}$$

We prescribe zero-flux boundary conditions on boundary for c and ρ. As we are always interested for the solution on surface, thus as a computational domain we take

$$\Omega = \{\mathbf{x} : 4.8 \leq |\mathbf{x}| \leq 5.2\}$$

and $\Gamma = \{\mathbf{x} : |\mathbf{x}| = 5\}$ which is defined by the zero level of the level set function defined

$$\phi = \sqrt{(x^1)^2 + (x^2)^2 + (x^3)^2} - 5.0$$

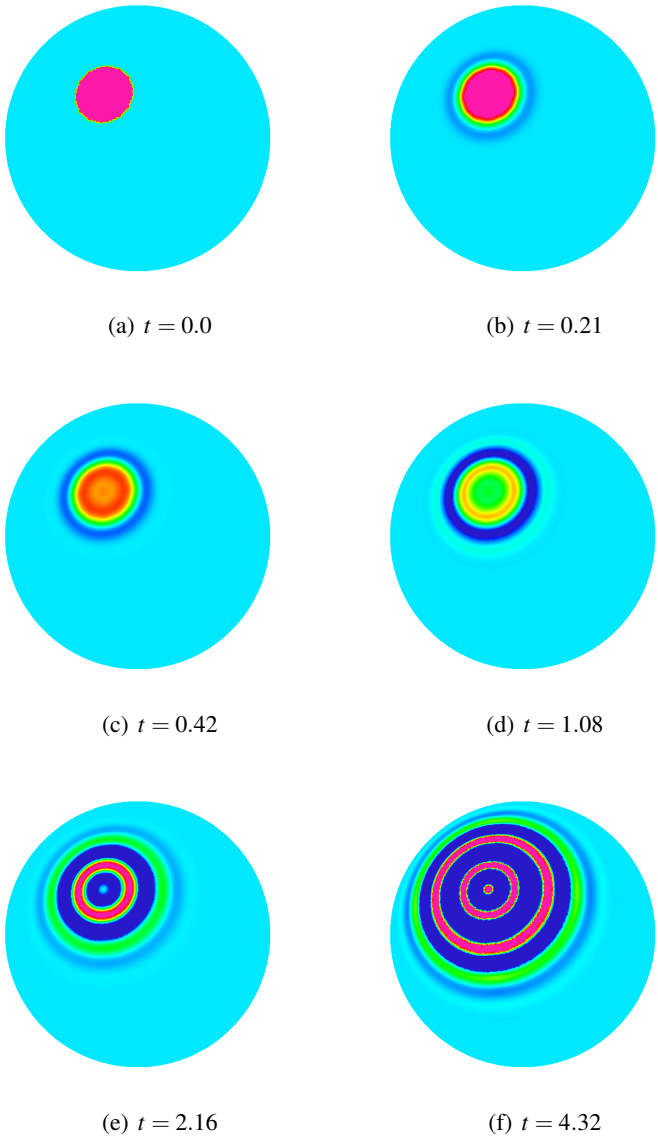

(a) $t = 0.0$ (b) $t = 0.21$

(c) $t = 0.42$ (d) $t = 1.08$

(e) $t = 2.16$ (f) $t = 4.32$

Figure 5.7: Chemotaxis patterns formation on a sphere with fixed time step $\Delta t = 0.01$.

The numerical scheme is able to capture the complex dynamics of the cell density. As Strehl et al. [113, 118] noticed that for the case, when $\rho \in \Omega^d$, $d = 2,3$, we observe a similar behavior, but now on a sphere. Namely, placed in a point $\mathbf{x} = (5,0,0)^T$, the initial concentration of bacteria propagates along Γ in a moving wave-patterns as a response to the chemosensitivity parameter χ, see figures 5.7(a)–5.7(f). Here the algebraic flux-corrected method of FCT-type to preserve the positivity of the cell density. Figure 5.7(a) is the initial configura-

tion and figures 5.7(b)–5.7(f) are the screen shots of chemotaxis patterns taken for $t = 0.21, 0.42, 1.08, 2.16$ and 4.32 with fixed time stepping $\Delta t = 0.01$.

5.3 Conclusion

This chapter introduced pattern forming models, such as Turing-type instabilities and chemotaxis. These models mostly involve nonlinear reactive kinetics. We provide linearization of nonlinear reaction terms using the Taylor series expansion. Advancing the developed schemes from previous chapter, we provided matrix representation of the finite element coefficient vectors. Moreover, the main idea on algorithmic steps are summarized, it required to perform iteration in time for finding the corresponding solutions. The performed convergence studies and numerical results are illustrated graphically.

This numerical framework can be used for systems of the reaction-diffusion equations on stationary and evolving in time surfaces. The proposed framework combines the level set methodology for the implicit description of the time dependent surface $\Gamma = \Gamma(t)$, the Eulerian finite element formulation for the numerical treatment of partial differential equations and the flux-corrected transport schemes for the numerical stabilization of arising advective/chemotaxis and convective (due to surface evolution) terms, respectively.

The numerical results support the reliability of the proposed computational framework based on numerical convergence and capturing of expected solution profiles. The developed methodology is applied to realistic biological phenomena such as Schnakenberg model on stationary surface and Koch-Meinhardt model on evolving in time surface and a modified Mimura-Tsujikawa model for chemotaxis patterns-formation on a sphere. The scheme is capable to capture complex dynamics of cell for biomathematical models on surfaces. This approach can readily be employed for more complex biological applications that involve PDEs on surfaces.

This framework is also applicable to three dimensional models which is mandatory considering real-life applications. Since the computational and analytical complexity significantly increases in three dimensional case.

6

Summary and outlook

This work is mainly focused on the study of reaction-diffusion-convection/advection types of equations with biological applications. It is concerned with the biological pattern forming models of chemotaxis and Turing-type systems. These systems of equations were posed on stationary and evolving in time surfaces. Mathematically, such models consist of coupled reaction-diffusion equations for the case of Turing-type models and reaction-diffusion-advection equations to describe chemotaxis phenomena. The coupled systems of equations are mostly defined on a bulk surface.

In general, the main results of this work are confined to the mathematical modeling and numerical simulation of the surface defined PDEs. On one hand, a rigorous mathematical foundation to treat surface defined PDEs is provided. On the other hand, an accurate and robust numerical scheme for the solution of reaction-diffusion-convection equations on stationary and evolving in time surfaces are presented. The frequently used formulae are proved to treat geometrical partial differential equations. A numerical framework based on the finite element level set method to solve surface PDEs with possible biological applications is provided.

A brief note on the mathematical foundation with widely used theoretical results of surface defined PDEs and its applications are highlighted as well. The peculiar characteristics based on proofs of theorems, lemmas and remarks are provided to analyze the nature of the surface PDEs. The state of the art numerical framework is built for such kind of highly nonlinear partial differential equations on stationary and evolving surfaces.

In addition, the numerical analysis gives a rigorous justification to use the AFC technique for PDEs on the surface. Our results illustrate that one can overcome the pervasive role of the surface convection, which influences the solution profile and produces non-physical oscillations. In most researches the surface boundary integral is not included, but this study contains the boundary integral term as well. Based on illustrative numerical experiments it has been observed that the standard Galerkin is not sufficient to achieve a physically accurate solution for such models.

A brief summary including pros and cons of different numerical techniques to solve surface defined PDEs is provided. For the presented numerical investigation, the level set approach has been used. Thus the interface is captured through a level set function $\phi(\mathbf{x},t)$. The surface Γ is aligned with a zero level set function

$\phi(\mathbf{x},t=0)$. It further developed our interest to study the nature of solution profile in the ambient space of $\Gamma(t)$, which is assumed to be the zero level set function. In addition, an illustrative observation for the case of reduced domain Ω_ε in the neighborhood of the surface Γ is taken under consideration. It has been concluded that the solution profile close to the steep gradient is full of spurious kinks, in the absence of the stabilization schemes.

The numerical results of the study suggest the development of a stabilized numerical scheme for partial differential equation on an evolving domain. Consequently, an algebraic flux correction (AFC) scheme has been constructed and implemented for several test cases. The numerical oscillations are eliminated using the AFC techniques of FCT (flux-correction transport) and TVD (total variation diminishing) schemes. The numerical evidence for the optimal order of convergence for the proposed scheme has been derived and discussed.

The $L^2(\Omega_\varepsilon)$ and $H^1(\Omega_\varepsilon)$-error norms are calculated and confirmed the order of convergence as second order in $L^2(\Omega_\varepsilon)$ and first order in $H^1(\Omega_\varepsilon)$. The numerical results are further supported through an extensive computational experiment, in which one seeks not only to validate the theoretical results but also examine some of the interesting phenomena that arise due to the nature of surface defined PDEs. Such as the effects of convective terms, evolution of the domain and change in the region close to the interface of surface Γ.

In the last part of the study, we simulated and investigated pattern forming models of Turing-type instability and chemotaxis on surface. The novelty of the approach is the incorporation of complex realistic biomathematical models on surfaces. The biological models include the Schnakenberg model and the Koch-Meinhardt model of Turing-type instabilities and the modified Mimura-Tsujikawa-type for chemotaxis pattern formation on surfaces. Here an Eulerian finite element method for spatial discretization has been taken and the temporal discretization is performed through backward Euler scheme. An illustrative numerical simulation has been carried out on 2- and 3-D models for stationary and evolving surfaces having different numerical configuration and mesh geometries.

As an outlook we indicate the possible future research in the field of numerical treatment of reaction-diffusion and/or chemotaxis model on surface.

- **General surface evolution:** In this study there are few assumptions on the evolution of surface $\Gamma(t)$. These are somehow natural to assume for mathematical problems posed on the surface. In more general cases, these assumptions and constraints on evolution bring limitations in the physical models e.g., for unknown growth rates and/or concentration-driven growth, in such cases the surface evolution leads to topological changes. These phenomena occur more often in biological systems e.g., tumours growth, biological membrane, animal skin and cell motility. Consequently, the mathematical modeling and analysis of reaction-diffusion-convection equations posed on surface with more complex evolution could be an interesting direction to work.

- **Reinitialization of the level set function:** The evolution of surface Γ is considered with as a zero level set function $\phi(\mathbf{x},t)$. The movement of the interface captured through the level set function. The evolution often distort the level set function when its slope is too high or too flat close to the interface. In principal, a small change in level set function may affect the location of the interface, which may lose the regularity in the neighborhood of the interface. The static sign distance function is not sufficient to correctly capture the interface. Therefore, an important area for future research is relying on the improvement of the reinitialization for the level set function. Other possible way could be the development of an alternative techniques such as phase field method.

- **Adaptive approaches:** In the present study, we use uniform mesh refinement and uniform time stepping schemes for solution. But the adaptive refinement of the numerical schemes is currently more required. For example, the adaptive mesh refinement can enhance the computational ability and storage capacity. It can be helpful to have a commanding grid resolution to communicate characteristics of solution at a specific location of geometry (mesh). Thus a combination of a FEM-stabilized adaptive mesh refinement with an adaptive time stepping scheme for general models would be an interesting task.

- **Curvature-driven models:** The biological surfaces (i.e., membranes, animal coat, tumour growth) are growing subjects. The curvatures play an important role for modeling and finding the solution for such sort of surface defined PDEs models. Besides both static and evolving deformation of surface, a newly developed technique based on energy variational formulation (Willmore flow model) can be employed for pattern forming models.

- **Generalized Keller-Segel model:** The nature of general biological models are complicated e.g., in case of an interactive multiple species in the presence of several chemo-attractant/repellents. The problems of multi-species and multi-chemo models exist in nature and mathematical models has been discussed in current work. The theoretical and numerical analysis of such a complex mathematical model can be extremely difficult to perform, as it consists of significantly increasing number of parameters.

- **Parallelization:** The modeling of general biological models could be very complex set of coupled partial differential equations. Sometimes even the advanced multi-core processors are not sufficient to perform numerical simulations. Consequently, the numerical solution of such system requires a full parallelization of the developed numerical software. Consequently, parallelization of numerical software for general models, and use of high performance computing could be an interesting work to apply for coupled PDEs.

Bibliography

[1] D. Adalsteinsson and J.A. Sethian. A level set approach to a unified model for etching, deposition and lithography I: Algorithms and two-dimensional simulations. *Journal of Computational Physics*, 120(1):128–144, 1995.

[2] M. Aida, T. Tsujikawa, M. Efendiev, A. Yagi, and M. Mimura. Lower estimate of the attractor dimension for a chemotaxis growth system. *Journal of the London Mathematical Society*, 74(2):453–474, 2006.

[3] R. Barreira, C.M. Elliott, and A. Madzvamuse. The surface finite element method for pattern formation on evolving biological surfaces. *Journal of Mathematical Biology*, 63(6):1095–1119, 2011.

[4] T. Batygina. Morphogenetic developmental programs: Stem cells. *Nova Science Publishers*, 2011.

[5] M. Bergdorf, I.F. Sbalzarini, and P. Koumoutsakos. A lagrangian particle method for reaction-diffusion systems on deforming surfaces. *Journal of Mathematical Biology*, 61(5):649–663, 2010.

[6] J.P. Boris and D.L. Book. Flux-corrected transport. I. SHASTA, a fluid transport algorithm that works. *Journal of Computational Physics*, 11:38–69, 1973.

[7] Y. Boykov, V. Kolmogorov, D. Cremers, and A. Delong. An integral solution to surface evolution PDEs via geo-cuts. *Lecture Notes in Computer Science (including subseries Lecture Notes in Artificial Intelligence and Lecture Notes in Bioinformatics)*, 3953 LNCS:409–422, 2006.

[8] D. Braess. Finite Elements Theory, Fast Solvers and Applications in Solid Mechanics. *Cambridge University Press*, 2007.

[9] S.C. Brenner and L.R. Scott. The Mathematical Theory of Finite Element Methods. *Springer, New York*, 2002.

[10] C. Budd, W. Huang, and R.D. Russell. Adaptivity with moving grids. *Acta Numerica*, 2009.

[11] E.O. Budrene and H.C. Berg. Complex patterns formed by motile cells of escherichia coli. *Nature*, 349(6310):630–633, 1991.

[12] M.P.D. Carmo. Differential Forms and Applications. *Springer-Verlag*, 1994.

[13] V. Castets, E. Dulos, J. Boissonade, and P. De Kepper. Experimental evidence of a sustained standing turing-type nonequilibrium chemical pattern. *Physical Review Letters*, 64(24):2953–2956, 1990.

[14] H.S. Chase. Fundamental forms of surfaces and the Gauss-Bonnet theorem. *University of Chicago, Chicago*, 2012.

[15] I. Chavel. Riemannian Geometry: A Modern Introduction. *Cambridge University Press*, 2006.

[16] A.Y. Chernyshenko and M.A. Olshanskii. An adaptive octree finite element method for PDEs posed on surfaces. *Computer Methods in Applied Mechanics and Engineering*, 291:146–172, 2015.

[17] S. Childress and J.K. Percus. Nonlinear aspects of chemotaxis. *Mathematical Biosciences*, 56(3-4):217–237, 1981.

[18] D.L. Chopp and J.A. Sethian. Motion by intrinsic Laplacian of curvature. *Interfaces and Free Boundaries, Oxford University Press*, (1):1–18, 1999.

[19] G.E. Christensen, R.D. Rabbitti, and M.I. Miller. 3-D brain mapping using a deformable neuroanatomy. *Physics in Medicine and Biology*, 39(3):609–618, 1994.

[20] L. Chunming, X. Chenyang, G. Changfeng, and D.F. Martin. Distance regularized level set evolution and its application to image segmentat. *IEEE Trans. on image processing*, (12):3243–3254, 2010.

[21] J. Condeelis, R.H. Singer, and J.E. Segall. The great escape: When cancer cells hijack the genes for chemotaxis and motility. *Annual Review of Cell and Developmental Biology*, 21:695–718, 2005.

[22] B. Dong. Applications of variational models and partial differential equations in medical image and surface processing. *UCLA*, 2009.

[23] B. Dong, A. Chien, Y. Mao, J. Ye, F. Vinuela, and S. Osher. Level set based brain aneurysm capturing in 3-D. *Inverse Problems and Imaging*, 4(2):241–255, 2010.

[24] J. Dorsey and P. Hanrahan. Digital materials and virtual weathering. *Scientific American*, 282(2):64–71, 2000.

[25] G. Dziuk. Finite elements for the Beltrami operator on arbitrary surfaces. *Springer-Verlag, Berlin*, 1357:142–155, 1988.

[26] G. Dziuk and C.M. Elliott. Finite element methods on evolving surfaces. *IMA Journal of Numerical Analysis*, 27:262–292, 2006.

[27] G. Dziuk and C.M. Elliott. An Eulerian approach to transport and diffusion on evolving implicit surfaces. *Computing and Visualization in Science*, 13 (1):17–28, 2010.

[28] G. Dziuk and C.M. Elliott. A fully discrete evolving surface finite element method. *SIAM Journal on Numerical Analysis*, 50(5):2677–2694, 2012.

[29] G. Dziuk and C.M. Elliott. Finite element methods for surface PDEs. *Acta Numerica*, 22:289–396, 2013.

[30] G. Dziuk and C.M. Elliott. L2 estimates for the evolving surface finite element method. *Mathematics of Computation*, 82:1–24, 2013.

[31] G. Dziuk, D. Kröner, and T. Müller. Scalar conservation laws on moving hypersurfaces. *Technical report, Freiburg*, 2012.

[32] G. Dziuk, C. Lubich, and D. Mansour. Runga-Kutta time discretization of parabolic differential equations on evolving surfaces. *IMA Journal on Numerical Analysis*, 32(2):394–416, 2012.

[33] C. Eilks and C.M. Elliott. Numerical simulation of dealloying by surface dissolution via the evolving surface finite element method. *Journal of Computational Physics*, 227(23):9727–9741, 2008.

[34] C.M. Elliott and T. Ranner. Finite element analysis for a coupled bulk surface partial differential equation. *IMA Journal on Numerical Analysis*, 33 (2):377–402, 2013.

[35] C.M. Elliott and B. Stinner. A surface phase field model for two-phase on biological membranes. *SIAM Journal on Applied Mathematics*, 70(8):2904–2928, 2010.

[36] C.M. Elliott and V. Styles. An ALE ESFEM for solving PDEs on evolving surfaces. *Milan Journal of Mathematics*, 80(2):469–501, 2012.

[37] C.M. Elliott, B. Stinner, V. Styles, and R. Welford. Numerical computation of advection and diffusion on evolving diffuse interface. *IMA Journal of Numerical Analysis*, 31(3):786–812, 2011.

[38] C.M. Elliott, B. Stinner, and C. Venkataraman. Modelling cell motility and chemotaxis with evolving surface finite elements. *Journal of the Royal Society Interface*, 9(76):3027–3044, 2012.

[39] I. Fatkullin. A study of blow-ups in the keller-segel model of chemotaxis. *Nonlinearity*, 26(1):81–94, 2013.

[40] M.S. Floater and K. Hormann. Surface parameterization: a tutorial and survey. *Advance in Multi-resolution for Geometric Modelling*, 282:157–186, 2005.

[41] V. French and P.M. Brakefield. The development of eyespot patterns on butterfly wings: Morphogen sources or sinks? *Development, Printed in Great Britain. The Company of Biologists Limited*, 116(1):103–109, 1992.

[42] L. Gierer and H. Meinhardt. A theory of biological pattern formations. *Kybernetik*, 12:30–39, 1971.

[43] D. Gilbarg and N.S. Trudinger. Elliptic partial differential equations of second order. *Berlin, Heidelberg, New York, Springer*, 224:1–517, 1983.

[44] R. Goldman. Curvature formulas for implicit curves and surfaces. *Computer Aided Geometric Design*, 22:632–658, 2005.

[45] A.B. Goryachev and A.V. Pokhilko. Dynamics of Cdc42 network embodies a turing-type mechanism of yeast cell polarity. *FEBS Letters*, 582(10):1437–1443, 2008.

[46] S. Gottlieb, C.-W. Shu, and E. Tadmor. Strong stability preserving high order time discretization methods. *SIAM Review*, 43:89–112, 2001.

[47] J.B. Greer. An improvement of a recent Eulerian method for solving PDEs on general geometries. *Journal of Scientific Computing*, 29(3):321–352, 2006.

[48] G.R. Grotendorst, I.K. Cohen, R.F. Diegelmann, and W.J. Lindblad. Chemoattractants and growth factors. In Wound Healing: Biochemical and Physical Aspects. *Wiley-Liss. New York*, 1, 1992.

[49] P. Herholz. General discrete Laplace operators on polygonal meshes. *Humboldt-Universität Berlin, Institut feur Mathematik und Informatik*, 2012.

[50] G. Hetzer, A. Madzvamuse, and W. Shen. Characterization of Turing diffusion-driven instability on evolving domains. *Discrete and Continuous Dynamical Systems- Series A*, 32(11):3975–4000, 2012.

[51] H. Huang, M.-C. Lai, and H.-C. Tseng. A parametric derivation of the surfactant transport equation along a deforming fluid interface. *Frontiers of Applied and Computational Mathematics*, pages 198–205, 2008.

[52] W. Huang and R.D. Russell. Adaptive moving mesh methods. *Springer, New York*, 2011.

[53] C. Johnson. Numerical solution of partial differential equations by the finite element method. *Cambridge University Press*, 1987.

[54] E.F. Keller and L.A. Segel. Conflict between positive and negative feedback as an explanation for the initiation of aggregation in slime mould amoebae. *Nature*, 227(5265):1365–1366, 1970.

[55] E.F. Keller and L.A. Segel. Initiation of slime mold aggregation viewed as an instability. *Journal of Theoretical Biology*, 26(3):399–415, 1970.

[56] E.F. Keller and L.A. Segel. Traveling bands of chemotactic bacteria: A theoretical analysis. *Journal of Theoretical Biology*, 30(2):235–248, 1971.

[57] A.J. Koch and H. Meinhardt. Biological pattern formation: From basic mechanisms to complex structures. *Reviews of Modern Physics*, 66(4): 1481–1507, 1994.

[58] V.I. Krinsky. Self-organization, auto-wave and structure far from equalibirium. *Springer, Berlin*, 4, 1984.

[59] D. Kuzmin. A guide to numerical methods for transport equations. *University Erlangen-Nuremberg, Erlangen*, 2010.

[60] D. Kuzmin. Linearity-preserving flux correction and convergence acceleration for constrained Galerkin schemes. *Journal of Computational and Applied Mathematics*, 236(9):2317–2337, 2012.

[61] D. Kuzmin and S. Turek. Flux correction tools for finite elements. *Journal of Computational Physics*, 175(2):525–558, 2002.

[62] C. Landsberg, F. Stenger, A. Deutsch, M. Gelinsky, A. Rsen-Wolff, and A. Voigt. Chemotaxis of mesenchymal stem cells within 3D biomimetic scaffolds-a modeling approach. *Journal of Biomechanics*, 44(2):359–364, 2011.

[63] J. Lefevre and J.-F. Mangin. A reaction-diffusion model of the human brain development. *In Biomedical Imaging: From Nano to Macro, IEEE International Symposium*, pages 77–80, 2010.

[64] Y. Li and J. Kim. A comparison study of phase-field models for an immiscible binary mixture with surfactant. *The European Physical Journal B*, 85 (9):1–9, 2012.

[65] P. Liu, J. Shi, Y. Wang, and X. Feng. Bifurcation analysis of reaction-diffusion schnakenberg model. *Journal of Mathematical Chemistry*, 51: 2001–2019, 2013.

[66] C. Lubich, D. Mansour, and C. Venkataraman. Backward difference time discretization of parabolic differential equations on evolving surfaces. *University of Warwic*, 32(2):1–20, 2013.

[67] C.B. Macdonald and S.J. Ruuth. Level set equations on surfaces via the closest point method. *Journal of Scientific Computing*, 35(2-3):219–240, 2008.

[68] C.B. Macdonald and S.J. Ruuth. The implicit closest point method for the numerical solution of partial differential equations on surfaces. *SIAM Journal on Scientific Computing*, 31(6):4330–4350, 2009.

[69] C.B. Macdonald, J. Brandman, and S.J. Ruuth. Solving eigenvalue problems on curved surfaces using the closest point method. *Journal of Computational Physics*, 230(22):7944–7956, 2011.

[70] R. Malladi and J.A. Sethian. Image processing: Flows under min/max curvature and mean curvature. *Graphical Models and Image Processing*, 58(2): 127–141, 1996.

[71] S. Mauch. A fast algorithm for computing the closest point and distance transform. *California Institute of Technology*, (29):1–18, 2000.

[72] D. Meidner and T. Richter. A posteriori error estimation for the fractional step theta discretization of the incompressible Navier Stokes equations. *Computer Methods in Applied Mechanics and Engineering*, 288:45–59, 2015.

[73] M. Mimura and T. Tsujikawa. Aggregating pattern dynamics in a chemotaxis model including growth. *Physica A: Statistical Mechanics and its Applications*, 230(3-4):499–543, 1996.

[74] T. Miura and P.K. Maini. Periodic pattern formation in reactiondiffusion systems: An introduction for numerical simulation. *Anatomical Science International*, 79:112–123, 2004.

[75] M. Möller. Algebraic flux correction for nonconforming finite element discretizations of scalar transport problems. *Computing*, 95(5):425–448, 2013.

[76] M. Möller, D. Kuzmin, and S. Turek. Implicit finite element discretizations based on the flux-corrected transport algorithm. *International Journal for Numerical Methods in Fluids*, 47(10-11):1197–1203, 2005.

[77] I. Mori and Y. Ohshima. Molecular neurogenetics of chemotaxis and thermotaxis in the nematode caenorhabditis elegans. *BioEssays*, 19(12):1055–1064, 1997.

[78] J.D. Murray. Discussion: Turing's theory of morphogenesis - its influence on modelling biological pattern and form. *Bulletin of Mathematical Biology*, 52(1-2):119–152, 1990.

[79] J.D. Murray. Mathematical Biology I: An introduction. *Springer Verlag, Third Edition*, 2002.

[80] J.D. Murray. Mathematical Biology II: Spatial Models and Biomedical Applications. *Springer Verlag*, 2003.

[81] M.P. Neilson, A.M. John, S.D. Webb, and H.I. Robert. Modeling cell movement and chemotaxis using pseduopod-based feedback. *SIAM Journal on Scientific Computing*, 33(3):1035–1057, 2011.

[82] L.I. Nicolaescu. The Co-area formula. *Department of Mathematics, University of Notre Dame*, 2014.

[83] H.F. Nijhout. Elements of butterfly wing patterns. *Journal of Experimental Zoology*, 291(3):213–225, 2001.

[84] T. Nozakura and S. Ikeuchi. Formation of dissipative structure in glaxies. *Astrophysics Journal*, 279:40–52, 1984.

[85] M.A. Olshanskii and A. Reusken. A finite element method for surface PDEs: Matrix properties. *Numerische Mathematik*, 114:491–520, 2009.

[86] M.A. Olshanskii and A. Reusken. Error analysis of a space-time finite element method for solving PDEs on evolving surfaces. *SIAM Journal on Numerical Analysis*, 52(4):2092–2120, 2014.

[87] M.A. Olshanskii and A. Reusken. A stabilized finite element method for advection-diffusion equations on surfaces. *IMA J. Numer. Anal.*, 28:732–758, 2014.

[88] M.A. Olshanskii and D. Safin. A narrow-band unfitted finite element method for elliptic PDEs posed on surfaces. *arXiv.org*, 1:1–19, 2014.

[89] M.A. Olshanskii, A. Reusken, and J. Grande. A finite element method for elliptic equations on surfaces. *SIAM Journal on Numerical Analysis*, 47(5): 3339–3358, 2009.

[90] M.A. Olshanskii, A. Reusken, and X. Xu. An Eulerian space-time finite element method for diffusion problems on evolving surfaces. *SIAM Journal on Numerical Analysis*, 52:1354–1377, 2014.

[91] S. Osher and R. Fedkiw. Level set methods and dynamic implicit surfaces. *Springer, New York,*, (153):1–188, 2002.

[92] H.G. Othmer and A. Stevens. Aggregation, blowup, and collapse: The abc's of taxis in reinforced random walks. *SIAM Journal on Applied Mathematics*, 57(4):1044–1081, 1997.

[93] Q. Ouyang and H.L. Swinney. Transition from a uniform state to hexagonal and striped turing patterns. *Nature*, 352(6336):610–612, 1991.

[94] K.J. Painter. Chemotaxis as a mechanism for Morphogenesis. *Brasenose College, University of Oxford*, D.Phil thesis,:1–236, 1997.

[95] M. Penstorf. Die level-Set-Methode für Reactions-Diffusions-Gleichungen auf statischen Oberflächen. *Tu-Dortmund*, 2014.

[96] A. Pressley. Elementary Differential Geometry. *Springer, London*, 2001.

[97] T. Ranner. Computational surface partial differential equations. *Department of Mathematics, The University of Warwick*, 2013.

[98] A. Rätz and M. Röger. Turing instabilities in a mathematical model for signaling networks. *Journal of Mathematical Biology*, 65(6-7):1215–1244, 2012.

[99] A. Rätz and A. Voigt. PDE's on surfaces a diffuse interface approach. *Commun. Math. Sci.*, 4:575–590, 2006.

[100] M. Razzaq. Numerical techniques for solving fluid-structure interaction problems with applications to bio-engineering. *PhD Thesis, TU Dortmund*, 2011.

[101] M. Razzaq, S. Turek, J. Hron, J. Acker, F. Weichert, I. Grunwald, C. Roth, M. Wagner, and B. Romeike. *FUNDAMENTAL TRENDS IN FLUID–STRUCTURE INTERACTION*, volume Contemporary Challenges in Mathematical Fluid Dynamics and its applications. World Scientific, 2010. Buch im LH vorhanden(ISSN: 10 981-4299-32-4/ 13 978-981-4299-32-9).

[102] M. Razzaq, C. Tsotskas, T. Kipouros, M. Savill, and J. Hron. Multi-objective optimization of a fluid structure interaction benchmarking. *CMES: Computer Modeling in Engineering and Sciences*, 90(4):303–337, 2013.

[103] S. Rosenberg. The Laplacian on a Riemannian Manifold: An Introduction to Analysis on Manifolds. *Cambridge University Press*, 1997.

[104] E. Rouy and A. Tourin. A viscosity approach to shape-from-shading. *SIAM Journal on Numerical Analysis*, (29):867–884, 1992.

[105] S.J. Ruuth and B. Merriman. A simple embedding method for solving partial differential equations on surfaces. *Journal of Computational Physics*, 227 (3):1943–1961, 2008.

[106] H.R. Schawrz. Finite Element Method. *Academic Press, London*, 1988.

[107] L.A. Segel and J.L. Jackson. Dissipative structure: An explanation and an ecological example. *Journal of Theoretical Biology*, 37(3):545–559, 1972.

[108] J.A. Sethian. An analysis of flame propagation. Phd thesis, department of mathematics. *University of California, Berkeley*, 1982.

[109] J.A. Sethian. Curvature flow and entropy conditions applied to grid generation. *Journal of Computational Physics*, (115):440–454, 1994.

[110] J.A. Sethian. A fast marching level set method for monotonically advancing fronts. *Proceedings of the National Academy of Sciences of the United States of America*, (93):1591–1595, 1996.

[111] J.A. Sethian. Level set methods and fast marching methods evolving interfaces in computational geometry, fluid mechanics, computer vision, and materials science. *Cambridge University Press*, (2):1–404, 1999.

[112] B.D. Sleeman and H.A. Levine. Partial differential equations of chemotaxis and angiogenesis. *Mathematical Methods in the Applied Sciences*, 24(6): 405–426, 2001.

[113] A. Sokolov, R. Strehl, and S. Turek. Numerical simulation of chemotaxis models on stationary surfaces. *Discrete and Continuous Dynamical Systems - Series B*, 18(10):2689–2704, 2013.

[114] A. Sokolov, R. Ali, and S. Turek. An AFC-stabilized implicit finite element method for partial differential equations on evolving-in-time surfaces. *Journal of Computational and Applied Mathematics*, 289:105–115, 2015.

[115] A. Sokolov, R. Strehl, R. Ali, and S. Turek. Numerical framework for pattern-formating models on evolving-in-time surfaces. *Department of applied mathematics, TU-Dortmund*, pages 1–17, 2015.

[116] H.A. Stone. A simple derivation of the time dependent convective diffusion equation for surfactant transport along a deforming interface. *Phys.Fluids A2*, 2:111–112, 1990.

[117] R. Strehl. Advanced numerical treatment of chemotaxis driven PDEs in mathematical biology. *TU Dortmund*, 2013.

[118] R. Strehl, A. Sokolov, D. Kuzmin, and S. Turek. A flux-corrected finite element method for chemotaxis problems. *Computational Methods in Applied Mathematics*, 10(2):219–232, 2010.

[119] R. Strehl, A. Sokolov, and S. Turek. Efficient, accurate and flexible finite element solvers for chemotaxis problems. *Computers and Mathematics with Applications*, 64(3):175–189, 2012.

[120] R. Strehl, A. Sokolov, D. Kuzmin, D. Horstmann, and S. Turek. A positivity-preserving finite element method for chemotaxis problems in 3D. *Journal of Computational and Applied Mathematics*, 239(1):290–303, 2013.

[121] L. Tian, C.B. Macdonald, and S.J. Ruuth. Segmentation on surfaces with the closest point method. *Proceedings - International Conference on Image Processing, ICIP*, pages 3009–3012, 2009.

[122] T. Tsiotsios and M. Petrou. On the choice of the parameters for anisotropic diffusion in image processing. *Pattern Recognition*, 46(13):69–81, 2013.

[123] S. Turek. Efficient solvers for incompressible flow problems: An algorithmic and computational approach. *Springer*, 6:1–358, 1999.

[124] S. Turek and R. Schmachte. Fully coupled and operator-splitting approaches for natural convection flows in enclosures. *International Journal for Numerical Methods in Fluids*, 40:1109–1119, 2002.

[125] S. Turek, L. Rivkind, J. Hron, and R. Glowinski. Numerical analysis of a new time stepping theta scheme for incompressible flow simulations. *Journal of Scientific computing*, pages 533–540, 2006.

[126] S. Turek, J. Hron, M. Madlik, M. Razzaq, H. Wobker, and J. Acker. Numerical simulation and benchmarking of a monolithic multigrid solver for fluid–structure interaction problems with application to hemodynamics. In H. Bungartz, M. Mehl, and M. Schäfer, editors, *Fluid-Structure Interaction II: Modelling, Simulation, Optimisation*. Springer, 2010. doi 10.1007/978-3-642-14206-2.

[127] S. Turek, J. Hron, M. Razzaq, and M. Schäfer. Numerical benchmarking of fluid–structure interaction: A comparison of different discretization and solution approaches. In H. Bungartz, M. Mehl, and M. Schäfer, editors, *Fluid-Structure Interaction II: Modelling, Simulation, Optimisation*. Springer, 2010. doi 10.1007/978-3-642-14206-2.

[128] S. Turek, O. Mierka, S. Hysing, and D. Kuzmin. Numerical study of a high order 3D FEM-level set approach for immiscible flow simulation numerical methods for differential equations, optimization, and technological problems. *Computational Methods in Applied Sciences*, 27(4):65–91, 2013.

[129] A. Turing. The chemical basis of morphogenesis. *Phil Trans B*, 337:37–72, 1952.

[130] R. Tyson, S.R. Lubkin, and J.D. Murray. A minimal mechanism for bacterial pattern formation. *Proceedings of the Royal Society B: Biological Sciences*, 266(1416):299–304, 1999.

[131] R. Tyson, S.R. Lubkin, and J.D. Murray. Model and analysis of chemotactic bacterial patterns in a liquid medium. *Journal of Mathematical Biology*, 38 (4):359–375, 1999.

[132] R. Tyson, L.G. Stern, and R.J. LeVeque. Fractional step methods applied to a chemotaxis model. *Journal of Mathematical Biology*, 41(5):455–475, 2000.

[133] C. Venkataraman. Reaction-diffusion systems on evolving domains with applications to the theory of biological pattern formation. *University of Sussex*, 2011.

[134] F. Weichert, L. Walczak, D. Fisseler, T. Opfermann, M. Razzaq, R. Münster, S. Turek, I. Grunwald, C. Roth, C. Veith, and M. Wagner. Simulation of intra–aneurysmal blood flow by using different numerical methods. *Computational and Mathematical Methods in Medicine*, 2011. published (doi:10.1155/2013/527654).

[135] D.B. White. The plan forms and on set of convection with a temperature dependent viscosity. *Journal Fluid Mechanics*, 191:247–286, 1984.

[136] S.S. Willard and P.N. Devreotes. Signaling pathways mediating chemotaxis in the social amoeba, dictyostelium discoideum. *European Journal of Cell Biology*, 85(9-10):897–904, 2006.

[137] D. Wu. Signaling mechanisms for regulation of chemotaxis. *Cell Res.*, 15 (1):52–56, 2005.

[138] K. Xia and G.-W. Wei. A Galerkin formulation of the MIB method for three dimensional elliptic interface problems. *Computers and Mathematics with Applications*, 68:719–745, 2014.

[139] J.-J. Xu and H.-K. Zhao. An Eulerian formulation for solving partial differential equations along a moving interface. *J. Sci. Comput.*, 19:573–593, 2003.

[140] Y. Yang, H. Chen, and W. Liu. On existence of global solutions and blow-up to a system of reaction-diffusion equations modelling chemotaxis. *SIAM Journal on Mathematical Analysis*, 33(4):763–785, 2001.

[141] S.T. Zalesak. Fully multidimensional flux-corrected transport algorithms for fluids. *Journal of Computational Physics*, 31(3):335–362, 1979.

[142] M. Zhang and C. Zhu. Global existence of solutions to a hyperbolic-parabolic system. *Proceedings of the American Mathematical Society*, 135 (4):1017–1027, 2007.

[143] O.O. Zienkiewicz. Finite element method: Its basis and fundamentals. *Oxford, England: Elsevier*, 2005.